

INFORMATION TO USERS

This manuscript has been reproduced from the microfilm master. UMI films the text directly from the original or copy submitted. Thus, some thesis and dissertation copies are in typewriter face, while others may be from any type of computer printer.

The quality of this reproduction is dependent upon the quality of the copy submitted. Broken or indistinct print, colored or poor quality illustrations and photographs, print bleedthrough, substandard margins, and improper alignment can adversely affect reproduction.

In the unlikely event that the author did not send UMI a complete manuscript and there are missing pages, these will be noted. Also, if unauthorized copyright material had to be removed, a note will indicate the deletion.

Oversize materials (e.g., maps, drawings, charts) are reproduced by sectioning the original, beginning at the upper left-hand corner and continuing from left to right in equal sections with small overlaps.

Photographs included in the original manuscript have been reproduced xerographically in this copy. Higher quality 6" x 9" black and white photographic prints are available for any photographs or illustrations appearing in this copy for an additional charge. Contact UMI directly to order.

ProQuest Information and Learning
300 North Zeeb Road, Ann Arbor, MI 48106-1346 USA
800-521-0600

UMI[®]

**A HIGH SPEED OPTICAL SURFACE COORDINATE
MEASUREMENT SYSTEM AND ITS APPLICATIONS
TO DYNAMIC MEASUREMENTS**

Yong Li

**A thesis submitted to the Faculty of Graduate Studies and
Research in partial fulfillment of the requirements of the
Degree of Doctor of Philosophy**

**Department of Mechanical Engineering
McGill University, Montreal, Canada
February 2000**

© Yong Li, 2000



**National Library
of Canada**

**Acquisitions and
Bibliographic Services**

**395 Wellington Street
Ottawa ON K1A 0N4
Canada**

**Bibliothèque nationale
du Canada**

**Acquisitions et
services bibliographiques**

**395, rue Wellington
Ottawa ON K1A 0N4
Canada**

Your file Votre référence

Our file Notre référence

The author has granted a non-exclusive licence allowing the National Library of Canada to reproduce, loan, distribute or sell copies of this thesis in microform, paper or electronic formats.

The author retains ownership of the copyright in this thesis. Neither the thesis nor substantial extracts from it may be printed or otherwise reproduced without the author's permission.

L'auteur a accordé une licence non exclusive permettant à la Bibliothèque nationale du Canada de reproduire, prêter, distribuer ou vendre des copies de cette thèse sous la forme de microfiche/film, de reproduction sur papier ou sur format électronique.

L'auteur conserve la propriété du droit d'auteur qui protège cette thèse. Ni la thèse ni des extraits substantiels de celle-ci ne doivent être imprimés ou autrement reproduits sans son autorisation.

0-612-64605-X

Canada

Dedicated to my parents and my lovely wife.

Abstract

Currently there is no standard whole-field methodology to measure the transient out-of-plane deformation of a surface under dynamic events. In this work, a whole-field high-speed optical surface measurement system has been developed, which yields absolute Cartesian coordinates (xyz) as measurement results. A high-speed digital camera coupled with the grating projection and Fourier transform is used to measure 3D surface deformations with the maximum sampling rate up to 1000 Hz and the exposure time of each frame up to 50 μ sec. A calibration technique has been utilized to convert the direct measurable values—phase, Φ , and image indices (i, j)—into 3D Cartesian coordinates (xyz). In addition, all Cartesian coordinates are with respect to a fixed coordinate system, which is virtually associated with the sensor head. Therefore, the rigid body movements (rotation and translation) of the surface can be detected. The measurement accuracy $\pm 50 \mu\text{m}$ is verified with several tests by using standard objects.

The dynamic surface deformation during polymer membrane inflation tests is investigated by using the proposed optical measurement system. Effects of various factors, such as the temperature and the airflow rate, are studied. Regarding the characterization of material constants by using the bubble inflation technique, the potential problems, which are caused by ignoring the nonuniformities of temperature distribution and the thermo-warping, have been studied.

A finite-element model, which can account for the nonuniformities of temperature distribution and the thermo-warping, has been employed to simulate the inflation deformation. A more accurate way to characterize the material constants is accomplished by combining the optical measurement system and a finite-element model that can account for the nonuniformities of the temperature distribution and the thermo-warping.

Résumé

Actuellement, il n'y a pas des méthodes standards permettant de mesurer la déformation hors plan d'une surface sous sollicitations dynamique. Dans ce travail, un système optique rapide de mesure a été développé et qui permet de visualiser les résultats dans le système de coordonnées cartésiennes absolu (xyz). Une camera digitale à grande vitesse, équipée d'un système de projection et utilisant la transformée de Fourier pour mesurer les déformations d'une surface tridimensionnelle avec une fréquence maximale allant jusqu'à 1000Hz et un temps d'exposition de chaque image allant jusqu'à 50 μ sec. Une technique de calibration a été utilisée afin de convertir les mesures directes des valeurs de la phase, Φ , et des indices de l'image (i, j) dans le système tridimensionnel de coordonnées cartésiennes (xyz). En plus, tous les coordonnées cartésiennes sont par rapport à un système de coordonnées fixe, qui est virtuellement lié à la tête du capteur. Ainsi, les mouvements du corps rigide (rotation et translation) de la surface peuvent être détectés. La précision de mesures ($\pm 50 \mu\text{m}$) est vérifiée à l'aide de plusieurs tests en utilisant des objets standards.

La déformation de la surface dynamique pendant les tests de gonflement membranaire du polymère est entreprise en utilisant le système de mesures optique proposé. Les effets des divers facteurs, tels que la température et l'écoulement d'air sont étudiés. Concernant la détermination des paramètres du modèle en utilisant la technique du gonflement, les problèmes potentiels qui se manifestent en ignorant la distribution non uniforme de la température et de la dilatation thermique ont été étudiés.

Un modèle éléments finis qui prend en compte la nonuniformité de la température et de la dilatation thermique, a été employé pour simuler la déformée. Une méthode plus précise de déterminer les paramètres du matériau est accomplie en combinant le système de mesure optique et le modèle éléments finis part la prise en compte des effets de variation de la température et de la dilatation thermique.

Acknowledgements

First and foremost, I would like to thank my academic advisor, Prof. J. A. Nemes, not only for the guidance he has provided me throughout the course of my graduate studies, but also for his patience and friendship.

I am very grateful to Dr. A. Derdouri for giving me the opportunity to participate in the bubble inflation tests on polymer materials at the Industrial Materials Institute of NRC. Thanks are also extended to Madam M. Plourde for her expertise in carrying out the bubble inflation tests.

I would like to thank Mr. S. Kecani of Physics machine shop at McGill University for his assistance and machining most of the mechanical parts used in this research. Portions of this study could not have been completed without the assistance of a number of people, including Prof. L. Lessard, Prof. J. Angeles, Prof. R. Funnell, Marie-Josée Potvin, Gilbert Bande, H. Samrout, H. Eskandari, E. Del Campo, G. Dedic, G. Tewfik, and S. Mitsialis. This work has been supported partially by the Natural Sciences and Engineering Research Council of Canada (NSERC) through an equipment grant.

Finally, I wish to express my gratitude to my wife for her love and support throughout these four and half years.

Table of Contents

ABSTRACT	I
RÉSUMÉ	II
ACKNOWLEDGEMENTS	III
TABLE OF CONTENTS	IV
LIST OF FIGURES	VII
LIST OF TABLES	XI
LIST OF SYMBOLS	XII
CHAPTER 1 INTRODUCTION	1
1.1 Motivation	1
1.2 Literature Review	4
1.2.1 Non-contact 3D Optical Measurement Methods	4
1.2.2 Dynamic Deformation Measurements by Using Optical Methods ..	12
1.3 Objectives	14
1.4 Thesis Outline	15
CHAPTER 2 OPTICAL MEASUREMENT METHODS	16
2.1 Introduction	16
2.2 Grating Projection Surface Shape Measurement	16
2.2.1 Fundamental of Gratings	16
2.2.2 Mathematical Modeling of Grating Images	19
2.2.3 Methods to Extract Phase Information	23
2.3 Fourier transform phase calculation	26
2.3.1 Basics	26
2.3.2 Discrete Fourier Transform	29
2.3.3 Phase Calculation by the Fourier Transform	31
2.4 Phase Unwrapping	35
2.4.1 Point-by-point Unwrapping Algorithm	36
2.4.2 Region-based Unwrapping Algorithm	41
2.5 Summary	45
CHAPTER 3 SYSTEM CALIBRATION	47
3.1 Introduction	47
3.2 Imaging Geometry	48
3.3 Calibration Techniques	51
3.3.1 Camera Model	52
3.3.2 Phase-to-Z Conversion	57
3.3.3 Calibration Procedure	58

3.4 Summary	61
CHAPTER 4 DYNAMIC MEASUREMENT SYSTEM	63
4.1 Introduction	63
4.2 System Overview	63
4.3 High-speed Camera Specifications	65
4.4 Multi-channel Data Link	67
4.5 Summary	68
CHAPTER 5 ACCURACY AND SENSITIVITY TESTS	69
5.1 Introduction	69
5.1.1 Geometric Moiré Methods	70
5.1.2 Phase-computing-based Optical 3D Measurement Techniques	71
5.2 Flat Surface Test	73
5.3 Cylindrical Surface Test	76
5.4 Sine Vise Test	78
5.5 Sensitivity Test	79
5.6 Summary	81
CHAPTER 6 BIAxIAL EXTENSION TESTS OF POLYMERIC MATERIAL	83
6.1 Introduction	83
6.1.1 Background	83
6.1.2 Inflation of Plane Circular Membrane and Basic Equations	84
6.1.3 Application of High-speed Optical Measurement System to Bubble Inflation Tests	89
6.2 Experimental Setup	89
6.3 Experimental Results and Data Analysis	91
6.3.1 Overview of Measurement Results	91
6.3.2 Real Shape of A Bubble	95
6.3.3 Temperature Effect	101
6.3.4 Airflow Rate Effect	103
6.3.5 Thermoformability	104
6.3.6 Deformation in Heating Process	106
6.4 Summary	108
CHAPTER 7 FINITE-ELEMENT ANALYSIS ON CIRCULAR MEMBRANE INFLATION	110
7.1 Introduction	110
7.2 Finite-element Model	113
7.2.1 Geometry & Mesh Generation	113
7.2.2 Element Model	113
7.3 Finite-element Analysis—Idealized Conditions	115

7.3.1 Finite-element Simulation for ABS Inflation Test T1-1503	115
7.4 Finite-element Analysis—General Conditions	120
7.4.1 Finite-element Simulation for ABS Inflation Test T1-1503	122
7.5 Summary	130
CHAPTER 8 CONCLUSIONS AND FUTURE DEVELOPMENTS	132
8.1 Conclusions	132
8.2 Future Developments	133
8.2.1 Optical Dynamic Measurement System	133
8.2.2 Membrane Inflation Experiments	133
8.2.3 Finite-element Modeling and Material Constant Characterization . .	133
8.2.4 Other Applications	134
ORIGINALITY AND CONTRIBUTION TO KNOWLEDGE	135
APPENDICES	137
Appendix A: System Calibration	137
Appendix B: Input File of ABAQUS for Idealized Conditions	140
Appendix C: Input File of ABAQUS for General Conditions	142
REFERENCES	147

List of Figures

Fig. No.	Captions	Page No.
1.1	The coordinate measuring machine (CMM) and touch probe.	2
1.2	Optical layout of the shadow Moiré method.	4
1.3	Moiré fringe of a 3D object.	5
1.4	Optical setup of the projection Moiré method.	7
1.5	Digital image representation.	7
1.6	Schematic of a CCD camera.	10
1.7	Reference point used in optical dynamic measurements.	13
2.1	Ronchi grating.	17
2.2	Fig. 2.2 Grating images on flat and cylindrical surfaces: (a) setup for a flat surface; (b) setup for a cylindrical surface; (c) deformed grating image on the flat surface; (d) deformed grating image on the cylindrical surface.	18
2.3	Intensity distribution of a grating: (a) grating image; (b) intensity distribution along the X-axis.	19
2.4	Left—grating projected onto a surface; Right—change in grating spacing with the change of surface.	21
2.5	A simple function and its Fourier spectrum.	28
2.6	Phase calculation by the Fourier transform.	34
2.7	Wrapped phase map.	35
2.8	Unwrapped phase distribution along a line.	36
2.9	Scanning line approach for phase unwrapping.	37
2.10	Inconsistency flagging.	38
2.11	The path to circumnavigate the inconsistent pixel segment.	39
2.12	Second differences calculation.	40
2.13	Example of phase map divided into regions.	42
2.14	Phase unwrapping example—cylindrical surface: (a) original deformed grating image (grating lines are parallel with the axis of the cylinder); (b) wrapped phase image; (c) unwrapped phase image.	43

Fig. No.	Captions	Page No.
2.15	Phase unwrapping example—cylindrical surface: (a) original deformed grating image (grating lines are perpendicular with the axis of the cylinder); (b) wrapped phase image; (c) unwrapped phase image.	44
2.16	Processing summary of the grating projection and Fourier method.	45
3.1	Basic geometry model of image forming.	49
3.2	Examples of lens distortion: (a) original grid; (b) pincushion distortion; (c) barrel distortion.	50
3.3	Pinhole camera model with lens distortion.	52
3.4	Definition of Euler angles.	53
3.5	Transformation from 3D global coordinate to 2D image coordinate.	56
3.6	Crossed-optical-axes geometry.	57
3.7	Schematic of the experimental setup for camera calibration.	59
4.1	Schematic of the high-speed optical measurement system.	63
4.2	Kodak Motion Corder High-speed camera SR-1000	65
4.3	Kodak Multi-channel Data Link.	68
5.1	Sensitivity concept in the geometric Moiré methods.	70
5.2	Surface flatness test.	74
5.3	Measurement result of a flat surface—point cloud.	74
5.4	Cylindrical surface test.	76
5.5	Point cloud display of the measured data on a cylindrical surface.	77
5.6	The best-fit results at $y=0.0$.	77
5.7	Accuracy tests with a sine vise set at different angles.	78
5.8	Sensitivity test location in the depth of view. (step size= $10\ \mu$)	80
6.1	Thermoforming process: (1) preheated thermoplastic sheet; (2) mold base plate; (3) mold body; (4) pressure plate; (5) trapped air.	84
6.2	Geometry of a bubble.	85

Fig. No.	Captions	Page No.
6.3	Cross-section view of the bubble inflation test: (1) upper plate; (2) lower plate; (3) polymer sheet.	88
6.4	The bubble inflation experimental setup: (1) polymer sheet; (2) pressure chamber.	90
6.5	The measurement result of bubble inflation: ABS @150°C and 3.0 liter/s airflow rate. The measurement was taken at 160 ms after inflation.	92
6.6	Rectangular xyz coordinate calculation window.	93
6.7	Wire-frame display of Fig. 6.5.	93
6.8	Pressure vs. height in a typical bubble inflation test.	94
6.9	Pressure vs. height for ABS @ 150°C and 3.0 liter/s airflow rate.	95
6.10	Cross-sectional shape of a bubble at 160 ms after inflation	96
6.11	Curvature distribution at 160 ms after inflation & $h/a=0.378$.	97
6.12	Gaussian surface curvature distribution at 160 ms after inflation. ($h/a=0.378$)	98
6.13	The bubble inflation at different times: from bottom up at time 20, 40, 80, 120, and 160 msec. The zero deformation is defined as the polymer sheet position before heating.	99
6.14	Curvature distribution at different times: (a) $t=0.0$ ms deformation due to heating; (b) $t=20$ ms; (c) $t=40$ ms; (d) $t=160$ ms. Distance from the edge to the inflection point is indicated.	100
6.15	Warpage due to the heating of the ABS material.	101
6.16	Temperature effect on the bubble inflation tests for ABS material: (a) 130°C; (b) 150°C; (c) 180°C. All at 3.0 liter/s airflow rate.	102
6.17	Airflow rate effect on the ABS material at 150°C: (a) 3.0 liter/s; (b) 5.0 liter/s; (c) 8.0 liter/s.	103
6.18	Bubble profiles at $t=0$ and $t=120$ ms: (a) ABS; (b) HDPE; (c) HIPS. Temperature at 130°C and airflow rate at 3.0 liter/s.	105
6.19	Warping of the HDPE specimen at 140°C before inflation.	106
6.20	Bubble profiles of HDPE at $t=0$ and $t=220$ ms. With 3.0 liter/s airflow rate and 140°C.	107
6.21	Wireframe display of the bubble shape of a HDPE sheet at $t=220$ ms with 3.0 liter/s airflow rate and 140°C.	107

Fig. No.	Captions	Page No.
6.22	Curvature distribution of cross-sectional lines of a HDPE bubble at (a) $t=0$ ms and (b) $t=220$ ms with 3.0 liter/s airflow rate and 140°C.	108
7.1	Finite-element mesh for circular ABS membranes.	113
7.2	Element type (CAX8H) and boundary condition.	114
7.3	The ABAQUS simulation results:(a) pressure= 0.2852×10^4 Pa; (b) pressure = 1.0000×10^4 Pa; (c) pressure= 2.6428×10^4 Pa; (d) pressure= 6.344×10^4 Pa.	116,117
7.4	Bubble shape comparison @ 0.011 MPa.	118
7.5	Bubble shape comparison @ 0.023 MPa.	118
7.6	Bubble height vs. pressure of ABS material considering uniform temperature distribution.	119
7.7	Temperature distribution measured by an infrared camera.	121
7.8	Typical temperature distribution along a line passing through the center.	122
7.9	Temperature profile used for FEM simulation. (from the center to the clamped edge)	123
7.10	Material constants C_{10} and C_{01} as functions of temperature.	123
7.11	ABAQUS simulation results considering temperature nonuniformity and thermo-warping: (a) pressure= 0.3982×10^4 Pa; (b) pressure= 2.3675×10^4 Pa; (c) pressure= 4.6618×10^4 Pa; (d) pressure= 4.5495×10^4 Pa.	126,127
7.12	Bubble shape comparison: (a) pressure=0.011 MPa; (b) pressure=0.022 MPa. (Considering the thermal warpage and temperature gradient)	128
7.13	Bubble height vs. pressure curve of ABS material considering nonuniform temperature distribution and thermo-warping.	129

List of Tables

Table 2.1 Light intensity distribution of a portion of a grating image.	20
Table 2.2 Features of different optical profile measurement methods.	46
Table 4.1 Specifications of the Kodak SR-1000 high-speed camera.	66
Table 5.1 Flat surface test results.	75
Table 5.2 The best-fit results of the cylindrical surface.	78
Table 5.3 Accuracy test results on the sine vise.	79
Table 5.4 Sensitivity test results.	81

List of Symbols

b	distance between the centers of projector lens and camera lens
l	distance between the center of projector lens and the grating
d	grating pitch
k	order number of Moiré fringes
z_k	distance between grating plane and the k^{th} order Moiré fringe
Δz	distance between two successive Moiré fringes
d_r	grating pitch on virtual reference plane
q	distance between the projection grating and the projection lens
x, y, z	3D Cartesian coordinates
i, j	2D image coordinates or index
I	light intensity in a digitized image (0–255)
Φ	phase
$F(u)$	Fourier transform of function $f(x)$
U	strain energy potential
C_{10}, C_{01}	material constants used in the Mooney-Rivlin model
P	inflating pressure
a	radius of the circular opening
R	radius of the spherical bubble
h	bubble height
λ_i	stretch ratio ($i=1,2,3$)
T_1, T_2	stress resultants
K_1, K_2	principal curvatures

CHAPTER 1

INTRODUCTION

1.1 Motivation

Thanks to Descartes, we may characterize our physical world, known as three-dimensional (3D) Euclidean space, in algebraic terms by establishing a Cartesian coordinate system (three mutually perpendicular number lines whose origins coincide at a single point, known as the origin of the coordinate system). Call one of these lines the X -axis, and then choose one of the remaining lines as the Y -axis. The last perpendicular line through the origin is called the Z -axis by adopting the right-hand rule. Any point P in 3D space can then be located or represented by an ordered triple of real numbers (x, y, z) , called the Cartesian coordinates of point P . The first number in the ordered triple indicates the location of the point in the direction of the X -axis, the second one indicates its location in the direction of the Y -axis, and the third number indicates the location of the point in the direction of the Z -axis. Any object in the physical world has its position, and occupies a certain space. By using a Cartesian coordinate system all the geometric properties of an object can be described. Therefore, the goal of 3D-measuring techniques, both optical and mechanical methods, is the determination of the Cartesian coordinates of an object.

As shown in Fig. 1.1, Coordinate Measuring Machines (CMMs) are the conventional tools for dimensional measurements of various mechanical components by the use of touch probes. A touch probe is a special electronic sensor that can generate a recording signal to a CMM to record simultaneously the x , y , and z positions when the head of the touch probe comes into contact with the surface to be measured. So, by touching the surface, a CMM can create x , y , and z coordinates for that point being touched. CMMs have high accuracy in the measurements of 3D coordinates, but suffer from important limitations such as: high cost, low measurement speed, and limitations on the autonomous measurements of the entire part surface. In addition, CMMs have to touch the surface, but in some applications the physical contact is not recommended, such as

measuring membrane structures. As a solution to this problem, optical non-contact sensors including stereo vision systems, laser scanning systems and fringe systems have important advantages over the CMMs. Significant advantages include high speed (~20,000 point/sec) and the ability to perform measurements on the entire surface of a part without physical contact.

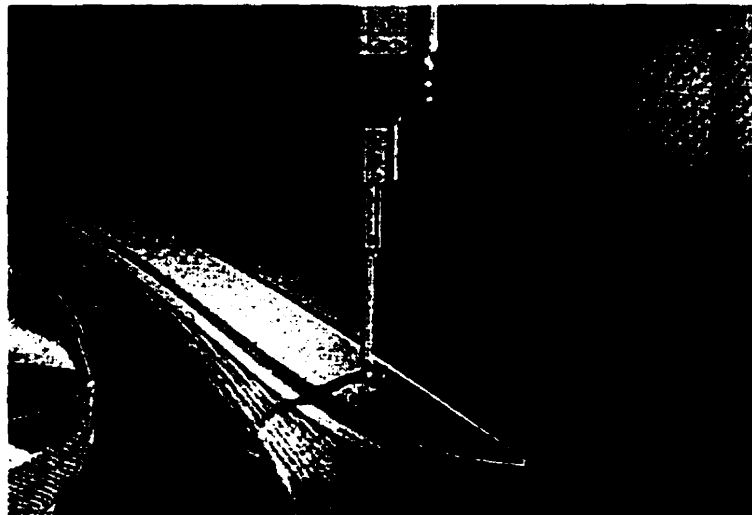


Fig. 1.1 The coordinate measuring machine (CMM) and touch probe.

However, the development of these new high speed and high precision optical non-contact sensors solve only a portion of the problem. Sometimes, the surface to be measured is changing its shape dynamically, as in the case of surfaces under vibration or impact. There is no time for a laser scanning system to finish one scanning cycle before the surface changes. Another example is the dynamic buckling of plates. The buckling shape is changing with the increase of loading. Other examples include free surface waves in hydrodynamics. The fluid surface shape is changing all the time due to the surface waves, and accurate prediction or measurement of the surface wave is a necessity in the fields of offshore and coastal engineering. The 3D measurement of the surfaces under transient deformation are too difficult for both conventional CMMs and optical measurement systems to deal with. In fact, there is no standard methodology to measure the transient deformation of a surface in a dynamic event. However, dynamic 3D surface measurements, which can provide the knowledge of the entire deformed field and its time history, can help to gain a better understanding of these complicated phenomena. This is the motivation of this research work.

Prior to formulating the specific objectives of this work in Section 1.3, a review of the literature on 3D optical measurement methods and their various applications on dynamic deformation measurements is given in Section 1.2. There are many optical measurement methods available today, such as photoelasticity, geometric Moiré, Moiré interferometry, holographic interferometry, shearography, laser scanning techniques, and laser speckle interferometry. Depending on their applications, they fall into two categories: *in-plane measurement* (in-plane strains and displacements) and *out-of-plane measurement* (out-of-plane displacement components, surface profile and topography). This work focuses on the out-of-plane measurement methods, which have the potential to provide 3D surface shape information. In addition, laser-scanning techniques are not considered in this work because they can only provide 3D information on a line at each time, and the time required to scan the whole surface makes them impractical for dynamic surface measurement. In such a case, what we need is an optical measurement technique, which can be used in dynamic 3D surface measurement to provide whole-field coordinate

information. In the next section, a literature review will be carried out for various optical techniques for the out-of-plane measurement.

1.2 Literature Review

1.2.1 Non-contact 3D Optical Measurement Methods

The *shadow Moiré method* is one of the first scientific applications of the Moiré phenomenon, which is if two superposed sets of lines are dense enough and show some regularities, a pattern known as Moiré fringes will be formed in addition to the individual line sets. The work in this area goes back to early 1940's. The principle of shadow Moiré is easy to understand.

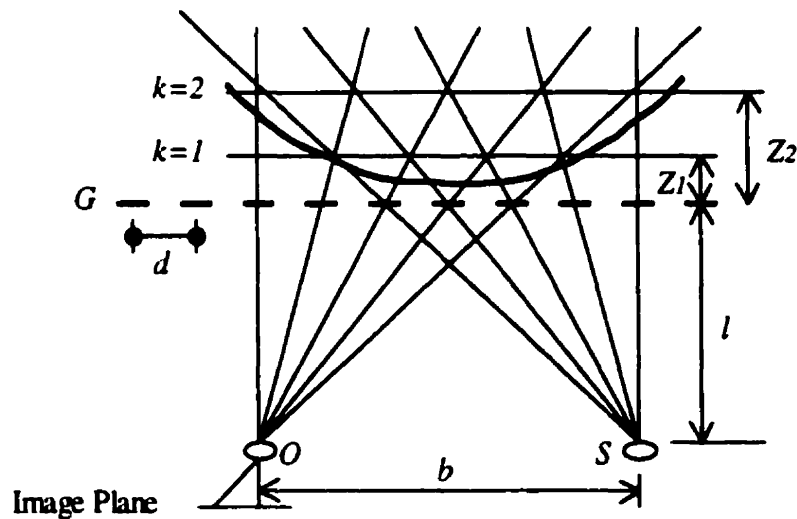


Fig. 1.2 Optical layout of the shadow Moiré method.

As shown in Fig. 1.2, a point light source S casts the shadow of a grating G , which consists of equispaced parallel black lines, onto the surface of an object. The grating shadow is modulated by the surface so it looks as if it is somehow deformed. When the shadow is viewed through the original grating, the two sets of lines (original grating and its deformed shadow) interfere with each other, and Moiré fringes are generated on the image plane due to this geometric interference. If the distance between the camera and

the grating is equal to that between the light source and the grating, the observed Moiré fringes will represent iso-height contours of the surface—all the points on a Moiré fringe will have same distance to the reference grating plane (Meadows, Johnson & Allen 1970, and Takasaki 1970). As shown in Fig. 1.2, the distance to the reference grating plane or the height is z_k for all the points on the k^{th} order Moiré fringe. The order of Moiré fringe is k ($k = 0, 1, 2, \dots$). A Moiré fringe image is shown in Fig. 1.3, which was taken for a 3D curved object of approximately $300 \times 250 \times 150$ mm in overall dimension. The black coarse curved lines are Moiré fringes, and the original straight grating lines are very fine in the background (running vertically).

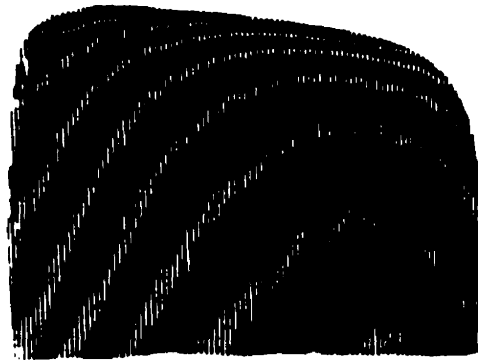


Fig. 1.3 Moiré fringes of a 3D object.

If the straight line connecting S and O is parallel to the plane of the grating, we can assume a simple equation to calculate the height of points on each Moiré fringe to the grating plane. All contour lines are parallel to the G plane.

$$z_k = \frac{l \times k \times d}{b - k \times d} \quad (k = 0, 1, 2, \dots) \quad (1.2-1)$$

Here, z_k is the distance between the G plane and the k^{th} order Moiré contour line. The distance between the lighting source and the G plane is l , and b is the distance between the lighting source and the camera. Finally, d is the pitch of the grating and k is the order

number of the Moiré contour lines, which is equal to 0, 1, and 2... The distance between successive contour lines Δz , called the sensitivity, is:

$$\Delta z = \frac{d \times l}{b} \times \frac{(1+z_k/l)^2}{1+(1+z_k/l) \times d/b} \quad (k = 0, 1, 2, \dots) \quad (1.2-2)$$

From Eq. 1.2-2, we can see that the sensitivity of the shadow Moiré method is not a constant; it increases with increasing order of the contour lines. If, as is often the case, $z_k/l \ll 1$ and $d/b \ll 1$, Eq. 1.2-2 can be simplified to have a constant value.

$$\Delta z = d \times \frac{l}{b} \quad (1.2-3)$$

The sensitivity of Moiré methods is an important factor, and it was often utilized to evaluate the precision of a Moiré system. The sensitivity and accuracy issues will be discussed in Chapter 3 and 5.

The projection Moiré method is a modified version of the shadow Moiré. As shown in Fig. 1.4, instead of using a grating in front of the surface, a grating, called the master grating, is projected onto the surface by using a lens. Therefore, the overall size of the master grating is usually very small comparing with the grating used in the shadow Moiré. However, a second grating, called the reference grating, is needed at the image plane of the viewing lens to generate Moiré fringes, due to the interference between the image of the master grating and the reference grating. Then a camera focusing at the reference-grating plane has to be used to record the Moiré fringes created. The setup of projection Moiré is therefore more complicated than that of the shadow Moiré. The equations derived for the shadow Moiré are still valid for the projection Moiré except that d must be substituted by dr , the pitch of the master grating on a virtual reference plane. All heights calculated are then with respect to this virtual reference plane.

$$dr = d \times \frac{l}{q} \quad (1.2-4)$$

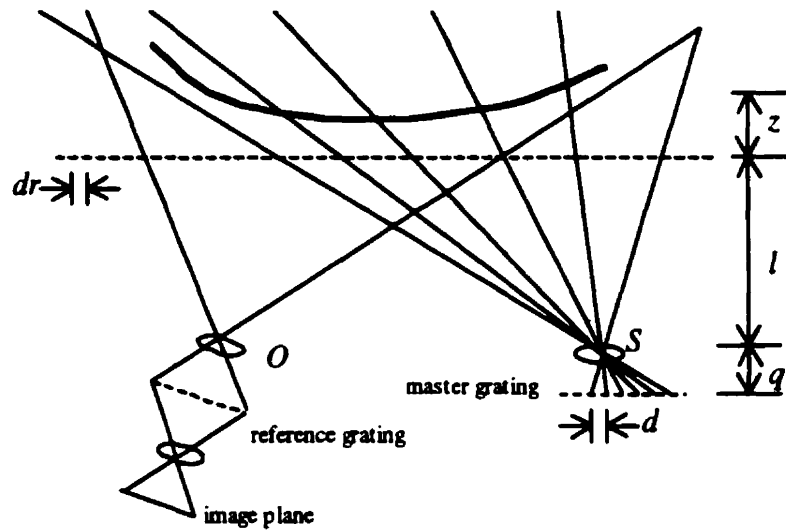


Fig. 1.4 Optical setup of the projection Moiré method.

As shown in Fig. 1.3, the direct measurement result of the shadow Moiré or the projection Moiré is a 2D image containing Moiré fringes, which represent contour lines. A number of researchers have scanned the resulting image to provide a digitized format, which provides a two-dimensional light intensity function $f(i, j)$, where i and j denote the image coordinates and the value f at any point (i, j) is proportional to the brightness or gray level of the image at that point. The origin of the image coordinate system can be anywhere in the image, but usually is taken as the image center or one of the image corners. In this case, the 2D image has been discretized by a digital camera both in spatial coordinates and in brightness as shown in Fig. 1.5.

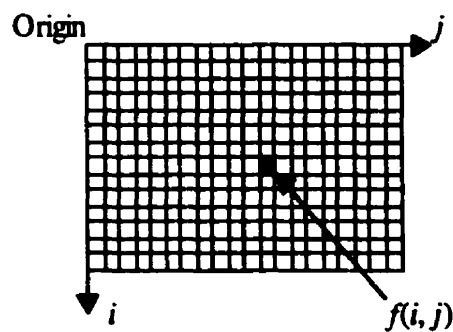


Fig. 1.5 Digital image representation.

If the Moiré image in Fig. 1.3 is viewed in perspective with the third axis being brightness, the image would appear as a series of active peaks in regions with numerous changes in brightness and smoother regions or plateaus where the brightness levels varied little. In most cases, eight bit black and white images are used. That means the brightness will have a value ranging from 0 to 255 representing dark to bright in the image. Therefore, a digital image can be considered a matrix whose row and column indices identify a point in the image and the corresponding matrix element value identifies the gray level at the point. The small picture elements or pixels correspond to each element in the digital camera imager that converts light to an electrical charge. There are total 480×512 elements or pixels in the digital camera imager we used.

After a 2D Moiré image has been created, one has to use Eq. 1.2-1 to obtain quantitative values, such as the height, for some pixels in the 2D image through image processing. The fundamental objective of the Moiré image processing is to locate the center of each Moiré fringe by defining its (i, j) image indices since the Moiré fringes are usually wider than one pixel, and only the center lines can be treated as contour lines. When dealing with relatively coarse Moiré fringes, errors are therefore introduced. Due to a number of unforeseeable factors, human intervention is always needed through each step of the image processing. Some researchers have tried to develop software tools to process Moiré fringes automatically (Ning & Peng 1988, Moran & Lipczynski 1994, and Bruynooghe 1996), but that objective has yet to be completely achieved.

Moiré fringes themselves do not allow a direct determination of whether a contour line showing concentric fringes is a hill or a valley, which is another reason that data processing of Moiré fringes can not be done automatically. When an order number is assigned to a Moiré fringe, it is necessary to know whether the number is going up or down. Some enhancements have been proposed (Murakami & Murakami 1978, and Fujimoto *et al* 1992), however, these modifications make the setup and data analysis more complicated.

As shown in Eq. 1.2-3, the sensitivity of the Moiré measurement Δz is defined as the minimum distance between two successive Moiré contour lines. Therefore, any surface

change smaller than Δz can not be detected. Sensitivity has always been considered from the theoretical point of view (see Eq. 1.2-2 and Eq. 1.2-3), and in all cases it has been seen to depend proportionally on the factors d and l/b . The factor d has lower practical limits determined by the loss in definition of the shadow of the grating with increasing distance from the grating itself. This in turn is caused by the diffraction effect. The factor l/b is also limited by similar causes. The highest sensitivity (smallest Δz) can be attained with very flat objects. In most practical cases, however, the sensitivity is considered around 1/10 mm. Some special techniques used to improve the sensitivity have been reported (Han, Ifju & Post 1993, and Liao & Voloshin 1993). Again, these enhancements need special treatments in either the setup or the following data-processing procedure.

In many cases, one has to interpolate the Moiré fringes since only the height information of centerline points of each Moiré fringe is known. The height information of all other off-fringe-points is still unknown and sometimes only few Moiré fringes are available in some areas (Marshall *et al* 1993, Fang 1991, and Mckelvie 1986). The height information is calculated from Eq. 1.2-1 by using known optical geometrical parameters: l , d , and b . However, how accurate these parameters can be determined in a practical way is questionable. Small errors with b and l can be amplified to bring big errors to height z . With these in mind, the accuracy of height information could be worse depending on applications.

Finally, the Moiré methods usually have to assume a reference point in the field of view as a zero order fringe. This point is actually the origin of all height information, and all geometry is built on this origin. If we need to measure a surface twice, there will be two zero order fringes or reference points being created. One can combine all the data from these two measurements together only if the relationship of these two reference points remains known or unchanged in height direction during the measurements. 'Unchanged' means the reference points must be fixed during all the measurements. When entire surface area in the field of view is under rotation, translation and deformation, it is impossible to find a fixed point to be the zero order point, and unfortunately this is the case for most dynamic applications. That means Moiré methods are not applicable in

such cases unless a device is used to provide the information on these rigid body movements (Lin, Chawla, & Wagner 1997). Therefore, the measurement of the Moiré methods is generally a relative measurement, which can not determine the absolute position of the surface in 3D space.

Assuming all above-mentioned problems are solved, the final results obtained are the height information of image pixels with respect to a reference point in a form of a set of triple numbers (h, i, j) . For clarity, the height is denoted as h instead of z . This information (h, i, j) is still based on the 2D image plane. Fig. 1.6 shows the schematic of a CCD (charge coupled device) camera. As the most important component inside a CCD camera, the imager is a physical device composed of discrete silicon imaging elements, called the pixels. Each pixel is very sensitive to light and has a voltage output proportional to the intensity of the incident light. The 2D image plane is the plane of the CCD imager, which is perpendicular to the optical axis.

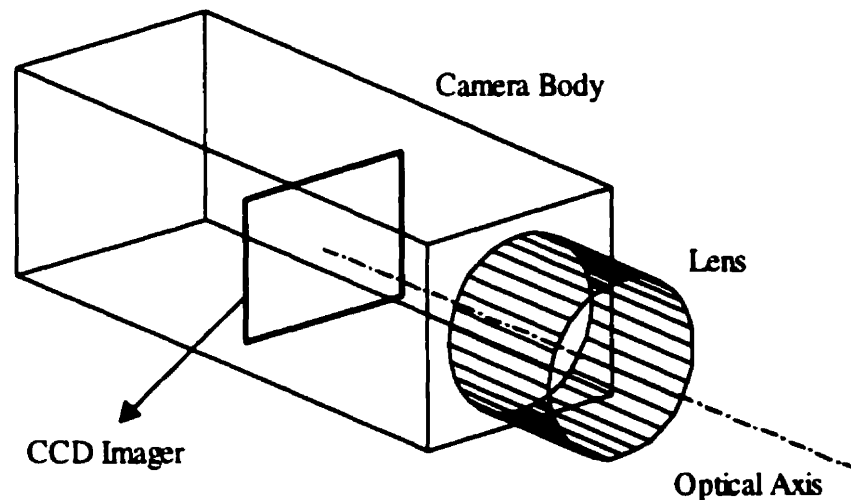


Fig. 1.6 Schematic of a CCD camera.

As mentioned earlier in this chapter, our world is characterized by the Cartesian coordinate system. Shape, position, deformation, and rotation are all described with respect to a Cartesian coordinate system. However, what is obtained directly from the Moiré methods are based on the image plane, whose position and orientation with respect

to a Cartesian coordinate system maybe unknown. Obviously, there is a gap between what can be obtained from the Moiré methods and what is needed to define a surface shape in 3D space—the 3D Cartesian coordinates, as mentioned in Section 1.1. For instance, from (h, i, j) one can not determine the exact diameter of a cylindrical surface. However, from (h, i, j) we do know qualitatively how many concave and convex areas are in a surface, and how much is the height difference between them. Even with these drawbacks, the Moiré methods have been used in various applications to date. Takasaki obtained some Moiré pictures on a human face and body (Takasaki 1970), and Hung used shadow Moiré to study vibrations (Hung *et al* 1977). For more application examples, see Pirodda's paper (1982) and Sciammarella's paper (1982). The applications so far were, in general, performed in the laboratory as a demonstration of the Moiré technique as a measuring device in a particular investigation. The features of the Moiré methods are summarized as follow:

- simple optical setup;
- difficulties in interpretation of Moiré fringes and fully automatic processing;
- ambiguity in convex and concave areas;
- need interpolation for off-fringe-points;
- sensitivity is a important factor for all applications;
- difficulties in the determination of optical parameters accurately;
- the measurement results are a set of (h, i, j) , not 3D Cartesian coordinates;
- relative measurement due to the assumption of a relative reference point on which the 3D geometry is based.

Some of the difficulties mentioned above are related with attempts at computer-based automatic data processing. In this point of view, the shadow Moiré and projection Moiré methods are called classic or geometric Moiré methods for fringe analysis by human observation rather than by computer processing.

In order to resolve the difficulties associated with the geometric Moiré methods, an alternative method called *the grating projection method or the grid projection method* has been proposed by several researchers (Takeda, Ina, & Kobayashi 1982, Takeda & Mutoh

1983, Toyooka & Iwaasa 1986, and Halioua & Liu 1989). Unlike the geometric Moiré methods, no Moiré fringes are generated by the interference between a reference grating and a deformed grating image. A deformed grating image projected on an object is directly analyzed without the use of a reference grating. Therefore, problems encountered in the geometric Moiré methods are minimized. The theory behind the grating projection method is that when a grating is projected onto a surface, the form of the grating image on the surface is determined only by the shape and position of the surface if the grating pitch and the optical setup (projection lens and projection orientation) are fixed. In other words, a 2D deformed grating image contains the surface shape information. It should be possible to calculate the shape of the surface from the deformed grating image directly. To use a reference grating to generate Moiré fringes as used in the geometric Moiré methods is only one of the ways to obtain shape information encoded in the deformed grating image. The grating projection method is used in this work, and its detailed description will be given in Chapter 2. In the following section, a brief review of the dynamic out-of-plane deformation measurement by using whole-field optical methods is given.

1.2.2 Dynamic Deformation Measurements by Using Optical Methods

A review of the literature shows that a number of studies have been done to deal with real-time measurement of dynamic out-of-plane deformation. Using high-speed photography to record the profile of transient deformation is usually the way to accomplish the dynamic measurement goal. Zhu, Goldsmith & Dharan (1992) photographed very high-speed projectiles penetrating Kevlar laminates. Senf, Strassburger & Rothenhausler (1997) employed a high-speed film camera in a shadow-optical arrangement to picture the dynamic out-of-plane deformation of composite armour at projectile impact. In above studies, the high-speed cameras were not digital cameras, and they record pictures on films. These pictures are limited to only one view (usually side view). Concerning the whole-field measurements, very few studies have been done so far, and these applications are the natural extension of the geometric Moiré methods. Unlike using standard frame rate cameras, high-speed framing film cameras were used in these studies. Chai (1982) conducted dynamic measurements on

compressed graphite/epoxy composites subjected to low-velocity out-of-plane impact by using the shadow Moiré method with a Hycam high-speed film camera (up to 40,000 frame/sec). More recently, Kokidko *et al* (1997) also employed the shadow Moiré method combined with high-speed photography to measure the deformation of glass fiber reinforced plastic panels at impact of projectiles. Lambros & Rosakis (1997) measured the dynamic deformation of fiber reinforced polymeric matrix composites by using coherent gradient sensing (CGS). Instead of (h, i, j) , the CGS provides the slope or the gradient of height $\partial h/\partial x$ with known image indices (i, j) at some locations of the recorded fringe image. An integration process has to be used to obtain height information.

As mentioned previously, the Moiré methods are a relative measurement technique (the same with the CGS). In order to find out a common reference for all the measurement data taken at different time, they need to assume that at least one point, in the dynamic scene, remains unchanged or fixed throughout the whole dynamic event, as shown schematically in Fig. 1.7.

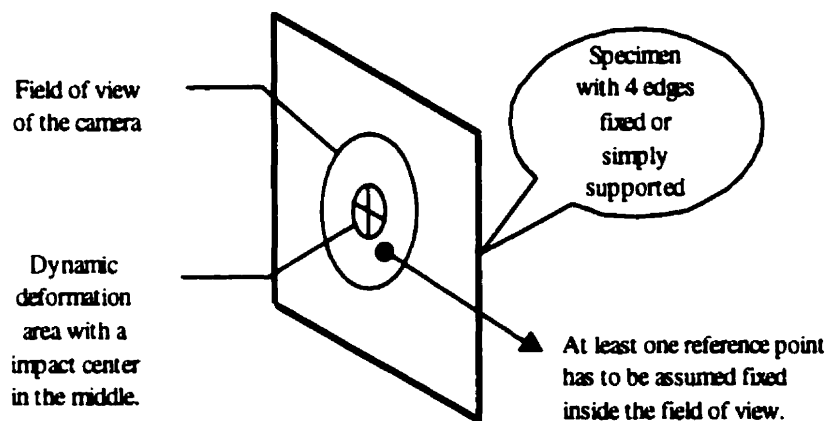


Fig. 1.7 Reference point used in optical dynamic measurements.

In Chai's Ph.D. thesis (1982), he assumed that 50 microseconds after impact by a $\varnothing 0.5$ inch projectile, the out-of-plane deformation at a point 0.5-inch away from the impact center is zero. The specimen used in his test was 0.2 inch thick. The same method to find a reference plane was also used by Kokidko *et al* (1997). They all implied that the

dynamic deformation was limited in the center as a localized deformation, and close to the boundary of the field of view of the camera the deformation was zero throughout the impact. This is valid for thick and stiff plates under high-speed impact, but the general failure mode of relative thin plates under low speed impact (150 ft/sec in Chai's thesis) is global buckling plus local delamination. Therefore, before any relative optical measurement techniques can be used, such as the Moiré methods, we have to make sure that the field of view of the camera is large enough to include some 'fixed' regions. For example, in Lambros & Rosakis' paper (1997), the field of view was approximately $\text{Ø}50$ mm out of a $152 \times 152 \times 6$ mm plate impacted with a $\text{Ø}25$ mm projectile. It is difficult to claim that any point 25 mm away from the impact center will remain fixed during the whole event, especially when the impact speed is as low as 1 m/sec.

Lin, Chawla & Wagner (1997) proposed a system to measure the out-of-plane deformation of two different tires of F-16 fighter jets by using a fringe projection technique and a standard CCD camera. In this very challenging application, no fixed point existed in the field of view and a fiber-optic sensor was employed to monitor the out-of-plane deformation of a reference point. Unfortunately, only static measurement results were presented in his paper, although this system was originally designated for both static and dynamic measurements.

All of these studies are extended applications of the geometric Moiré techniques. Therefore, all the difficulties associated with the geometric Moiré methods are still present. Despite the tedious data processing after the Moiré fringe images are taken, the most detrimental shortcomings that jeopardize the whole measurement results are the relativity of the measurement and the failure of providing 3D Cartesian coordinates with respect to a fixed coordinate system.

1.3 Objectives

Optical measurement techniques and the optical dynamic out-of-plane deformation measurement techniques reviewed in the previous section indicate that existing techniques for dynamic out-of-plane deformation measurement have some detrimental

limitations. Thus, there is no standard methodology to measure the transient deformation of a structure under dynamic events, such as impact. On the other hand, a reliable treatment of complicated structural dynamic problems should be validated by experimental data. It is with this philosophy in mind that this research work is undertaken. The objectives of this work are:

- To develop an optical 3D-measurement method that can provide 3D Cartesian coordinate information as its measurement results. Accomplished with automatic data processing;
- To verify the measurement accuracy;
- To develop a dynamic 3D surface measurement system by integrating the optical measurement technique with a high-speed digital camera;
- To apply the dynamic 3D surface measurement system in practical applications.

The original contributions to knowledge are described in detail later at the end of the thesis.

1.4 Thesis Outline

This thesis is divided into four parts:

- Chapter 2, 3, and 5 deal with the optical method used in this work. Chapter 2 covers the basic principles of the optical measurement. The calibration technique is described in Chapter 3, and Chapter 5 includes some accuracy test results;
- Chapter 4 gives a detailed description of the high-speed measurement system in terms of hardware specifications;
- Chapter 6 deals with the practical applications of the dynamic 3D surface measurement system. The application is the polymer sheet inflation test;
- Chapter 7 presents a finite-element simulation of polymer sheet inflation tests.

The last chapter concludes the thesis, and indicates some possible future developments.

CHAPTER 2

OPTICAL MEASUREMENT METHODS

2.1 Introduction

In this research, the grating projection and Fourier transform technique is employed as the fundamental methodology to build-up the high-speed optical 3D measurement system. As described in Chapter 1, the grating projection method is more applicable than the geometric Moiré methods in the following aspects:

- (1) automatic data processing;
- (2) non-ambiguities in convex and concave areas;
- (3) no need to do the data interpolation;
- (4) higher measurement sensitivity.

Due to these factors, the grating projection and Fourier transform method is an appropriate candidate for this project. The details of the grating projection method are described in Section 2.2. As the most important component of this method, the Fourier transform technique is outlined in Section 2.3. In the final section of this chapter, the phase unwrapping problem and several unwrapping algorithms are addressed.

2.2 Grating Projection Surface Shape Measurement

2.2.1 Fundamental of Gratings

As shown in Fig. 2.1, the gratings used in this work are evenly spaced lines running parallel to each other, and are usually printed or etched on thin glass substrate. The line width is equal to the space width next to it. Sometimes, this type of grating is called the Ronchi grating to distinguish from other grating types, such as the diffraction grating. The distance between the center of a black line to the center of the next black line is a characteristic property of the grating, called the pitch or the frequency.

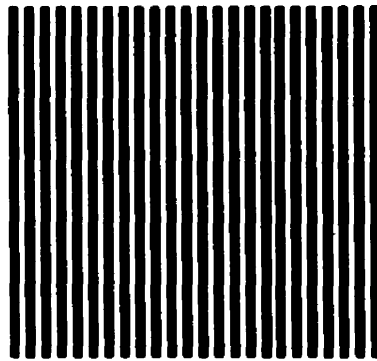
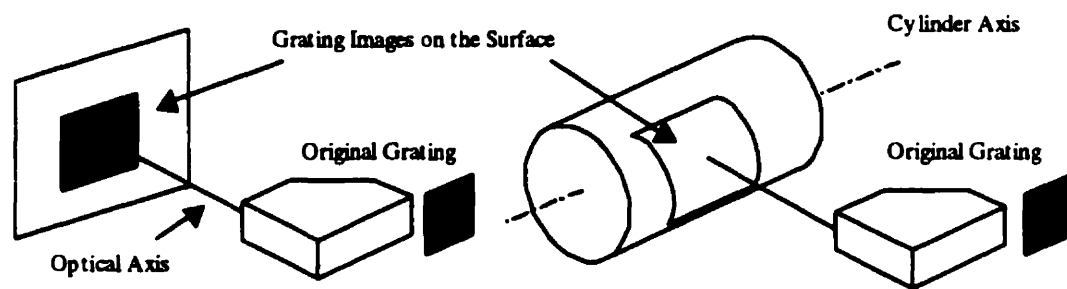


Fig. 2.1 Ronchi grating

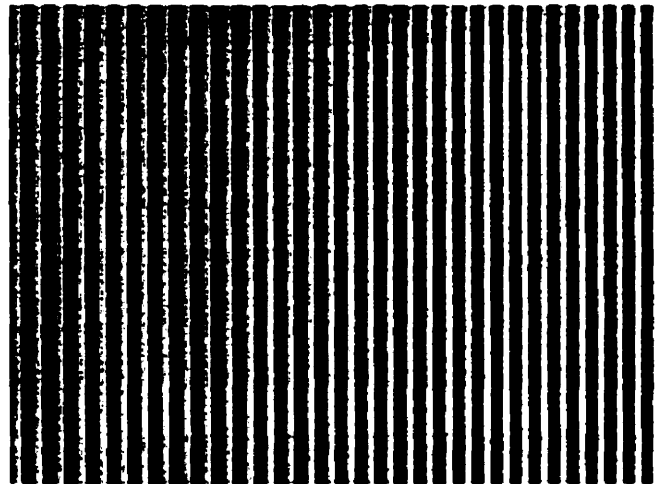
When a Ronchi grating is projected onto a surface, the form of the grating pattern on the surface is determined by both the shape of the surface and the angle of projection. If the grating and the optical configuration are fixed, the only factor that determines the form of the grating pattern on the surface is the surface shape itself. When an equispaced line grating is projected onto a flat surface, it will give an image with equispaced straight lines. The same grating projected onto a cylindrical surface can give either an image of straight lines with varying spacing or an image of curves of varying spacing and its shape depending on the relative orientation of the cylinder and the grating. Fig. 2.2 shows the different grating images given by the same grating when it is projected onto different surfaces with different orientations. The original grating, which is used in the projection, is also shown in the figure. Actually, the original grating is mounted inside a projector that is fixed with a CCD camera in a box, which is called the sensor head, which is also shown in the figure. Fig. 2.2 (c) and (d) show the deformed grating images obtained from these two simple cases, respectively. For Fig. 2.2 (c), the deformed grating image looks like the original grating, but with different and varying spacing. For Fig. 2.2 (d), the straight lines in the original grating bend into curved lines with varying spacing.



(a) Optical axis perpendicular with the flat surface.

(b) Grating lines are perpendicular with the cylinder axis.

(c)



(d)

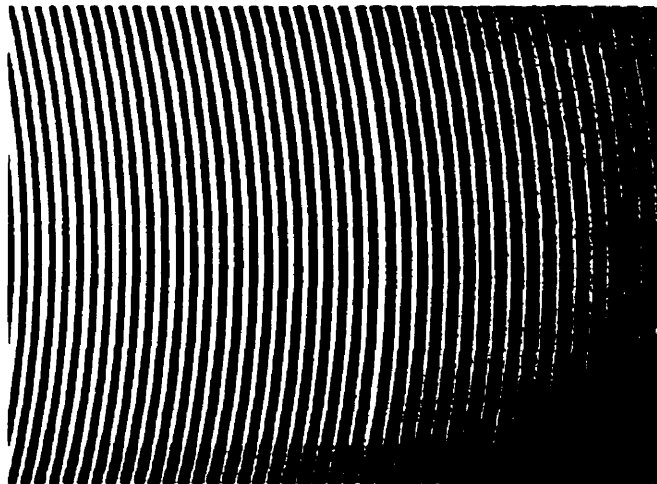


Fig. 2.2 Grating images on flat and cylindrical surfaces: (a) setup for a flat surface; (b) setup for a cylindrical surface; (c) deformed grating image on the flat surface; (d) deformed grating image on the cylindrical surface.

Since the form of the projected grating image is determined by the surface shape, it should be possible to calculate the surface shape from the grating pattern formed on the surface if the projection and viewing geometry are known. In other words, the deformed grating pattern contains the surface shape information. The problem here is limited to how to extract or obtain the surface shape information from the deformed grating image. It should be recalled that the geometric Moiré methods use an additional grating (known as the reference grating) to 'filter' the deformed grating image to generate the Moiré fringes, which are treated as contour lines of the surface, as shown in Fig. 1.3. This method, to employ an additional grating as a reference to obtain the surface shape information, is considered as one of the ways to achieve the goal. In this chapter, we will see other ways to obtain the surface shape information out of a deformed grating image. These ways are usually more efficient and practical than that used by the geometric Moiré methods. First, the mathematical representation of grating images will be analyzed.

2.2.2 Mathematical Modeling of Grating Images

In this work, the gratings considered are one-dimensional gratings such as shown in Fig. 2.3. In addition, the coordinate system used to describe the light intensity distribution of the grating is shown in Fig. 2.3.

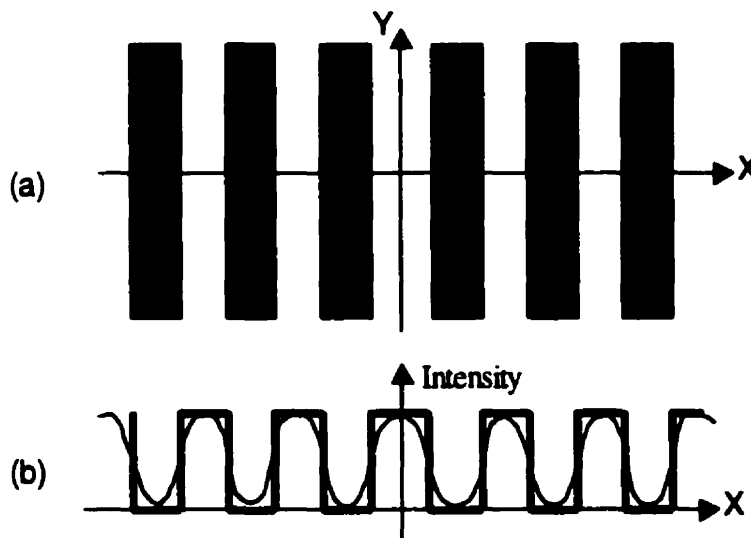


Fig. 2.3 Intensity distribution of a grating; (a) grating image, (b) intensity distribution along the X-axis.

We have to make two basic assumptions in order to develop the mathematical equations to represent the intensity distribution of gratings: (1) the CCD camera used to acquire the digital image of grating patterns has adequate resolution to show the regularity of the grating images, such as the frequencies; (2) the frequency of the grating used should be at least twice that of the highest frequency induced by surface shape. As shown in Fig. 2.2, a grating image is modulated by the surface shape after being projected onto this surface. The frequency of this deformed grating image is no longer uniform due to the overlapping of the original grating frequency and the frequencies induced by surface shape. This condition assures that different frequency terms are separable in the frequency domain. The above two conditions are mutually competing with each other. However, both can be satisfied in most practical cases. In our case, 20 line/inch gratings and 512×480 pixel resolution of the CCD camera are employed with the field of view of approximately 100×100 mm. Under this configuration, there are approximately 9 pixels for one cycle of the grating.

The real intensity distribution along the X -axis of the original grating is in the form of a square wave. After being projected onto the surface and digitized by a CCD camera, the square wave will lose its sharp corners and turn into a periodic curve. This is because the light source is not a single-point source and the light rays are not exactly parallel to each other. Another reason is that some pixels will have dark grating lines occupying only half of the pixel's area. Table 2.1 shows a portion of the real light intensity distribution of a grating image along the X -axis.

$I(x)$	164	130	75	41	47	89	139	162	149	100	52	42	65	123	158
x (pixel)	1	2	3	4	5	6	7	8	9	10	11	12	13	14	15

Table 2.1 Light intensity distribution of a portion of a grating image.

Since any function can be represented by the sum of its harmonic sine or cosine components (known as the Fourier series), a periodic intensity distribution function can be represented as an infinite series of cosine or sine terms (Gonzalez-Velasco 1995):

$$I(x) = \sum_{n=0}^{\infty} b_n(x) \cdot \cos(n\Phi(x) + 2n\pi \cdot f \cdot x) \quad (2.2-1)$$

Here, $I(x)$ is the intensity distribution along the X-axis, $b_n(x)$ are the spatially dependent harmonic amplitudes, f is the grating frequency, and $\Phi(x)$ is the phase map corresponding to the surface shape. Eq. 2.2-1 is a general form and can be simplified or truncated by assuming only the first two terms are considered. Therefore, Eq. 2.2-1 can be re-written as:

$$I(x) = b_0(x) + b_1(x) \cdot \cos(\Phi(x) + 2\pi \cdot f \cdot x) \quad (2.2-2)$$

Where, $b_0(x)$ represents the background intensity and $b_1(x)/b_0(x)$ the grating pattern contrast. In practice both $b_0(x)$ and $b_1(x)$ will be modified at each location by noise, by variations in surface texture, and possibly due to non-uniform lighting. As indicated previously, $\Phi(x)$ is the phase map that represents the surface shape. This claim is examined more closely in the following paragraphs.

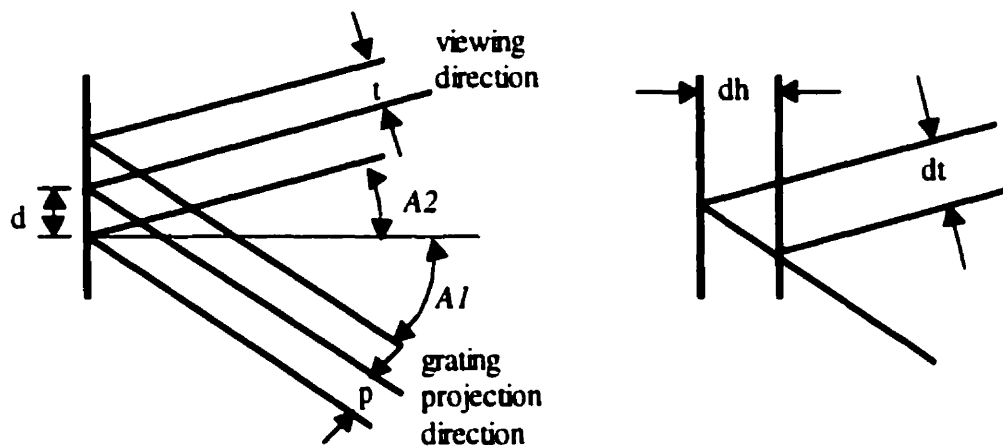


Fig. 2.4 Left--grating projected onto a surface; Right--change in grating spacing with the change of surface position.

As shown in Fig 2.4, a grating is projected onto a surface at an angle $A1$, and the grating image on the surface is viewed through a lens at an angle $A2$. If the original grating has a

pitch of p , the pitch of the grating image on the surface is called d and it is given by the following equation.

$$d = p / \cos A1$$

The light viewed by the camera will have an intensity variation with the pitch of t given by

$$t = d \cdot \cos A2 = p \cdot \cos A2 / \cos A1$$

Now if the surface moves a distance dh , as shown in the Fig. 2.4, there will be a change in t in the viewing direction. The change is dt and it will be equivalent to the shift of the grating due to the change in the surface position. That is, the phase shift $\Phi(x)$, in Eq. 2.2-2. The phase shift can then be given by

$$\Phi = 2\pi \cdot \frac{dt}{t}$$

As shown in Fig. 2.4, we have

$$dt = dh \cdot (\tan A1 + \tan A2) \cdot \cos A2$$

and so

$$\Phi = \frac{2\pi \cdot dh \cdot [\tan A1 + \tan A2] \cdot \cos A1}{p} \quad (2.2-3)$$

This equation indicates that the height variation, dh , at a point on a surface may be obtained by an evaluation of the change of phase, Φ , of a sinusoidal grating projected onto the surface. It verifies the previous claim that the phase mapping is related to the surface shape directly if the optical geometry is fixed. The basic problem, therefore, is how to recover the phase, Φ , for each pixel of a deformed grating image. The next section will introduce the different methods developed in the past to achieve this goal.

2.2.3 Methods to Extract Phase Information

(1) Phase Shift or Phase Stepping

Upon translation of the projection grating by a fraction $1/N$ of its pitch p , the phase of the deformed grating image represented by Eq. 2.2-2 is shifted by $2\pi/N$, yielding a new intensity function I_n . Using three, or more conveniently four, intensity functions corresponding to different phase shifted values, the phase Φ can be retrieved independently from the other parameters in Eq. 2.2-2. For example, in the four-phase step algorithm, if shifting the phase by $\pi/2$ increments:

$$\begin{aligned} I_1 &= A + B \cdot \cos(\Delta) \\ I_2 &= A + B \cdot \cos(\Delta + \pi/2) = A - B \cdot \sin \Delta \\ I_3 &= A + B \cdot \cos(\Delta + \pi) = A - B \cdot \cos \Delta \\ I_4 &= A + B \cdot \cos(\Delta + 1.5\pi) = A + B \cdot \sin \Delta \end{aligned}$$

$$\Delta = \arctan\left(\frac{I_4 - I_2}{I_1 - I_3}\right) \quad (2.2-4)$$

where, functions $A(i, j)$ and $B(i, j)$ represent b_0 and b_1 functions in Eq. 2.2-2, respectively. The symbol Δ represents $(\Phi + 2\pi \cdot f \cdot x)$ both modulated and unmodulated components. If necessary, the unmodulated phase component $2\pi \cdot f \cdot x$ must be subtracted to leave the required modulated phase component Φ . Since the arctangent function is restricted to generate a value in the range of $-\pi$ and $+\pi$, calculated raw phase mapping Φ is wrapped into this range, and a phase unwrapping scheme is needed to produce a continuous phase distribution. The details of phase unwrapping schemes are given in Section 2.4.

The phase shifting technique, when compared with direct geometric measurement of the interferogram (such as in the geometric Moiré methods), is characterized by several superior features:

- High precision-permitting interpolation to 1/1000 of a fringe order.
- Low sensitivity to background, contrast variations, and noise.

- Measurement over a uniform rectangular array of points defined by the imager, ready for further mathematical manipulation.
- Easy automation with readily available computers and solid state array detectors such as CCD, CID array-cameras.

However, the phase shifting method needs a precision translation mechanism to realize the small, but accurate, movements of the grating. In addition, both the object and the optical setup are required to be fixed and vibration-free during different shifting stages. In order to obtain the phase information, at least three frames of the deformed grating image are required. This means the phase shifting technique is not applicable in the measurement of transient deformation, which is required in this work.

(2) Fourier Transform

The phase shifting and Fourier transform techniques are the two most established methods to retrieve phase information from deformed grating images. Unlike the phase shifting method, only one deformed grating image is necessary for the Fourier transform method in the calculation of the phase. This feature is very attractive to this work due to the original objective of measuring surface under transient deformation. The Fourier transform technique, therefore, is the method used in this work to conduct phase calculations. The details of the Fourier transform processing are given later in Section 2.3. The main steps in the processing are listed as follows:

- Capture a deformed grating image and Fourier transform it into the frequency domain;
- Bandpass filter the spectrum signal in the frequency domain to remove unwanted signal components;
- Shift the isolated harmonic component to the origin of the power spectrum to remove the unmodulated grating frequency;
- Inverse Fourier transform the modulated signal to create its real and imaginary components;
- Calculate the phase from the real and imaginary components.

(3) Sinusoidal Fitting

As a simplified approximation to the Fourier transform method, Mertz (1983) suggested a sinusoidal fitting method to obtain similar phase information based on the pioneering work of Bruning *et al* (1974). Mertz first developed an electronic fringe evaluation processor, which was able to extract the phase of the fringes in video real-time analog signals, by assuming the phase step is $2\pi/3$ from one sampling point to the next and the mean intensity and the modulation of the fringe are constants in the small range of three sampling points. Then Macy (1983) followed this idea by implementing the algorithm using standard digital image processing technology. As described in Section 2.2.2, the measured intensity at one pixel of the CCD camera could be expressed as:

$$I(x) = b_0(x) + b_1(x) \cdot \cos(\Phi(x) + 2\pi \cdot f \cdot x)$$

With an increasing spatial coordinate x , the term $(\Phi + 2\pi \cdot f \cdot x)$ is also increasing. Here f is an average spatial frequency, and the grating is oriented in the Y direction. If the spacing of the grating is adjusted so that the phase step is $2\pi/4$ from one pixel $x(i)$ to the next pixel $x(i+1)$, each grating line occupies 4 pixels. In the meantime, it is assumed that the mean intensity $b_0(x)$ and the modulation $b_1(x)$ of the grating don't change in the small range from the left neighbor pixel $x(i-1)$ to the right neighbor pixel $x(i+1)$. The phase $\Phi(x)$ at the pixel $x(i)$ is derived from the approximation of the measured intensities $I(x)$ around the pixel position. By using trigonometric identities, the above equation can be re-written as:

$$\begin{aligned} I(x) &= b_0(x) + b_1(x) \cdot \cos(\Phi(x) + 2\pi \cdot f \cdot x) \\ &= b_0(x) + b_1(x) \cdot \cos \Phi(x) \cdot \cos(2\pi \cdot f \cdot x) - b_1(x) \cdot \sin \Phi(x) \cdot \sin(2\pi \cdot f \cdot x) \end{aligned}$$

Let $c_1(x)$ equal $b_1(x) \cdot \cos \Phi(x)$ and $c_2(x)$ equal $-b_1(x) \cdot \sin \Phi(x)$. The equation can then be expressed as:

$$I(x) = b_0(x) + c_1(x) \cdot \cos(2\pi \cdot f \cdot x) + c_2(x) \cdot \sin(2\pi \cdot f \cdot x) \quad (2.2-5)$$

Again, it is assumed that $c_1(x)$ and $c_2(x)$ vary slowly in a local neighborhood, so that they may be taken as constants in that neighborhood. These constants can therefore be found by fitting Eq. 2.2-5 through the gray levels of four successive pixels.

$$c_1(x_i) = I(x_{i-1})\cos(2\pi fx_{i-1}) + I(x_i)\cos(2\pi fx_i) + I(x_{i+1})\cos(2\pi fx_{i+1}) + I(x_{i+2})\cos(2\pi fx_{i+2})$$

$$c_2(x_i) = I(x_{i-1})\sin(2\pi fx_{i-1}) + I(x_i)\sin(2\pi fx_i) + I(x_{i+1})\sin(2\pi fx_{i+1}) + I(x_{i+2})\sin(2\pi fx_{i+2})$$

Finally, we will get the phase information for each pixel by following the equation:

$$\Phi(x_i) = \arctan\left(\frac{-c_2(x_i)}{c_1(x_i)}\right) \quad (2.2-6)$$

This method to obtain phase information works well when the grating frequency does not vary too much across the whole image. In situations, when it is hard to maintain the 4 pixels per grating line assumption everywhere, the result is that the phase steps between adjacent pixels are not $\pi/4$ as they should be, but have some smaller or greater value. The final calculated phase has many errors inside, and the error is intrinsic to the method. This may be one reason why the sinusoidal fitting technique was not given much attention in recent years.

2.3 Fourier Transform Phase Calculation

2.3.1 Basics

The Fourier transform is a commonly used tool in signal processing and digital image processing. This is because the Fourier transform can decompose a signal (1D) or an image (2D) into a set of cosines and sines, each of which represents the corresponding frequency components of the signal or the image intensity itself. Furthermore, most features believed to be important for solving image processing tasks are often more easily described in the frequency domain than in terms of the variation of the image itself. Examples of such features are orientation, phase, frequency and curvature. This section presents the basics of the continuous Fourier transform.

Let $f(x)$ be a continuous function of a real variable x . The Fourier transform of $f(x)$, denoted $F(u)$, is defined by the following equation.

$$F(u) = \int_{-\infty}^{\infty} f(x) \cdot \exp[-2\pi i \cdot ux] dx \quad (2.3-1)$$

Where $i^2 = -1$. Given $F(u)$, $f(x)$ can be obtained by using the inverse Fourier transform:

$$f(x) = \int_{-\infty}^{\infty} F(u) \cdot \exp[2\pi i \cdot ux] du \quad (2.3-2)$$

Equations 2.3-1 and 2.3-2, called the Fourier transform pair, exist if $f(x)$ is continuous and integrable and $F(u)$ is integrable. These conditions are usually satisfied in practice. The Fourier transform of a real-valued function $f(x)$ is generally complex, that is,

$$F(u) = R(u) + i \cdot I(u) \quad (2.3-3)$$

where $R(u)$ and $I(u)$ are the real and imaginary components of $F(u)$, respectively. The magnitude function $|F(u)|$, called the Fourier spectrum of $f(x)$ is defined as:

$$|F(u)| = \sqrt{R^2(u) + I^2(u)} \quad (2.3-4)$$

The variable u appearing in the Fourier transform often is called the frequency variable. This name arises from expression of the exponential term $\exp[-2\pi i \cdot ux]$. According to Euler's formula,

$$\exp[-2\pi i \cdot ux] = \cos 2\pi ux - i \cdot \sin 2\pi ux \quad (2.3-5)$$

Interpreting the integral in Eq. 2.3-1 as a limit summation of discrete terms makes it evident that $F(u)$ is composed of an infinite sum of sine and cosine terms and that each value of u determines the frequency of its corresponding sine-cosine pair. Fig. 2.5 shows a simple function and its Fourier spectrum. The first component actually has zero frequency because it represents the mean amplitude of the signal, and it sometimes called the DC term. The first non-zero frequency component is known as the fundamental component.

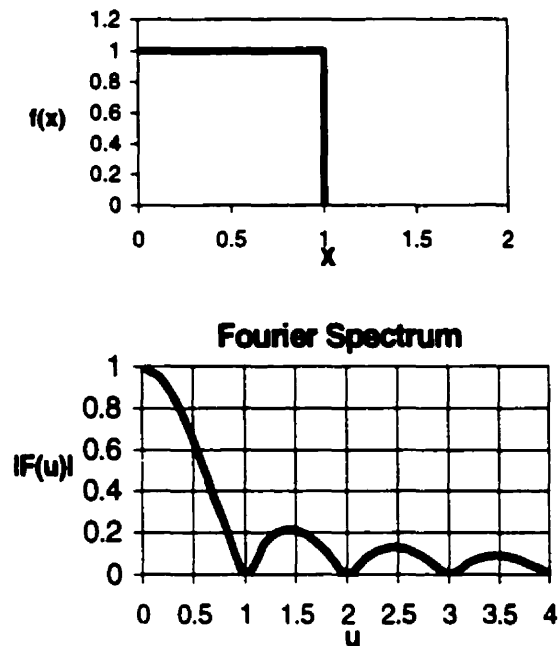


Fig. 2.5 A simple function and its Fourier spectrum.

The Fourier transform can be easily extended to a function $f(x, y)$ of two variables. If $f(x, y)$ is continuous and integrable and $F(u, v)$ is integrable, the following Fourier transform pair exists:

$$F(u, v) = \iint_{-\infty}^{\infty} f(x, y) \cdot \exp[-2\pi i(ux + vy)] dx dy \quad (2.3-6)$$

$$f(x, y) = \iint_{-\infty}^{\infty} F(u, v) \cdot \exp[2\pi i(ux + vy)] du dv \quad (2.3-7)$$

where u and v are the frequency variables. As in the one-dimensional case, the Fourier spectrum is:

$$F(u, v) = R(u, v) + i \cdot I(u, v) \quad (2.3-8)$$

$$|F(u, v)| = \sqrt{R^2(u, v) + I^2(u, v)} \quad (2.3-9)$$

2.3.2 Discrete Fourier Transform

In the context of image processing and machine vision, the images under consideration are usually digitized. Such images have dimensionality two, are real-valued, and are defined on a rectangular discrete point grid with finite extension in both dimensions. Hence, to actually compute the Fourier transform of such an image, the discrete Fourier transform must be used, as a sufficiently good approximation of the continuous transform. The following provides an introduction of discrete Fourier transform without further proofs for each of the equation. For further evidence, please see Brigham's book (1974).

Suppose that a continuous function $g(x)$ is discretized into a sequence

$$\{g(x_0), g(x_0 + \Delta x), g(x_0 + 2\Delta x), \dots, g(x_0 + [N-1]\Delta x)\}$$

by taking N samples Δx units apart. In other words, the sequence $\{g(0), g(1), g(2), \dots, g(n)\}$ ($n=N-1$) denotes any N uniformly spaced samples from a corresponding continuous function. The discrete Fourier transform pair that applies to sampled functions is given by

$$G(u) = \frac{1}{N} \sum_{n=0}^{N-1} g(n) \cdot \exp[-2\pi i n u / N] \quad (2.3-10)$$

for $u = 0, 1, 2, \dots, N-1$, and

$$g(n) = \sum_{u=0}^{N-1} G(u) \cdot \exp[2\pi i n u / N] \quad (2.3-11)$$

for $n = 0, 1, 2, \dots, N-1$.

The values $u = 0, 1, 2, \dots, N-1$ in the discrete Fourier transform, Eq. 2.3-10, correspond to samples of the continuous transform at values $0, \Delta u, 2\Delta u, \dots, (N-1)\Delta u$. The sampling increments in the spatial and frequency domains are related by the following equation.

$$\Delta u = \frac{1}{N \cdot \Delta x} \quad (2.3-12)$$

In the two-variable case the discrete Fourier transform pair is

$$G(u, v) = \frac{1}{MN} \sum_{m=0}^{M-1} \sum_{n=0}^{N-1} g(m, n) \cdot \exp[-2\pi i(um/M + vn/N)] \quad (2.3-13)$$

for $u = 0, 1, 2, \dots, M-1, v = 0, 1, 2, \dots, N-1$, and

$$g(m, n) = \sum_{u=0}^{M-1} \sum_{v=0}^{N-1} G(u, v) \cdot \exp[2\pi i(um/M + vn/N)] \quad (2.3-14)$$

for $m = 0, 1, 2, \dots, M-1, n = 0, 1, 2, \dots, N-1$.

Sampling of a continuous function is now in a 2D grid, with divisions of width Δx and Δy in the X and Y directions, respectively. As in the 1D case, the discrete function $g(m, n)$ represents samples of the function $g(x_0+m\Delta x, y_0+n\Delta y)$ for $m = 0, 1, 2, \dots, M-1$ and $n = 0, 1, 2, \dots, N-1$. Similar to the 1D case, the sampling increments in the spatial and frequency domains are related by the following equations.

$$\Delta u = \frac{1}{M \cdot \Delta x} \quad (2.3-15)$$

and

$$\Delta v = \frac{1}{N \cdot \Delta y} \quad (2.3-16)$$

The Fourier spectrum of 1D and 2D discrete function also are given by Eq. 2.3-4 and Eq. 2.3-9, respectively. The only difference is that the independent variables are discrete.

The principal purpose of this section is to present a theoretical foundation of the Fourier transform. Within this framework, the essential points necessary for a basic understanding of the Fourier transform are developed and illustrated. Transform theories,

especially the Fourier transform, have played a central role in the development of image processing as a formal discipline. In the following section, we will consider how to use the Fourier transform to process the deformed grating images to obtain the phase information we wanted.

2.3.3 Phase Calculation by the Fourier Transform

The deformed grating images, as shown in Fig. 2.2, are two-dimensional discrete functions. As mentioned previously, the surface shape information is modulated in the grating image along with other information, such as the background light intensity, noise caused by surface irregularities and the intensity distribution of a sinusoidal grating. All this information is mixed together. Moreover, it is very difficult to isolate and to extract the surface shape information by manipulating directly the pixels of a deformed grating image. Things, which are hard to deal with in the spatial domain, are sometimes easy to achieve in the frequency domain, and this is the case in the analysis of a deformed grating image.

Here we consider the information contained in a deformed grating image. First, the background light intensity over the field of view of a camera is the average of the illumination of the grating projector. The average of the illumination does not change much over the field of view if the surface is smooth. Hence, the background light intensity is a very low frequency signal in this case, and sometimes is the same as the direct current (DC) component of an electrical signal. The noise caused by surface irregularities or electronic noise is a sharp change in light intensity. Usually, they are random and relatively in small size. These kind of random noises are high-frequency signals. Another regularity in a deformed grating image is due to the grating itself. This is a sinusoidal signal with a certain frequency, called the carrier frequency, which is decided by the pitch of the original grating. Compared with the grating modulation caused by the surface shape, the carrier frequency is definitely higher. Therefore, the signal of the grating modulation caused by the surface shape is a low-frequency component. All the information or signals contained in a deformed grating image have

different corresponding frequencies. This is the foundation of using the Fourier transform to separate them in the frequency domain.

Takeda & Mutoh (1982) initially employed the Fourier transform to analyze deformed grating images for topological investigations. The steps of processing are as follows:

- The intensity distribution of a deformed grating image is 1D Fourier transformed into the frequency domain for the variable x only (perpendicular to the grating direction), with y being fixed;
- Bandpass filter the spectrum signal in the frequency domain to remove unwanted signal components, such as the DC component and the high-frequency components; After filtering, only the first low-frequency component is left;
- Shift the isolated harmonic component to the origin of the power spectrum to remove the unmodulated grating frequency;
- Inverse Fourier transform the modulated signal to create its real and imaginary components;
- Calculate the phase from the real and imaginary components by using the following equation.

$$\Phi(m, n) = \arctan \left\{ \frac{\text{Im}[p(m, n)]}{\text{Re}[p(m, n)]} \right\} \quad (2.3-17)$$

Here, $\text{Re}[p(m, n)]$ and $\text{Im}[p(m, n)]$ denote the real and imaginary parts of the inverse Fourier transform, respectively. Due to the features of the arctangent function, the unambiguous phase is wrapped into a range of $-\pi - \pi$. In order to produce a continuous phase distribution, phase-unwrapping schemes are required, which is the topic of the next section. Figure 2.6 shows an example of the phase calculation by using the Fourier transform. Fig. 2.6 (a) is the deformed grating image. Fig. 2.6 (b) is the intensity distribution of a line perpendicular to the grating. In order to see the modulation clearly, an unmodulated signal with the grating frequency is also shown in the graph. Fig. 2.6 (c) is the Fourier spectrum in the frequency domain. We can see different frequency

components are separated from each other by approximately the carrier frequency f_0 . The second peak in the frequency domain is easily located by an amplitude counting operation. Then the filtering in the frequency domain is carried out by applying a window in which those points lying inside the window preserve their values and the rest of the data is set to zero. The filtering window size can be defined by using the middle points between the first/second peaks and the second/third peaks, respectively. After the inverse Fourier transform, Fig. 2.6 (d) shows the wrapped phase distribution along the line with 2π discontinuities.

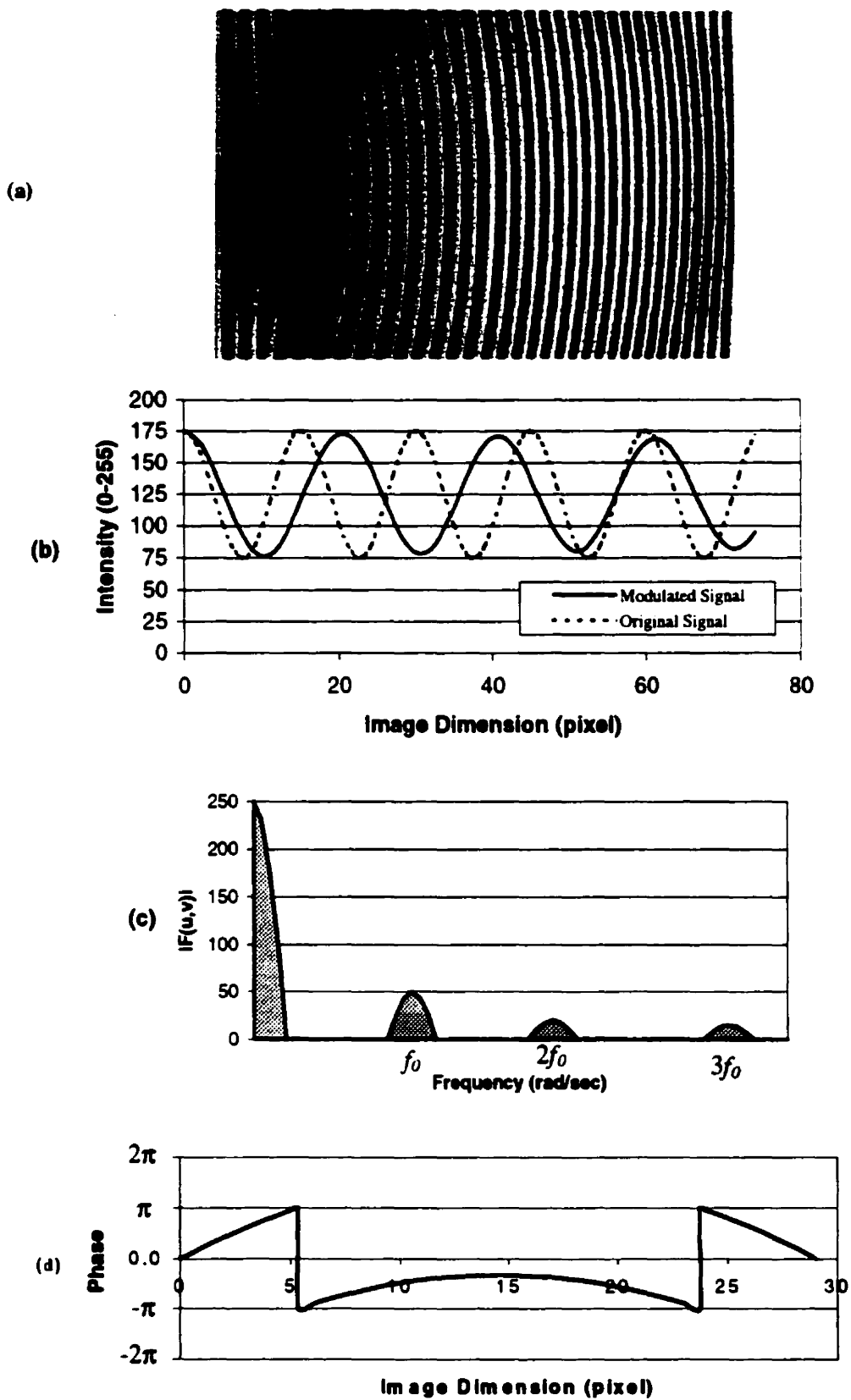


Fig. 2.6 Phase calculation by the Fourier transform.

2.4 Phase Unwrapping

In the previous sections, different techniques are introduced for the automatic analysis of deformed grating images. All these techniques, the phase-shifting, the sinusoidal fitting, and the Fourier transform method, yield a phase pattern with wrapped phase values ranging from $-\pi$ to π . Therefore, they contain 2π discontinuities or jumps even for a continuous surface. Fig. 2.7 shows a wrapped phase map in a normalized form using a gray scale to represent phase. The intensity ranges from black at one extreme, representing a phase value of $-\pi$, to intense white at the other representing a phase value of π .



Fig. 2.7 Wrapped phase map.

The purpose of the phase unwrapping is to remove these 2π discontinuities by shifting phase values by 2π or -2π of certain points to generate a continuous phase distribution over the whole field of view for continuous surfaces. As shown in Fig. 2.6 (d), a portion of the cross section line with phase values out of $-\pi$ to π range is wrapped. By adding 2π to its phase values for these wrapped points, it is possible to create a continuous phase distribution, shown in Fig. 2.8.

However, in practice wrapped phase images contain noise, small or large size, or even some large-scale inconsistencies, for example when there is a hole in the surface. Any unwrapping algorithm that fails to detect noise and inconsistencies will make a faulty unwrapping decision at any single point, and, even worse, this error will be carried on to

other noise-free points. Therefore, the noise can propagate to affect the whole unwrapping result. An appropriate phase unwrapping algorithm should be able to tackle noisy data to isolate the effect of noise. Several different algorithms have been proposed so far. They fall into two categories—the point-by-point algorithm and the region-by-region algorithm. In the following sections, the phase unwrapping algorithm used in this work is described, which is region-based. In order to compare with other unwrapping algorithms, some point-by-point unwrapping techniques are outlined first.

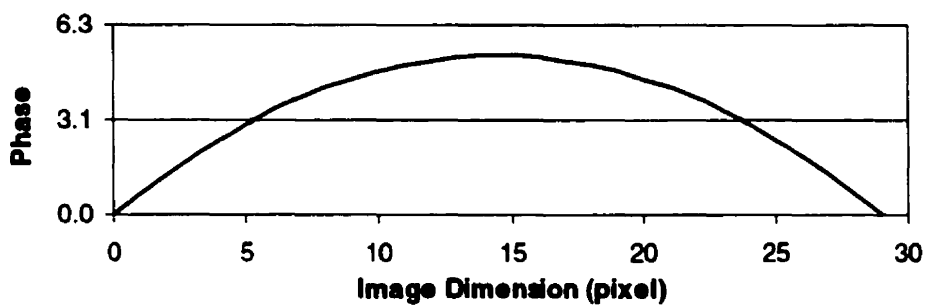


Fig. 2.8 Unwrapped phase distribution along a line.

2.4.1 Point-by-point Unwrapping Algorithm

(1) Scanning line approach for phase unwrapping

The procedural steps of the scanning line approach are described below:

- The digitized grating images are filtered to eliminate noise. A 3×3 spatial averaging filtering usually performs this process. A wrapped phase map is then computed by either the phase shifting or the Fourier techniques. The phase is related to the surface shape other than at those 2π discontinuities.
- The phase map is traced horizontally on a scan line by scan line basis. The 2π discontinuities may be found by seeking a phase change over a specified threshold level. A threshold level of π is normally used. This places a limit on the permitted rate of change of phase to be less than π between two adjacent pixels. A phase sum is kept of the discontinuities passed, up by 2π or down by 2π .

depending on the direction of phase roll over. This is seen, respectively, as a rapid white/black or a black/white transition (assuming phase is shown in gray scale with $-\pi$ as black and white as π). This phase sum is added to the phase values of successive pixels.

- The horizontal traces are, at this point, independent of each other. In order to bring them into their correct relative positions a single vertical trace of unwrapped phase is used. Various strategies may be applied to select a good candidate for this arranging trace, usually the central column.
- At the conclusion of this unwrapping process an unwrapped phase map is obtained.

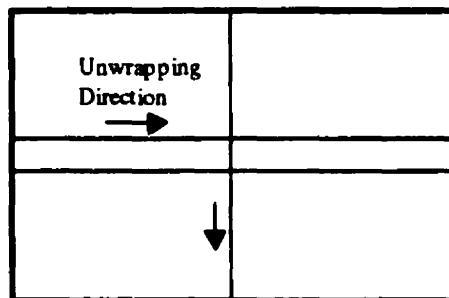


Fig. 2.9 Scanning line approach for phase unwrapping.

There are several variations on this theme. The roles of the horizontal and vertical traces might be reversed to give a better result for a given phase map, for instance. The algorithm relies on the quality of the raw phase map. However, there can be no guarantee that, even after filtration, noise in the raw phase map will disappear. The behavior of the 2π jump detection is an important factor. The 2π jump must always be distinguished by at least the threshold level of the detection procedure. Any failure is carried across the phase map and may disrupt many points of any particular scan line in the phase map. For more details, see Nakadate & Saito's paper (1985).

(2) Noise-immune cut method of phase unwrapping

The phase unwrapping method described in this section is an enhancement of the scanning line unwrapping algorithm. The basis of the algorithm is to place cuts, on a scan line by scan line basis, between points of phase discontinuity in order to minimize the length of the propagated discontinuity. The size of the discontinuity is termed the cut length. A simple means of flagging possibly inconsistent points is implemented by checking all 2×2 pixel areas in the phase map according to the procedure shown in Fig. 2.10.

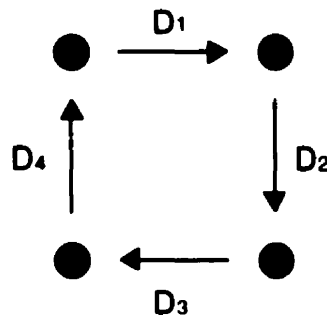


Fig. 2.10 Inconsistency Flagging

The phase is checked along the closed path indicated. If the sum of the wrapped-phase differences along the path, $D_1 + D_2 + D_3 + D_4$, equals zero, then all four points are said to be consistent; otherwise, all four points are flagged as inconsistent. This is done for all 2×2 regions until the entire phase map is covered. This processing detects pixels of phase discontinuity and masks them out. After flagging, bad segments have been cut from each scan line. The next step is to set up a phase unwrapping path required to circumnavigate the bad segments along a scan line.

strategy to consider large-scale regional inconsistencies. For more details about this algorithm, please see the reference papers by Goldstein, Zebker & Werner (1988) and Huntley (1989).

(3) Flood phase unwrapping algorithm

Bone (1991) proposed a new phase unwrapping algorithm to overcome some limitations of the noise-immune cut approach, for example, when the network of segment cuts is not uniquely determined. Rather than construct segment cuts, Bone's method constructs a mask to prevent the unwrapping process from following any path that could lead to inconsistencies. A concept of the second difference of the wrapped phase map is introduced, as defined below. The second differences are calculated from the locally unwrapped phase, as shown in Fig. 2.12

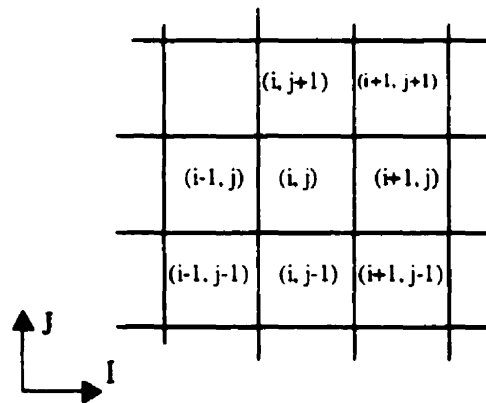


Fig.2.12 Second Differences Calculation

For a given pixel (i, j) , the second differences are

$$\begin{aligned}\Delta_{yy}(i, j) &= \Delta_x(i, j+1) - \Delta_x(i, j) \\ \Delta_{xx}(i, j) &= \Delta_x(i+1, j) - \Delta_x(i-1, j) \\ \Delta_{yy}(i, j) &= \Delta_x(i, j+1) - \Delta_x(i, j-1)\end{aligned}$$

where

$$\Delta_x(i, j) = \Phi(i+1, j) - \Phi(i, j)$$

These second differences are calculated for all the pixels in the wrapped phase map. There is discontinuity if one of the three second-differences is greater than a threshold value, but smaller than 2π radians. For all discontinuity points, the mask is set to zero to exclude them from the unwrapping process.

When the mask operation is completed, the phase unwrapping can be carried out by using a recursive flood fill algorithm. The phase is unwrapped at a point only if at least one of its eight neighbors is unwrapped. For that, 2π is added or subtracted while the phase difference between the point and its adjacent point is greater than 2π . When a point is unwrapped, the mask for this point is set. The wrapped phase map is scanned to make sure every consistent point has been unwrapped.

2.4.2 Region-based Unwrapping Algorithm

The above unwrapping algorithms are typically written to make a phase unwrapping decision on each point as an individual unit, using knowledge about only the one preceding point or the adjacent points. They make a large number of immediate decisions based on limited data. The concept of region-based unwrapping is to make a small number of decisions based on a much larger amount of analysis.

The region-based unwrapping algorithm groups phase data into regions containing no phase ambiguities. Regions are decided by determining whether points lie within a tolerance of adjacent points that are already included in a region. A point will be considered part of the region if a given percentage of the adjacent points belonging to the region are within a specified tolerance of the point. A point may have up to eight neighbors. Typical values for percentage agreement have been from 40 to 65% and typical tolerances from 0.5 to 1.5 radians. Once all points have been assigned to a region, as shown in Fig. 2.13, the edges of the regions are compared to determine if there is a discontinuity between them.

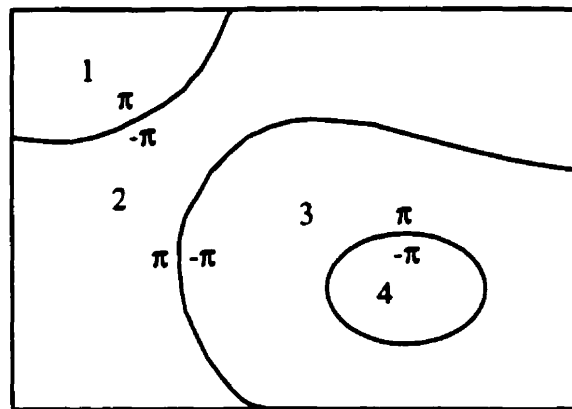


Fig. 2.13 Example of phase map divided into regions

All edges between adjacent regions are traced to determine whether a phase shift should be made, up by 2π , down by 2π or whether no shift is required. Each edge point carries a vote. Once the relationships between regions have been defined, regions that have been identified as having no phase ambiguities are combined into a single larger region. These larger regions are then compared to determine the necessary phase shifts that need to take place. This algorithm recognizes the problem posed by large-scale discontinuities, and is employed in this work. For more details, please see Gierloff's paper (1987). Finally, Fig. 2.14 and Fig. 2.15 show some phase unwrapping examples experienced in this work.

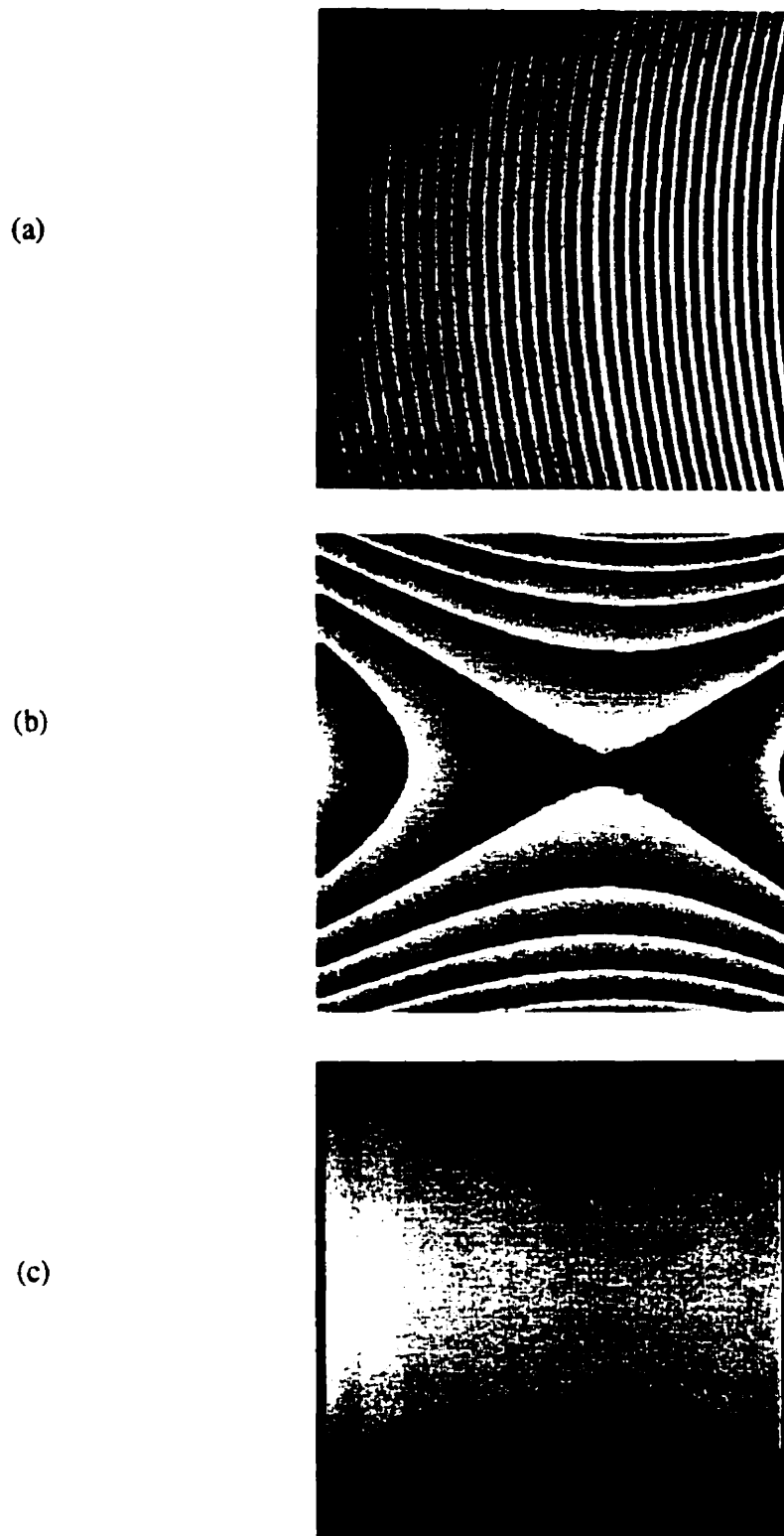


Fig. 2.14 Phase unwrapping example—cylindrical surface: (a) original deformed grating image (grating lines are parallel with the axis of the cylinder); (b) wrapped phase image; (c) unwrapped phase image.

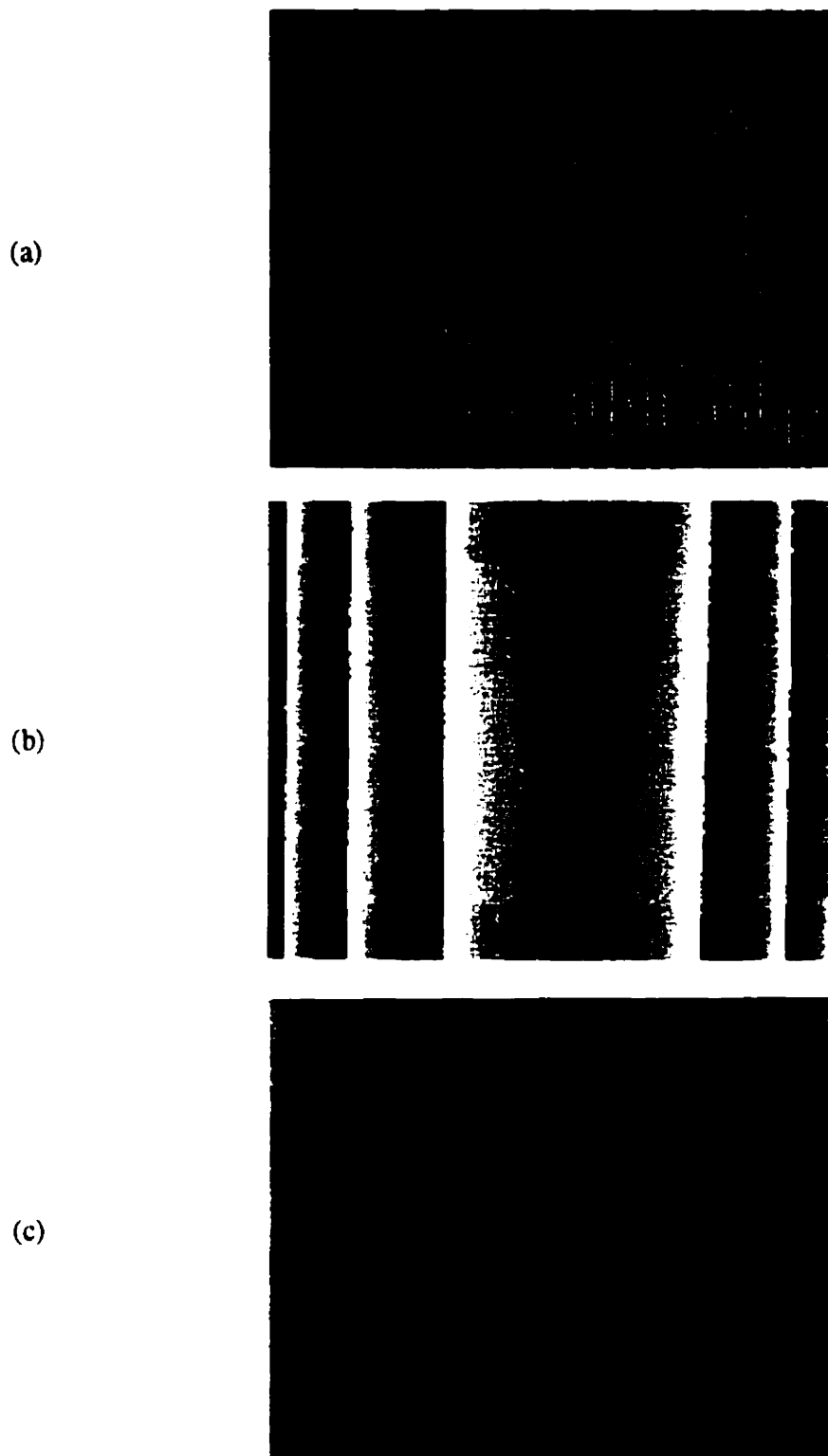


Fig. 2.15 Phase unwrapping example—cylindrical surface: (a) original deformed grating image (grating lines are perpendicular with the axis of cylinder); (b) wrapped phase image; (c) unwrapped phase image.

2.5 Summary

In Section 2.2, different techniques are introduced to extract the phase information from a deformed grating image. It is required that the phase calculation process should be carried out automatically without any ambiguity, unlike the concave and convex problem in the classic geometric Moiré methods. In addition, the applicability to high-speed measurement is also a concern. The phase-shifting technique is not suitable in this research since it needs at least three frames to compute the phase information, which is inclusively for static surface measurements. Therefore, the Fourier transform technique is chosen for this research. Section 2.3 gives a detailed description of the Fourier transform method. Finally, the phase unwrapping algorithms are outlined in Section 2.4. Fig. 2.16 summarizes the basic steps involved in calculating the phase information. Table 2.2 summarizes the features of different optical profile measurement techniques. Considering whole-field, high-speed 3D surface measurement, there are only two candidates. Following the steps described in this chapter, a continuous phase map can be obtained from a deformed grating image. The next chapter will describe how to obtain absolute Cartesian coordinates from the continuous phase map.

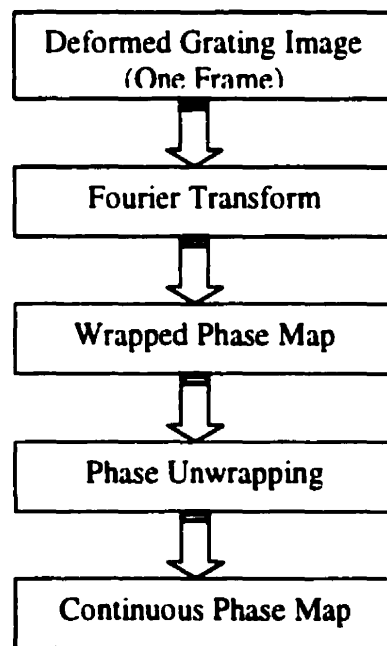


Fig. 2.16 Processing summary of the grating projection and Fourier method.

		Moiré Fringes	Data Processing	Measurement Results	Frame(s) Needed	Whole Field Meas.	Applicable to High-speed Measuring
Geometric Moiré	Shadow Moiré	Yes	Human intervention	(h, i, j) on the center of Moiré fringes	One	Yes	Yes
	Projection Moiré	Yes	Human Intervention	(h, i, j) on the center of Moiré fringes	One	Yes	Yes
Grating Projection Methods	FFT	No	Automatic	(h, i, j) for all pixels	One	Yes	Yes
	Phase Shifting	No	Automatic	(h, i, j) for all pixels	≥ 3	Yes	No
	Others	No	Automatic	(h, i, j) for all pixels	One	Yes	Yes
Laser Scanning Techniques		No	Automatic	(x, y, z) on the center of scan lines	Multi frames	No	No

Table 2.2 Features of different optical profile measurement methods.

CHAPTER 3

SYSTEM CALIBRATION

3.1 Introduction

In this research, the objective is to digitize surfaces, which are involved in a dynamic event such that their shapes and spatial positions are changing as a function of time. In such a case, multiple measurements from the same direction are required in order to build a complete time history of the deformation. In order to build a time history of deformation in a dynamic event, the xyz coordinates of each individual measurement, taken at different times, are needed to be with respect to an absolute global coordinate system within the accuracy of the measurement system. That is what is desired for the measurement results. Let us keep this requirement in mind and see what the results are from the processing described in the previous chapter.

The grating projection method has been introduced in Chapter 2. A deformed grating image after being processed by the Fourier transform can provide a continuous phase map, which is related to the surface height with respect to a reference plane. However, this technique has previously been limited to relative measurements. This is because most of the measurement procedures presented so far allow the evaluation of the height $H_{p(i, j)}$ with respect to a reference plane. Moreover, the coordinates (i, j) of a point p are expressed with reference to the column and row indices of the corresponding image point on the image plane. This kind of surface shape information is useful to describe a surface qualitatively, such as how many concavities and convexities exist and how big the maximum displacement in the Z direction the surface has. However, as mentioned in the beginning, three-dimensional Cartesian coordinates are needed to define 3D shapes quantitatively. Therefore, to this point the measurement results, $H_{p(i, j)}$, are indirect, and can not fulfill the ultimate goal—the determination of 3D Cartesian coordinates with respect to a fixed coordinate system.

Some researchers have tried to solve this problem by transforming the column and row indices (i, j) of an image point to (x, y) coordinates by using a constant scale ratio (magnification ratio) while ignoring lens aberrations and distortions. By doing this, errors are introduced to the final results because the scale ratio is not uniform throughout the depth of view, and it is changing at least as a function of the z coordinate (see Section 3.2 for details). This spatial dependency of the scale ratio can't be neglected when a surface is not flat. In addition, even a high quality lens has some aberrations, which means in practice that the scale ratio should be a non-linear function of (i, j, z) . Obviously, for the calculation of $x, y,$ and z coordinates, a mathematical model must be assumed that describes the relationship between the measured values, such as phase and image coordinates, and the ultimate 3D coordinates.

In this chapter, a calibration procedure is proposed that can create a relationship between the indirect measured values and the ultimate 3D coordinates. This mathematical model allows the indirect measured values to be converted into 3D Cartesian coordinates. Before introducing the details of calibration, let us outline some basics of imaging geometry.

3.2 Imaging Geometry

Fig. 3.1 shows a model of the optical image formation process. All geometry is expressed in a 3D Cartesian coordinate system (X, Y, Z) , called *the global coordinate system*, in which the position of a point is defined by 3 coordinates denoted (x, y, z) . The 2D image, given by (i, j) is used to denote the position of a pixel in an image plan. Let us assume that the image plane is parallel to the XY plane, and the optical axis is along the Z -axis. The point O_2 and O_3 are the centers of the image plane and the lens, respectively. As shown in Fig. 1.6, the image plane is physically associated with the CCD camera. Any change in the orientation and position of the CCD camera will result in a change of the orientation and position of the image plane with respect to the global coordinate system. If the camera is in focus for distant objects, the distance between O_2 and O_3 is the *focal length* of the lens denoted as λ .

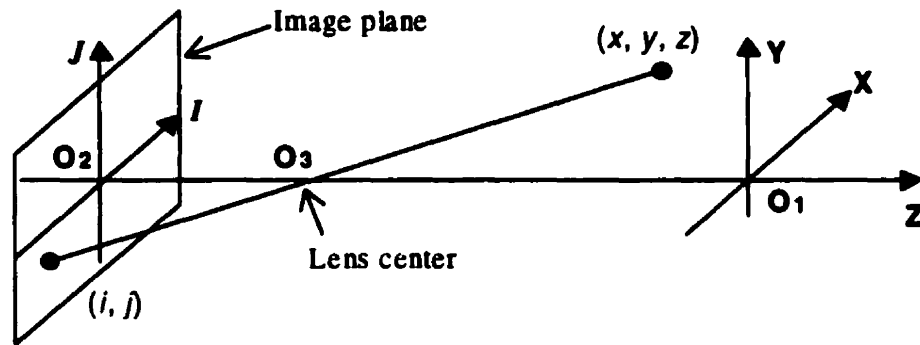


Fig. 3.1 Basic geometry model of image forming.

As shown in Fig. 3.1, let (x, y, z) be the global coordinates of any point in a 3D scene, and we assume that all points of interest lie in front of the lens. The relationship that gives the image coordinates (i, j) of the projection of the point (x, y, z) onto the image plane is easily accomplished by the use of similar triangles. With reference to Fig. 3.1, if the Cartesian coordinate system is shifted to the location of the image coordinate system (O_1 and O_2 is the same point), we have

$$\frac{i}{\lambda} = -\frac{x}{z - \lambda} \quad (3.2-1)$$

$$\frac{j}{\lambda} = -\frac{y}{z - \lambda} \quad (3.2-2)$$

Where the negative signs in the equations indicate that image points are actually inverted, as the geometry of Fig. 3.1 shows. The image-plane coordinates of the projected 3D point follow directly from Eqs. 3.2-1 and 3.2-2:

$$x = \frac{\lambda - z}{\lambda} \times i \quad \text{or} \quad x = f(i, z) \quad (3.2-3)$$

$$y = \frac{\lambda - z}{\lambda} \times j \quad \text{or} \quad y = g(j, z) \quad (3.2-4)$$

Equations 3.2-3 and 3.2-4 show that unless something (for example its z coordinate) is known about the 3D point that generated an image point, it is not possible to completely recover the global x and y coordinates of a 3D point from its image coordinates (i, j) . Therefore, the global coordinate x and y are functions of (i, z) and (j, z) , respectively. As addressed in Section 3.1, some researchers have assumed a constant scale ratio to derive x and y coordinates from its corresponding image coordinates (i, j) . This operation, however, requires some care. Only in the case of flat surfaces, can it safely be assumed that the transform between the global coordinates (x, y) and the image or pixel coordinates (i, j) does not depend on the small surface shape variation $z(x, y)$. For non-flat-surfaces, neglecting the surface height variation can create errors. The calculation of (x, y, z) has to be carried out together since they depend on each other.

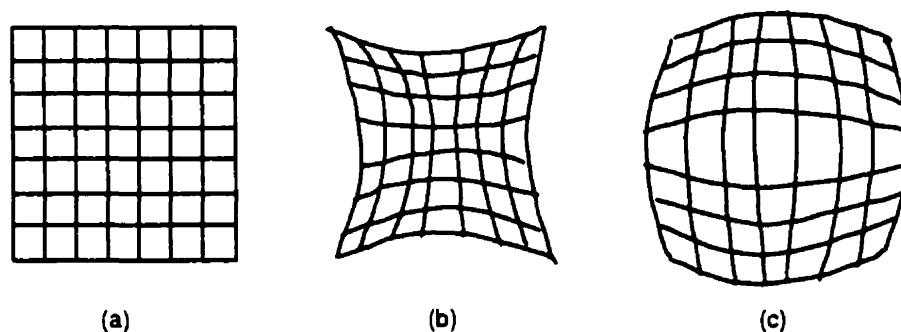


Fig. 3.2 Examples of lens distortion: (a) Original Grid, (b) Pincushion Distortion, (c) Barrel Distortion;

In optical 3D measurement systems, lenses or lens systems (consisting of several thin lenses) play an important role in grating projection and image forming. Two lens systems are used in our system, one is the projection lens system and another is the camera lens system. As shown in Fig. 3.2, one of the basic problems of lenses and lens systems is the imperfect quality of the images, usually called *the lens aberrations*. Such imperfect images are largely the result of defects in the shape and form of the lenses. The

lens aberrations are very detrimental to optical measurement systems since the measurement values (such as 3D coordinates in our case) are calculated on the basis of precise analysis of image forming. We always assume simply theory of lens systems in optical 3D measurement systems, which ignores the distortion of the lenses. Clearly, this is not the case in practice. For example, there is no single focal length for a lens due to the spherical aberrations. Therefore, we have to assume that there are some distortions in every image, and due to these distortions the magnification of off-optical-axis points differs from the magnification of those points near the lens optical axis. With lens distortions in mind, Eqs. 3.2-3 and 3.2-4 will be rewritten in a more general form.

$$x = F(i, j, z) \quad (3.2-5)$$

$$y = G(i, j, z) \quad (3.2-6)$$

The x and y coordinates are functions of i , j and z coordinates. In addition, different lenses have unique transformation functions. Therefore, in practice we have to find out the form and all the coefficients of these two equations for each lens. A procedure for determining the model parameters from a set of points with known global Cartesian coordinates and their corresponding image coordinates is called “the camera calibration.” Once the calibration is done, the 3D information can be inferred from corresponding 2D image information and vice versa. This is the purpose of the next section.

3.3 Calibration Techniques

Equations 3.2-5 and 3.2-6 are the general form of the relationship between 2D and 3D world. In this section, we will further formulate these two equations, and moreover to determine the form of the functions involved. The image acquisition, which is used to capture the deformed grating patterns in all the image processing techniques described in Chapter 2, results in a series of transformations before a grating image is finally stored in a computer’s memory as a 2D digital image. These transformations must be inverted before the results processed from the 2D digital image can be related to the information used in 3D space. As described in Section 3.2, the information processed from a

deformed grating image (a 2D image) is (i, j, h) , and the results we need in 3D space are xyz coordinates. The most common types of transformations from the 3D world coordinates to 2D image plane coordinates are coordinate translation and rotation, lens distortion and perspective transformation. In the following section, a camera model will be developed for the transformation from 3D global coordinates to camera coordinates.

3.3.1 The Camera Model

Consider a pinhole camera model with lens distortion, as shown in Fig. 3.3. Let P be an object point in the 3D space, and (x_g, y_g, z_g) be its coordinates with respect to a fixed global coordinate system (GCS). Let the camera coordinate system (CCS) have its XY plane parallel to the image plane, such that the X -axis is parallel with the horizontal direction of the image, and the Y -axis is parallel with the vertical one. The origin of CCS is located at the lens center and the Z -axis is aligned with the optical axis of the lens, which is perpendicular to the image plane.

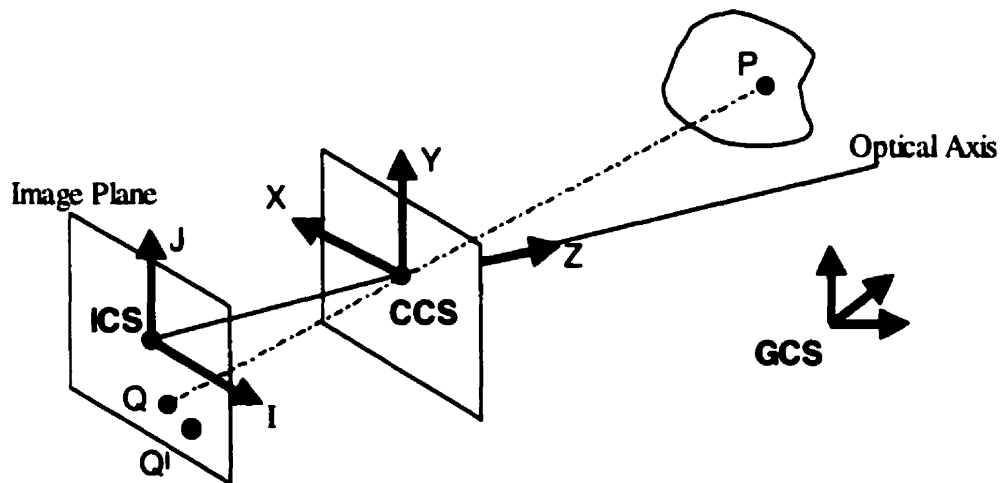


Fig.3.3 Pinhole camera model with lens distortion

Let (x_c, y_c, z_c) be the coordinates of the 3D point P with respect to the CCS. If there is no lens distortion, the corresponding image point of P on the image plane would be Q (see Fig. 3.3). However, due to the effect of lens distortion, the actual image point is Q' . Let (i, j) denote the 2D image coordinates (in pixels) of the actual image point Q' with respect

to the computer image coordinate system (ICS). The origin of the ICS is the intersection point of the image plane and the optical axis. The distance between the image plane and the lens center is denoted as f . The overall transformation from (x_g, y_g, z_g) to (i, j) can be divided into the following four steps, as shown in the flow chart of Fig. 3.5.

(1) Translation and rotation from the GCS to CCS

The transformation from the global coordinate system to the camera coordinate system can be expressed as:

$$\begin{bmatrix} x_c \\ y_c \\ z_c \\ 1 \end{bmatrix} = \begin{bmatrix} r_1 & r_2 & r_3 & t_1 \\ r_4 & r_5 & r_6 & t_2 \\ r_7 & r_8 & r_9 & t_3 \\ 0 & 0 & 0 & 1 \end{bmatrix} \begin{bmatrix} x_g \\ y_g \\ z_g \\ 1 \end{bmatrix} \quad (3.3-1)$$

This equation can be also written in the following matrix form.

$$\vec{r}_c = T_c^g \vec{r}_g = \begin{bmatrix} R_c^g & t_c^g \\ 0 & 1 \end{bmatrix} \cdot \vec{r}_g \quad (3.3-2)$$

Here, $t_c^g = (t_1, t_2, t_3)^t$ is a translation vector, and R_c^g is a 3×3 rotation matrix determined by the three Euler angles, ϕ , θ , and φ , rotating about the X , Y , and Z axes sequentially, as shown in Fig. 3.4.

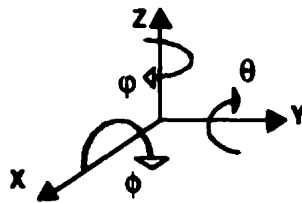


Fig. 3.4 Definition of Euler angles.

(2) Perspective projection from a 3D object point in the CCS to a 2D image point on the image plane

As shown in Fig. 3.3, the distance between CCS and ICS planes is f , also referred to as the *effective focal length*. Let (i_u, j_u) be the 2D image coordinates of the undistorted image point Q lying on the image plane. Then, we have

$$i_u = f \cdot \frac{x_c}{z_c} \quad \text{and} \quad j_u = f \cdot \frac{y_c}{z_c} \quad (3.3-3)$$

Since the origin of the CCS is at the lens center, Eq. 3.3-3 has a different form than Eq. 3.2-1 and Eq. 3.2-2.

(3) Radial lens distortion from Q to Q'

Let (i_d, j_d) be the 2D image coordinates of the distorted image point Q'. Then we have

$$i_u = i_d \cdot (1 + k \cdot r^2) \quad \text{and} \quad j_u = j_d \cdot (1 + k \cdot r^2) \quad (3.3-4)$$

Here, $r^2 = i_d \times i_d + j_d \times j_d$. Based on the experience of some researchers, Eq. 3.3-4 is adequate enough to model lens distortion for industrial vision applications (Tsai 1987). More elaborate modeling not only would not help but also would cause numerical instability.

(4) Scaling of 2D image coordinates

The horizontal and vertical pixel spacing, δ_u and δ_v (millimeter/pixel), are used to scale from pixels to millimeters.

Combining these four steps together, we have

$$(1-k \cdot r^2) \cdot i \cdot \delta_u = f \cdot \frac{x_g r_1 + y_g r_2 + z_g r_3 + t_1}{x_g r_7 + y_g r_8 + z_g r_9 + t_3} \quad (3.3-5)$$

$$(1-k \cdot r^2) \cdot j \cdot \delta_v = f \cdot \frac{x_g r_4 + y_g r_5 + z_g r_6 + t_2}{x_g r_7 + y_g r_8 + z_g r_9 + t_3}$$

Instead of (i_d, j_d) , we use (i, j) as the true or distorted image coordinates. The parameters used in the transformation from the 3D world to the 2D image plane can be categorized into the following two classes.

- **Extrinsic Parameters:** the parameters used for the rigid body transformation from the 3D global coordinate system (GCS) to the 3D camera coordinate system (CCS) with the origin at the lens center are called the extrinsic parameters. There are six extrinsic parameters: the Euler angles pitch ϕ , yaw θ , and tilt φ for rotation and the three components for the translation vector t^c . The rotation matrix R^c can be expressed as a function of ϕ , θ , and φ . These Euler angles are defined in Fig. 3.4.

$$R_c^s = \begin{bmatrix} \cos \varphi \cos \theta & \sin \varphi \cos \theta & -\sin \theta \\ -\sin \varphi \cos \phi + \cos \varphi \sin \theta \sin \phi & \cos \varphi \cos \phi + \sin \varphi \sin \theta \sin \phi & \cos \theta \sin \phi \\ \sin \varphi \sin \phi + \cos \varphi \sin \theta \sin \phi & -\cos \varphi \sin \phi + \sin \varphi \sin \theta \sin \phi & \cos \theta \cos \phi \end{bmatrix} \quad (3.3-6)$$

- **Intrinsic Parameters:** the parameters used for the transformation from 3D coordinates in the CCS to the image coordinate system (ICS) are called the intrinsic parameters. There are usually five parameters: effective focal length f , lens distortion coefficient k , pixel scaling factors δ_u & δ_v , and the origin coordinates of the computer image coordinate in the image plane (i_0, j_0) . Since we have the origin of the computer image the same as the intersection point of the optical axis and the image plane, $(i_0, j_0) = (0, 0)$. For a solid state camera (CCD or CID cameras), the pixel spacing factors are known. Therefore, the parameters that need to be calibrated are f and k .

To summarize these transformations, we create a flow chart as shown in Fig. 3.5. All the parameters used at different steps, which need to be calibrated later, are listed.

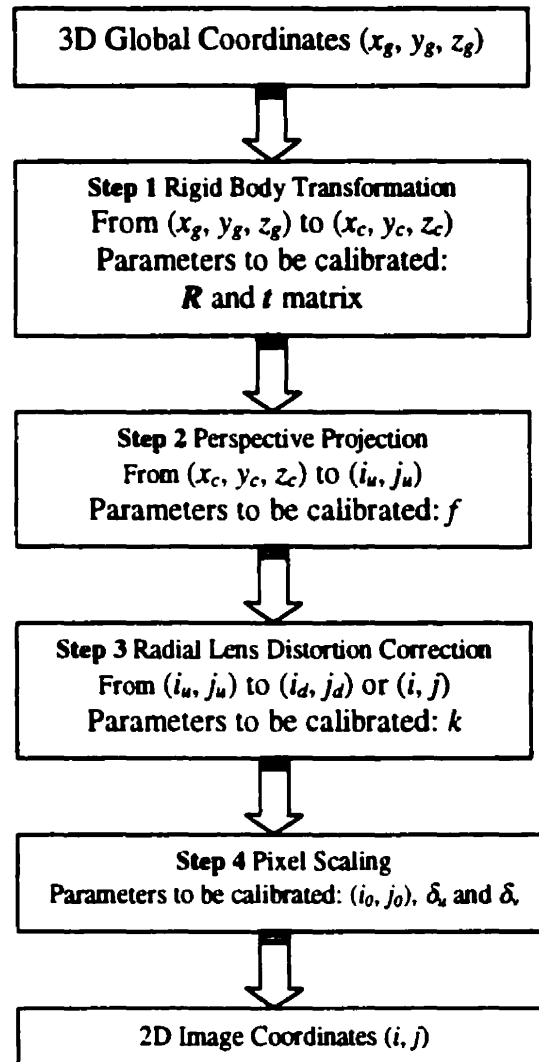


Fig. 3.5 Transformation from 3D global coordinate to 2D image coordinate.

3.3.2 Phase-to-Z Conversion

In this section, a formula for converting the measured phase distribution into z coordinates will be derived. In Section 2.2, it has been shown that the phase is correlated with the surface height for parallel incident light rays. Now we will set up this relationship for an ordinary point lighting source.

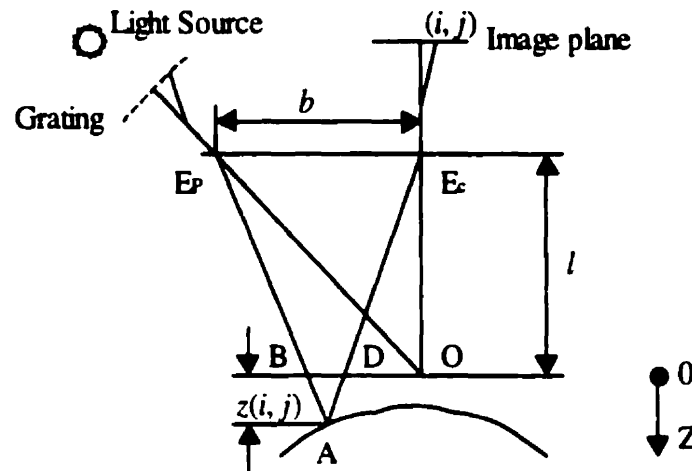


Fig 3.6 Crossed-optical-axes geometry

As shown in Fig. 3.6, a grating pattern is projected onto the surface to be measured by a point lighting source. The optical axis of the projector crosses the optical axis of the camera at point O on a $z=0$ plane, which has been set up during the calibration. E_p and E_c denote, respectively, the front centers of the lenses for the projector and the camera. The distance between these two lens centers is b , and the distance between the lens center to the $z=0$ plane is denoted as l . A light ray passes through the $z=0$ plane at point B and reaches the surface at point A . Then the reflected ray passes through the $z=0$ plane again at point D . Eventually, an image point is formed on the image plane at (i, j) . Note the triangle ABD is similar to the triangle AE_cE_p . Therefore, we can write

$$\frac{\overline{BD}}{z(i, j)} = \frac{b}{l + z(i, j)} \quad (3.3-7)$$

Let f_0 be the frequency of the deformed grating on the $z=0$ plane. We then have

$$\Phi(i, j) = 2\pi f_0 \overline{BD} \quad (3.3-8)$$

Substituting Eq. 3.3-8 into Eq. 3.3-7 and solving for $z(i, j)$, we obtain the following conversion formula.

$$z(i, j) = \frac{l \cdot \Phi(i, j)}{2\pi f_0 \cdot b - \Phi(i, j)} \quad (3.3-9)$$

By using Eq. 3.3-9, the phase information of each pixel on the image plane can be correlated to the z coordinates if all the parameters in the above equation are known. Actually, f_0 is not uniform over the entire field of view since a point light source is used. The deformation of the grating, including the rotation of the grating lines and slight change of f_0 , becomes the source to calculate the surface shape. What has to be calibrated is f_0 as a function of (i, j) on the $z=0$ plane.

3.3.3 Calibration Procedure

Up to now, the relationship between the direct measured information $\Phi(i, j)$ and the ultimate 3D coordinates (x, y, z) has been accomplished through the following three equations. If all the constants involved in the equations are known, the $\Phi(i, j)$ at any pixel on the image plane can be converted into 3D coordinates (x, y, z) . The problem of camera calibration is to compute the constants involved in these equations. The constants include the camera intrinsic and extrinsic parameters, the grating frequency on the $z=0$ plane, and the distance between the two lens centers. The calibration is carried out based on a number of points whose global coordinates (x, y, z) are known and whose corresponding image coordinates (i, j) and phase Φ are measured. The details of calibration are described in the following paragraphs.

$$\begin{cases} (1 - k \cdot r^2) \cdot i \cdot \delta_u = f \cdot \frac{x_g r_1 + y_g r_2 + z_g r_3 + t_1}{x_g r_7 + y_g r_8 + z_g r_9 + t_3} \\ (1 - k \cdot r^2) \cdot j \cdot \delta_v = f \cdot \frac{x_g r_4 + y_g r_5 + z_g r_6 + t_2}{x_g r_7 + y_g r_8 + z_g r_9 + t_3} \\ z(i, j) = \frac{l \cdot \Phi(i, j)}{2\pi f_0 \cdot b - \Phi(i, j)} \end{cases}$$

(1) Camera Parameter Calibration

Fig. 3.7 illustrates the setup for calibrating a camera using a set of monoview non-coplanar points. The camera is mounted on a translation stage, and an accurate surface of a metal block, called the calibration target, is in front of the camera. Two Ronchi gratings are mounted on the surface with its grating lines perpendicular to each other. The spacing of the grating lines is known, and the central points of the grating lines are treated as the calibration points. The vertical grating is used for the x -calibration and the horizontal grating for the y -calibration.

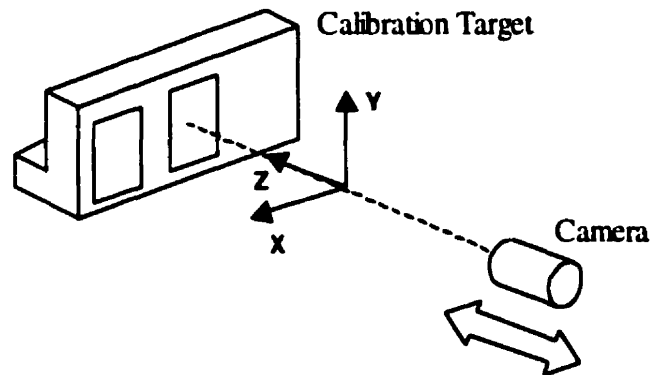


Fig. 3.7 Schematic of the experimental setup for camera calibration.

Several images are taken at different z values, one of which is established as $z=0$. From these images, the phase is calculated, and then the (Φ, i, j) and its corresponding (x, y, z) are known for each selected point. Assuming that we have N pairs of 2D-3D calibration points, Eq. 3.3-5 can be also written in a matrix form (see Appendix A).

$$[A] \cdot [p] + [B] \cdot [q] + k \cdot [C] \cdot [q] = [0] \quad (3.3-10)$$

where

$$[A] = \begin{bmatrix} \cdot & \cdot \\ x & y & z & 1 & 0 & 0 & 0 & 0 \\ 0 & 0 & 0 & 0 & x & y & z & 1 \\ \cdot & \cdot \end{bmatrix}_{2N \times 8}$$

$$[B] = \begin{bmatrix} \cdot & \cdot & \cdot & \cdot \\ -i \cdot x & -i \cdot y & -i \cdot z & -i \\ -j \cdot x & -j \cdot y & -j \cdot z & -j \\ \cdot & \cdot & \cdot & \cdot \end{bmatrix}_{2N \times 4}$$

$$[C] = \begin{bmatrix} \cdot & \cdot & \cdot & \cdot \\ i \cdot r^2 \cdot x & i \cdot r^2 \cdot y & i \cdot r^2 \cdot z & i \cdot r^2 \\ j \cdot r^2 \cdot x & j \cdot r^2 \cdot y & j \cdot r^2 \cdot z & j \cdot r^2 \\ \cdot & \cdot & \cdot & \cdot \end{bmatrix}_{2N \times 4}$$

$$[P_1] = \begin{bmatrix} r_1 f / \delta_u \\ r_2 f / \delta_u \\ r_3 f / \delta_u \\ t_1 f / \delta_u \end{bmatrix}, \quad [P_2] = \begin{bmatrix} r_4 f / \delta_v \\ r_5 f / \delta_v \\ r_6 f / \delta_v \\ t_2 f / \delta_v \end{bmatrix}, \quad [P_3] = \begin{bmatrix} r_7 \\ r_8 \\ r_9 \\ t_3 \end{bmatrix}$$

$$[p] = \begin{bmatrix} [P_1] \\ [P_2] \end{bmatrix} \cdot \frac{1}{t_3}, \quad [q] = [P_3] \cdot \frac{1}{t_3}$$

Substituting N pairs of 2D-3D point coordinates into Eq. 3.3-10, the composite parameters defined in $[p]$ and $[q]$ can be solved for by using the pseudo-inverse method. Then the composite parameters can be further decomposed into individual parameters.

(2) Sensor Head Geometry Calibration

Very similar to the camera parameter calibration, a monoview non-coplanar calibration method is used for the sensor head geometry calibration. If we use N pairs of known 2D-3D points, Eq. 3.3-9 can be re-written in a matrix form.

$$[D] \cdot [h] = [E] \quad (3.3-11)$$

where

$$[D] = \begin{bmatrix} z(i, j) & -\Phi(i, j) \\ \cdot & \cdot \\ \cdot & \cdot \\ \cdot & \cdot \end{bmatrix}_{N \times 2} \quad [h] = \begin{bmatrix} 2\pi f_0 \cdot d \\ l \end{bmatrix}_{2 \times 1} \quad [E] = \begin{bmatrix} z(i, j) \cdot \Phi(i, j) \\ \cdot \\ \cdot \\ \cdot \end{bmatrix}_{N \times 1}$$

Substituting N pairs of 2D-3D point coordinates into Eq. (3.3-11), the composite parameters defined in $[h]$ can be solved by using the pseudo-inverse method.

3.4 Summary

As mentioned in the beginning of this chapter, the goal of optical 3D measurement is the determination of the Cartesian coordinates of surfaces. All known optical methods based on grating projection are creating relative and indirect results, such as the height information. Based on the works of photogrammetry, a camera calibration technique has been developed for the grating projection method to calculate Cartesian coordinates from the directly measured values (phase and image coordinates). The calibration is carried out before the measurement in order to obtain all the constants involved in the system, including the parameters of the camera (intrinsic and extrinsic) and the relative geometry between the camera and the projector. After the calibration is carried out in the lab, the whole optical measurement system can be taken to any site to perform in-situ measurements. As long as the camera and the geometry between the camera and the projector remain unchanged, there is no need to re-calibrate. In each measurement, the direct calculated results (i, j, Φ) can then be converted into 3D coordinates (x, y, z) by using the mathematical model previously described.

To have 3D Cartesian coordinates as the measurement results is very important for the dynamic measurement. It provides a very detailed 3D raw information source—a set of point clouds in 3D space. From the point clouds, it is possible to analyze the information further, such as the curvature, cross-sectional lines, and even to reconstruct the surface. In addition, due to the large amount of points obtained, any detailed feature at any location inside the field of view can be analyzed. Furthermore, it provides a practical tool for verifying the measurement accuracy, which will be the topic of Chapter 5. The following chapter will describe the dynamic measurement system from the point of view of hardware.

CHAPTER 4

DYNAMIC MEASUREMENT SYSTEM

4.1 Introduction

In previous chapters, the details of the grating projection and Fourier transform technique are presented. In addition, the data processing algorithms are depicted systematically. These are the theoretical basis of the optical measurement system proposed for this research. In this chapter, the emphasis will be shifted to the hardware's point of view. In the first section, a system overview will be given, which covers the main components of the optical measurement system. As the most important components, the high-speed camera SR-1000 and the multi-channel data link (MCDL) will be introduced in the last two sections.

4.2 System Overview

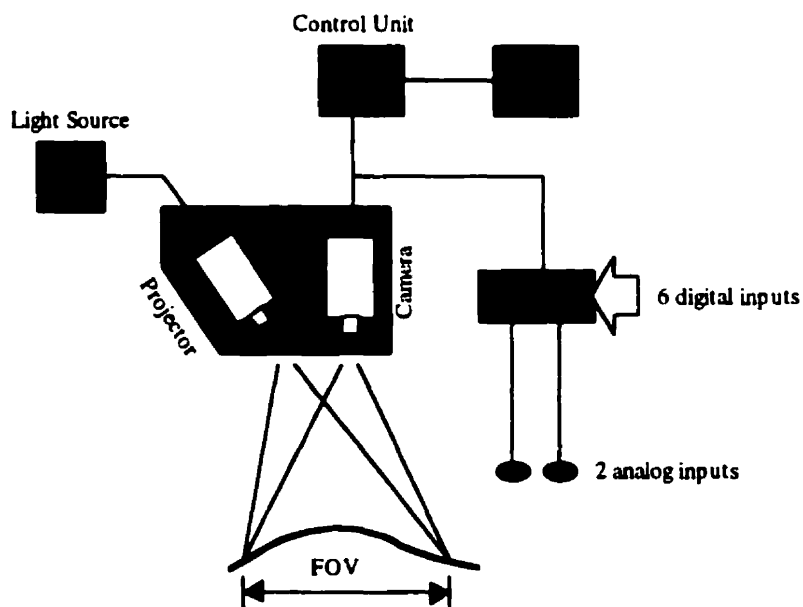


Fig. 4.1 Schematic of the high-speed optical measurement system.

As shown in Fig. 4.1, the proposed optical measurement system consists of a high-speed digital camera and its control unit, a light source, a grating projector, a multi-channel data link (MCDL), and a personal computer. Actually, the high-speed camera and the grating projector are mounted inside a box, which is called the sensor head. The light source illuminates a Ronchi grating inside the projector, and the grating is projected onto the surface to be measured by a 16-mm lens. Ronchi gratings are evenly spaced lines running parallel to each other. After being projected onto a surface, its image will deform according to the surface shape. The deformed grating images on the specimen surface are digitized and saved into the control unit of the high-speed camera system at a certain framing rate. In the mean time, the MCDL acquires external analog and digital signals simultaneously to correlate them with each frame. The images stored in the memory of the camera control unit are replayed to view the recording to select interesting frames to represent a dynamic event. The selected image frames are then transferred into the computer and saved as standard image files via a SCSI-II connection. After each deformed grating image being processed by the computer, an array of points (as many as 200,000 points) with known xyz coordinates is generated, which represents the surface shape inside the field of view of the camera. Since a high-speed camera is used, a sequence of deformed grating images of a dynamic event is saved successively at a certain frame rate. By processing each individual image, it is possible to obtain the surface shape at that particular time when this frame is recorded. By processing these deformed grating images, the surface deformation history is known as a function of time since the time interval between image frames is known. In conclusion, the system has the ability to digitize the whole surface inside the field of view into an array of points with known xyz coordinates, at a certain sampling rate (30 ~ 1000 Hz).

For the current system configuration, the field of view is approximately 100×100 mm, and the depth of view (outside this range the grating image will be blurred) is approximately 50 mm. The distance from the sensor head to the surface to be measured, called the working distance, is approximately 200 ~ 250 mm. The dimension of the sensor head is approximately $335(L) \times 200(W) \times 80(H)$ mm. The image acquisition time

is dependent on the electronic shutter speed (as low as 50 μsec) and the framing rate of the camera (30 ~ 1000 fps). The time needed to process one image frame saved on the hard drive is approximately 15 seconds for the current computer (Pentium 200 MHz). Since the final measurement results are *xyz* coordinates, we set up a goal for the measurement accuracy—less than $\pm 50 \mu\text{m}$ for the overall measurement. This is the precision for *xyz* coordinates calculation, and details of the accuracy will be described in the next chapter. By changing the lens specifications and the geometry of the sensor head, the field of view and the working distance can be modified to fit a particular application.

Until now, the general information regarding the proposed optical measurement system has been introduced in this section. As the most important component, the details of the high-speed camera will be described in the following section.

4.3 High-speed Camera Specifications

As the recording device in the proposed system, a high-speed monochrome digital camera is used in this work—Kodak Motion Corder SR-1000 (Motion Analysis Systems Division, Eastman Kodak Company). A picture of the high-speed camera is shown in Fig. 4.2. The specifications of the high-speed camera are listed in Table 4.1.

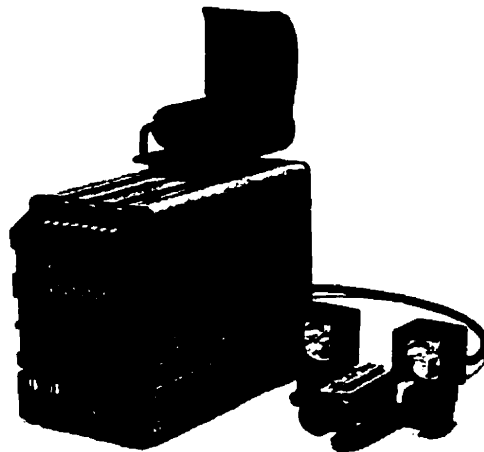


Fig. 4.2 Kodak Motion Corder High-speed Camera SR-1000.

Imager	CCD, 7.4×7.4 μm pixel size, progressive scanning, 658×496 sensor array
Electronic Shutter	As fast as 50 μsec. depending on the frame rate
Display Resolution	256 gray levels, RS-170 video output
Recording Rate	30, 60, 125, 250, 500, and 1000 frames per second (fps)
Trigger Modes	start, center, end and random (activation: control panel & TTL external input)
Frame Storage	DRAM memory for 546 frames @ 512×480 resolution.
Recording Time (sec)	18.2 @ 30 fps (546 frames @ 512×480 resolution) 9.1 @ 60 fps (546 frames @ 512×480 resolution) 4.4 @ 125 fps (546 frames @ 512×480 resolution) 2.2 @ 250 fps (546 frames @ 512×480 resolution) 2.2 @ 500 fps (1092 frames @ 512×240 resolution) 2.2 @ 1000 fps (2184 frames @ 256×240 resolution)
Digital Image Output	8 bit monochrome TIFF or BMP file export via SCSI-2 connected PC.
External Data Input	Accepts 2 analog and 6 digital data inputs via Kodak MCDL
Lens Mounting	Standard C-mount

Table 4.1 Specifications of the Kodak SR-1000 High-speed camera.

The deformed grating images, which are changing their forms quickly during a dynamic event, are captured by the high-speed camera and stored temporarily in the camera's DRAM memory. Four triggering modes (start, center, end and random) can be selected to fit a particular application. In addition, the triggering signal can be a TTL compatible signal (BNC type connection) or a signal generated by a switch closure. In addition, there is a TTL compatible synchronizing signal provided at the beginning of each image frame for synchronizing other external electronic devices. After images are stored temporarily in the memory of the camera, they can be played back to select useful frames for transfer to a personal computer to store on a hard disk as permanent image files. There is no film or magnetic tape nor moving mechanical parts involved in the whole recording process. This is a major advantage of digital cameras over conventional high-

speed film cameras since all the problems associated with film developing are eliminated. However, the digital high-speed cameras are operating at relatively low frame rates (250 – 1000 fps) compared to the high-speed film cameras (up to 100,000 fps). Some digital high-speed cameras can achieve higher frame rate, but this is accomplished on the reduction of the image size. However, it is expected that the performance of digital high-speed cameras will be enhanced in the near future.

The *xyz* coordinate calculation requires a high-quality grating image. For recording a static object, a lower framing rate and longer exposure time can be used. Therefore, lighting is not a problem for static or relative slow-moving objects. However, lighting is a well-known problem in high-speed photography applications. Extra care has to be taken to make sure the grating images are not blurred and have adequate contrast. In order to avoid noise caused by irregular reflection on the surface, a very thin coating is made on the object to create a matte reflective surface. However, the matte reflective surface of the specimen allows for only a fraction of the incident light beam to be collected by the camera lens. This, along with the need to record a rapidly propagating phenomenon at an exposure time on the order of milliseconds (SR-1000), requires a very intense light source which is not readily available. To meet this condition, a fiber optic illuminator with a 175-Watt quartz halogen lamp is used, which is capable of generating 3200 K light intensity. In addition, two plano-convex lenses are mounted in front of the light-pipe to condense the light rays before they reach the projection grating. Even with all these measures, the light intensity barely reaches the minimum requirement at the framing rate of 1000 fps. For lower frame rates, such as 250 fps, the current lighting is sufficient to provide an adequate illumination.

4.4 Multi-channel Data Link

As shown in Fig. 4.3, the Kodak Multi-channel Data Link (MCDL) expands the capability of the Kodak Motion Corder High-speed Cameras by correlating external signals with each video image. The MCDL can measure two analog voltage levels of

transducers, such as pressure and force sensors, and simultaneously record this data along with the video image. In addition, the MCDL has six digital channels (switch closure). These digital signals can be used to monitor the status of various switches in a complex operation. In our case, the analog pressure and force signals are monitored along with the high-speed images. The MCDL is a very powerful tool that can provide information on the history of force or pressure, which is correlated with the surface shape. Therefore, the MCDL is helpful in many practical measurements.

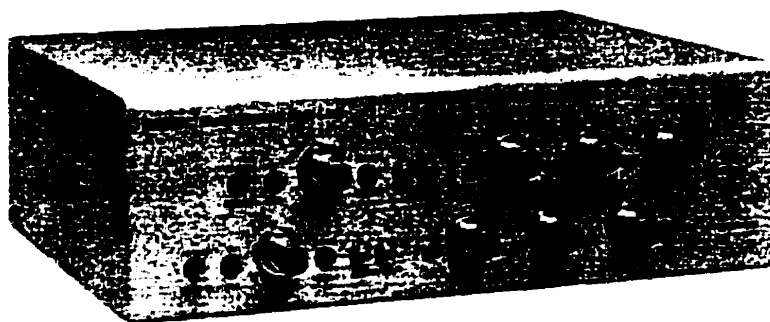


Fig. 4.3 Kodak Multi-channel Data Link (MCDL).

4.5 Summary

In conclusion, the system proposed in this research is an optical measurement system that can digitize a portion of a 3D curved surface into an array of points with known xyz coordinates at a certain sampling rate (30 – 1000 Hz). Since a high-framing-rate digital camera is used, the shape of a surface under dynamic events can be measured as a function of time. In addition, several external signals can be simultaneously recorded with each image frame by using the MCDL. By carrying out further data-analysis on the point sets with known xyz coordinates, the detailed surface information, such as the displacement and curvature, can be obtained. The objective of the accuracy of xyz coordinates calculation is approximately $\pm 50 \mu\text{m}$, and the details on the accuracy issue will be discussed in the next chapter.

CHAPTER 5

ACCURACY AND SENSITIVITY TESTS

5.1 Introduction

In Chapter 3, the fundamentals of the grating projection and Fourier transform technique have been introduced. All processing procedures have been described regarding how to obtain the phase information, which is related to the surface shape. Later, the calibration techniques have been depicted in order to convert the direct measured value (Φ, i, j) into Cartesian coordinates (x, y, z) , which is necessary to define surface shapes in 3D space. So far, with all these steps we can digitize a surface into an array of points with known coordinates. Before we rush into the applications of the proposed system, there is still a question left in our mind, and actually an important question from the users' point of view—how accurately can these 3D measurements be carried out?

Every system used for 3D coordinate measurement has to define its accuracy of measurement. For a coordinate measurement machine, the manufacturers usually use the linear displacement accuracy for three axes and the volumetric performance to specify how accurate their CMMs are. Usually, the accuracy for a CMM is less than $5.0 \mu\text{m}$ per 1000 mm. That means there is an error of approximately $5.0 \mu\text{m}$ in the coordinate measurements for an object of 1.0 meter in length. Therefore, CMMs are treated as high-accurate dimension measurement tools. This is the concept of measurement accuracy—the possible errors in the measurement results. The sensitivity of measurement means the smallest quantities or changes that can be detected by the measurement system. Can we also find a way to define the accuracy and sensitivity of the optical 3D measurement systems? Due to variations of the optical 3D measurement systems, the definitions of accuracy and sensitivity are not that clear in some cases. Here we review the accuracy issue for some of the optical 3D measurement methods.

5.1.1 Geometric Moiré Methods

As described in Chapter 1, the measured results from the geometric Moiré methods are discrete points with known (h, i, j) . Here, h denotes the height of a point from a reference plane, and (i, j) are the location of that point on the image plane. In addition, the points are the central points of the Moiré fringes as shown in Fig. 1.3. There is no height information available for the points located between the Moiré fringes. An interpolation procedure has to be employed by assuming smooth changes between Moiré fringes to obtain the height information for any point not located on a Moiré fringe. If there is a shape change between two adjacent Moiré fringes, this shape change will not show up in the final result. As exhibited in Fig. 5.1, the interpolation procedures just round off small surface change. In other words, the system is not sensitive enough to detect such a detailed surface change.

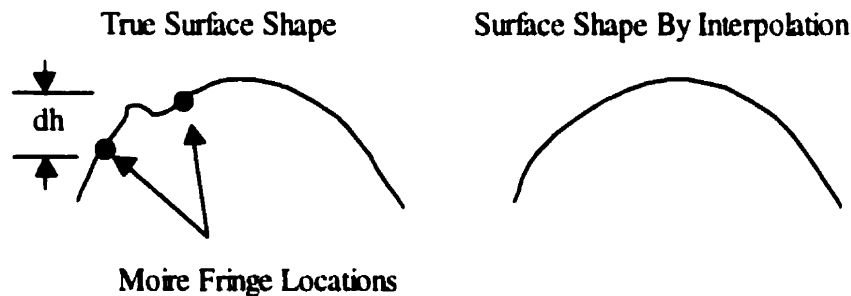


Fig. 5.1 Sensitivity concept in the geometric Moiré methods.

Therefore, a concept of sensitivity or resolution has been introduced to define how sensitive a geometric Moiré system is for detecting surface changes (Sciammarella 1982). The sensitivity, denoted as dh , is equal to the distance between two successive Moiré contour lines. In past years, researchers treated the maximum error in the surface shape measurement as the same as the sensitivity dh . There are many techniques published on ways to increase the number of Moiré fringes in a field of view. The more Moiré fringes you have, the more sensitive the measurement is, due to the smaller distance between consecutive Moiré fringes. However, for each Moiré fringe how accurate the height

information can be obtained is different from the concept of sensitivity, although it could be smaller in value compared with dh . Regarding how accurate each Moiré fringe represents in the height information, few works have been done. One way to determine the accuracy is to carry out an error analysis from Eq. 1.2-1 by assuming errors have been introduced into each of the parameters involved to simulate how the outcome height will be affected. The ideal optical system represented by Eq. 1.2-1 is different from a practical optical system due to a number of imperfect factors or layout. In addition, some noise sources are not included in this kind of error analysis, such as electronic noise. Therefore, how accurate the height information can be is still to be verified. Another reason why there is a lack of accuracy analysis is due to the measured result (h, i, j) , itself. They are neither absolute nor expressed in a form of Cartesian coordinates. For such data, we really have few things to verify its accuracy. In addition, the geometric Moiré methods have a more serious problem to deal with, which is the sensitivity.

5.1.2 Phase-computing-based Optical 3D Measurement Techniques

For the phase shifting or the Fourier transform methods, the situation is different from that of the geometric Moiré methods. First, the sensitivity is no longer a serious problem since the phase calculation is carried out for each pixel, instead of only for discrete pixels. There is no need to interpolate the data. Therefore, the sensitivity of phase-computing-based methods is defined as the smallest change in the surface shape or position that can cause the grating image to shift one pixel in the image plane. Usually, the angle between the projector and the CCD camera plays an important role. Later, an experiment will be carried out to find out how sensitive the current system is.

The direct measured value of these phase-computing-based methods is phase plus its corresponding position on the 2D image plane— $\Phi(i, j)$. Therefore, the accuracy of the phase computation is an important topic, and there are a number of papers dealing with it—Halious & Liu 1986, Creath 1992, and Joenathan 1994. From these papers, the phase computation accuracy is seen to be approximately $2\pi/100$. Various error sources are briefly listed below.

- **Error due to imperfect sinusoidal grating profile:** The line width and the spacing between two consecutive lines may have some error.
- **Error due to digitization:** The digitization noise is caused by the finite number of digitized levels present in the detected intensities. Here 8 bits or 256 gray levels are used in the A/D transformation.
- **Error due to electronic noise:** The background noise in the camera and the frame grabber gives rise to random errors. Each pixel of the solid imager converts light to an electrical charge. If the illumination is not strong enough or the lighting does not fit with the spectral response character of the camera in wavelength, a great deal of electronic noise will be added into the image.
- **Error due to imperfect phase shifting:** This error is relevant in the phase-shifting systems since the grating has to be shifted a very small distance. Due to mechanical reasons, there are always some errors for the real distance the grating travels.
- **Error due to surface quality:** The noise level varies with the surface finish of the object under measurement. If a large amount of detailed surface irregularities exist, there will be noise in the final phase map.

The error sources listed above are for the phase computation only. As indicated in the previous chapters, the phase information and its corresponding image coordinates (Φ, i, j) are not the final measurement results for our system. The (Φ, i, j) have to be converted into Cartesian coordinates (x, y, z) by using a special calibration technique. Therefore, there are some additional errors related to this transformation.

- **Error due to drifting:** All the parameters calibrated are set for the geometry of the sensor head at the time of calibration. The geometry may vary with temperature, and some errors will be introduced by still using the old calibration data.
- **Error due to imperfect calibration:** As described in the previous chapter, a standard object, called the calibration target, is necessary in the calibration. Moreover, the calibration target will be translated at different z positions. The imperfection of

surface flatness and the error of linear movement will bring some errors into the calibration parameters.

Considering all these error sources for both the phase calculation and the Cartesian coordinate calculation, the final accuracy for the Cartesian coordinates (x , y , z) is a very important issue. Standard error analysis, as carried out in Joenathan's paper (1994), is not fully suitable here since some error sources are implicit and are not easy to simulate, especially for those error sources related to the calibration. Fortunately, we have 3D Cartesian coordinates as the final results. They are used also as a tool to check the measurement accuracy. Accuracy will be checked by measuring standard objects with known geometry, such as a flat surface and a cylindrical surface. By comparing the measured values with the standard values, the overall measurement accuracy can be defined. Please note that this way of defining the measurement accuracy is unlike that used in the geometric Moiré methods or any other phase-measuring methods since they can not provide 3D Cartesian coordinates as the final measurement results. This method to define the measurement accuracy is more similar to methods employed by industries for CMMs. The following sections will include the accuracy test results by using a flat surface and a cylindrical surface for the current system configuration.

5.2 Flat Surface Test

The first accuracy test is carried out with a flat surface. A metal surface is carefully machined to have a surface flatness less than $20\ \mu\text{m}$. Then a uniform thin powder coating is put on the surface to give an optical diffusive feature. The thickness of the powder coating is approximately $30\ \mu\text{m}$, and care is taken to make sure there is a uniform distribution over the whole surface. Therefore, after the coating the surface flatness is still less than $20\ \mu\text{m}$. The surface is placed in front of the sensor head at different z values (-22 – $22\ \text{mm}$) in the depth of view, as shown in Fig. 5.2.

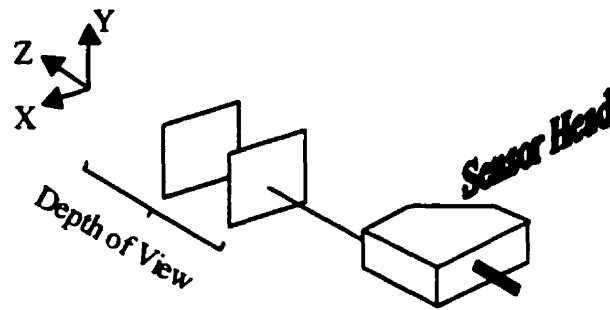


Fig. 5.2 Surface flatness test.

For each position, the flat surface (approximately 80×80 mm) is measured by using the proposed high-speed 3D measurement system. Each measurement generates a point cloud with known xyz coordinates, usually over 100,000 points. A point cloud of a flat surface is shown in Fig. 5.3 with reduced number of points. Since the original surface is flat, all the points measured should be very close to a plane. In order to evaluate the 'flatness' of the data, a least square plane fitting is carried out for all the points, and the deviation of each point is calculated. The results for the total number of points involved in the calculation are given in Table 5.1.

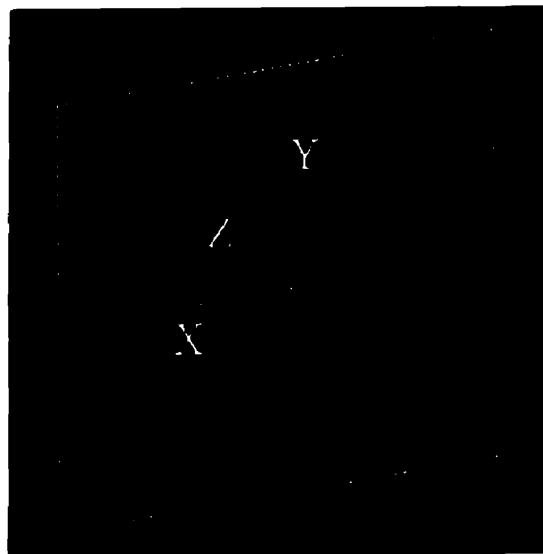


Fig. 5.3 Measurement result of a flat surface—point cloud.

Surface Location Z (mm)	Number of Points	SD (μm)	Surface Location Z (mm)	Number of Points	SD (μm)
-22.000	154,775	11.02	2.000	154,811	10.82
-18.000	154,784	11.06	6.000	154,811	11.05
-14.000	154,806	10.59	10.000	154,812	11.28
-10.000	154,809	10.88	14.000	154,841	11.95
-6.000	154,812	10.54	18.000	154,812	12.99
-2.000	154,812	10.40	22.000	154,810	14.02

Table 5.1 Flat surface test results.

The standard deviation (SD) is calculated by the following equation:

$$SD = \sqrt{\frac{\sum_{i=1}^N (d_i)^2}{N-1}} \quad (5.2-1)$$

where, d_i is the distance from point i to the plane just fitted, and N is the total number of points. Consequently, approximately 68% of the points are within one standard deviation from the fitted plane, and about 97% of the points are within two standard deviations. The maximum deviation is caused by isolated noise, which could be bigger in value than the standard deviation. However since those noisy points are relatively small in number, their effects can be limited by any surface filtering process.

The average standard deviation for all 12 tests is approximately 11.38 μm , and the deviation is relatively small around the center of the depth of view. Therefore, it is recommended to carry out measurements around the center of the depth of view whenever possible. The flat surface tests show very good results, and it is better than the

overall accuracy target we set for the system— $\pm 50 \mu\text{m}$. In the next section, we will test accuracy on curved surfaces.

5.3 Cylindrical Surface Test

A cylindrical surface is machined on an aluminum rod with a diameter of 75.810 ± 0.004 mm. The aluminum surface is very shiny after machining, and an appropriate coating is needed to reduce noise in the images. After coating, the cylindrical surface is placed

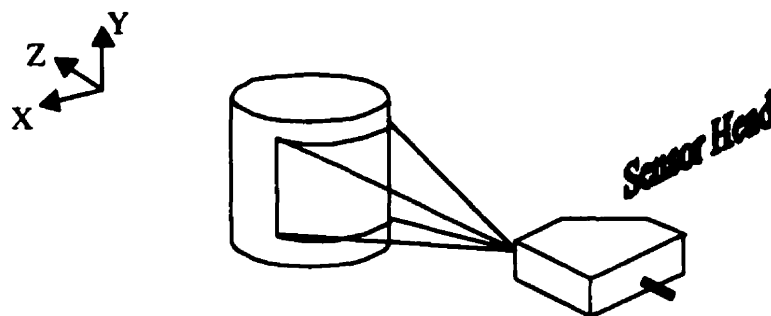


Fig. 5.4 Cylindrical surface test.

approximately in the center of the depth of view, as shown in Fig. 5.4. Then a portion of the cylindrical surface (approximately 50×50 mm) is measured by using the proposed optical system to generate 1,100 points as the results. These points are displayed in Fig. 5.5. Since the original surface is cylindrical, all the measured points are very close to a cylindrical surface with a diameter of 75.81 mm. The data deviation from the standard cylindrical surface is evaluated at different y locations (-25 – 25 mm). The best fit results at $y=0.0$ are displayed in Fig. 5.6, and Table 5.2 summarizes the best-fit results for all other y locations.

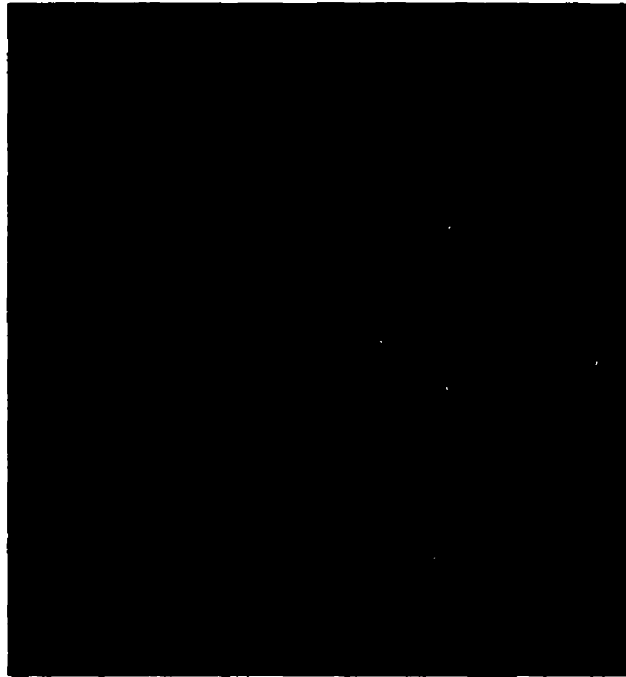


Fig. 5.5 Point cloud display of the measured data on a cylindrical surface.

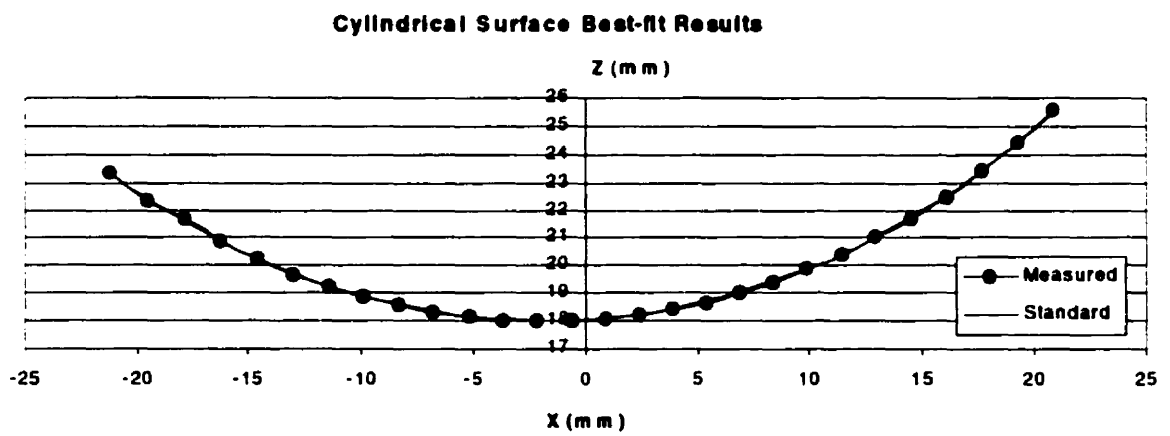


Fig. 5.6 The best-fit results at $y=0.0$.

Y (mm)	-25.0	-20.0	-15.0	-10.0	-5.0	0.0	5.0	10.0	15.0	20.0	25.0
SD (μm)	30.5	25.7	31.5	36.8	32.3	28.7	33.0	34.5	33.9	35.8	30.4

Table 5.2 The best-fit results of the cylindrical surface.

The accuracy test done on a cylindrical surface is slightly different from those carried out on a flat surface since for curved surfaces the lateral coordinates, x and y , will play a role. Any error with x and y coordinate calculation will affect the final data deviation. The results shown in Table 5.2 are still better than the accuracy target we set for the overall measurement.

5.4 Sine Vise Test

A sine vise is an industrial tool to create accurate angles by changing the height of gauge blocks underneath. As shown in Fig. 5.7, a sine vise is placed in front of the sensor head. By changing the height of the gauge blocks, surfaces at different angles are created.

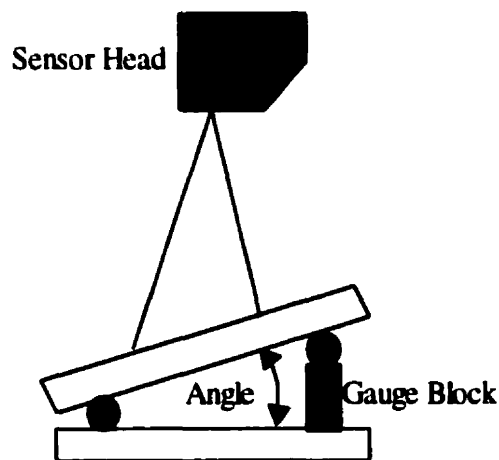


Fig. 5.7 Accuracy tests with a sine vise set at different angles.

Since the accuracy of the gauge blocks is less than $0.5 \mu\text{m}$, the angles created by this method have an accuracy of approximately $\pm 0.0036^\circ$. A portion of the top surface of the sine vise is measured for each different angle, and the deviation of each point to the ideal flat plane at that angle is evaluated to verify the measurement accuracy. Table 5.3 summarizes the results.

Test	1	2	3	4	5	6	7	8	9	10
Gauge Block Height (mm)	3.81	5.08	7.62	10.16	12.7	16.51	17.78	20.32	22.86	25.4
Angle ($^\circ$)	1.719	2.292	3.44	4.589	5.739	7.47	8.048	9.207	10.37	11.54
Number of Points	350	350	350	350	350	350	349	349	349	349
SD (μm)	31.94	33.15	37.96	43.55	44.77	47.57	52.67	50.77	51.89	50.18

Table 5.3 Accuracy test results on the sine vise.

From Test 1 to Test 10, the surface traveled about 30mm in the Z direction. Compared to the depth of view (50mm), we found that the accuracy gets worse when a surface is located close to the two ends of the depth of view. From Table 5.3, we can see that the overall accuracy objective is barely maintained in this case.

5.5 Sensitivity Test

In the previous section, the measurement accuracy on flat surfaces and curved surfaces has been evaluated. The objective of the accuracy tests is to assess how much error is in the measured data. In this section, we will decide how small a surface change can be detected by the system, i.e. how sensitive the system is. Note here, the sensitivity we are considering is the out-of-plane sensitivity, in other word the sensitivity in the Z direction

since the system is primarily designated for out-of-plane measurement. We will not assess how sensitive the system is for the measurement in the X and Y directions.

The sensitivity is mainly decided by the angle between the projector and the CCD camera. The bigger the angle is, the more sensitive the system will be. However, bigger angles will reduce the depth of view. In our current configuration, the angle is about 30 degrees. Instead of assessing the sensitivity theoretically, a test will be carried out to evaluate the practical sensitivity. Again, the flat surface used for flat surface accuracy test is used here. As shown in Fig. 5.2, the flat surface is placed at different positions in the depth of view. At each location, the flat surface is moved by a small distance, usually in microns. The surface is measured twice (before and after the movement) to see whether or not the small movement is included in the measured results. Since the smallest read-out of our translation stage is 10 microns, the smallest movement we can have is 10 microns.

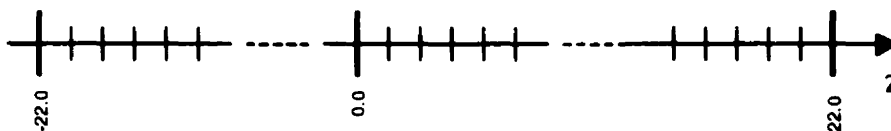


Fig.5.8 Sensitivity test location in the depth of view (step size=10 microns).

As shown in Fig. 5.8, three locations inside the depth of view ($z = -22.0$, 0.0 , and 22.0 mm) are selected to carry out the sensitivity test. The flat surface is placed at these locations, then five small movements (step size = 10 microns) are introduced in the Z direction. The surface is measured at each step to create a point cloud, and then the raw point cloud is plane-fitted. Finally, the distances between these computed planes are compared with the known step size (10 microns). The results are shown in Table 5.4.

The results in Table 5.4 show that under the current configuration the system can detect as small as 10 microns displacement in the Z direction. The step size of 10 microns is

also close to the accuracy of the translation stage, therefore an error of 1 or 2 microns is very reasonable. As mention previously, the sensitivity can be increased by changing the angle between the CCD camera and the projector. However, at this moment it is not necessary to do so.

Location z (mm)	Standard Movement (μm)	Step Number	Points Measured	Measured Movement (μm)	Error (μm)
-22.0	10.0	1	154,807	10.0	0.0
		2	154,808	8.0	2.0
		3	154,812	9.0	1.0
		4	154,811	9.0	1.0
		5	154,807	8.0	2.0
0.0	10.0	1	154,808	10.0	0.0
		2	154,811	10.0	0.0
		3	154,808	10.0	0.0
		4	154,809	10.0	0.0
		5	154,811	8.0	2.0
22.0	10.0	1	154,812	10.0	0.0
		2	154,810	10.0	0.0
		3	154,811	10.0	0.0
		4	154,810	9.0	1.0
		5	154,810	12.0	-2.0

Table 5.4 Sensitivity test results.

5.6 Summary

In this section, various error sources have been pointed out. Instead of assessing the overall measurement accuracy theoretically, several experiments have been carried out to evaluate the accuracy from a practical point of view. The *xyz* coordinates as the measured results make it possible to evaluate accuracy this way. Three tests on flat or

curved surfaces show that the overall accuracy objective, $\pm 50 \mu\text{m}$, has been obtained. Regarding the sensitivity of the measurement, the experiment shows that an out-of-plane displacement as small as $10 \mu\text{m}$ is detectable. In addition, the experiments show that near the middle of the depth of view the error is relatively small.

Finally, the data quality varies with the surface finish of the object under test. Very rough surfaces will create more random errors in the xyz coordinates. A number of ways can be employed to reduce this kind of error. One of the ways is to filter the original grating image to remove random noise.

CHAPTER 6

BIAXIAL EXTENSION TESTS OF POLYMERIC MATERIAL

6.1 Introduction

6.1.1 Background

Plastics are modern, synthetic materials that have superior properties, such as hygienic barrier properties, lightweight, and durability, which contribute significantly to our health and quality of life. In automotive applications they offer light-weight performance which in turn improves gas mileage; in packaging applications, they protect our food from contamination and many products from damage; in medical applications they are used to improve our quality of life and save lives through IV and blood bags, artificial hips and limbs and disposable syringes. In construction, plastics help insulate and decorate our homes and are used extensively in plumbing and electrical applications. Plastics are also very energy efficient. Studies show that it takes less energy to make a product from plastics than just about any other material. For example, it takes less energy to make a plastic bottle than a glass bottle; vinyl siding than aluminum siding; plastic pipe than steel pipe; and so on.

Blow molding and injection molding are two common techniques to fabricate different shape plastic products. As shown in Fig. 6.1, thermoforming technologies require a pre-manufactured thermoplastic sheet, which is clamped, heated, and shaped into or over a mold. Despite the fact that thermoforming has been used extensively in recent decades, the techniques used were mostly based on experience, and therefore were rather empirical. How to test the thermoformability of plastic sheets was always a challenging task for engineers. For example, in the past if one wanted to know whether a certain plastic sheet material could be formed into a particular shape, the only solution before was to build a mold and try it out. Now, with the powerful computers, engineers can simulate the whole thermoforming procedure using different constitutive material models

to represent the behavior of the polymeric material. By doing so, it is possible to know whether or not a particular product can be made and in addition how to make it, including what temperature and airflow rate should be applied, and what thickness the final product will be. However, as the input parameters of these simulation models, the material constants of polymeric material under elevated temperatures are often lacking. There is an increasing need for the polymeric material to be adequately characterized since the performance of these simulation models depends on how accurate the material models and parameters can be determined. Therefore, this recent progress in computer-aided plastic processing demonstrates a strong need for accurate description of the material behavior relating stress, strain, and temperature.

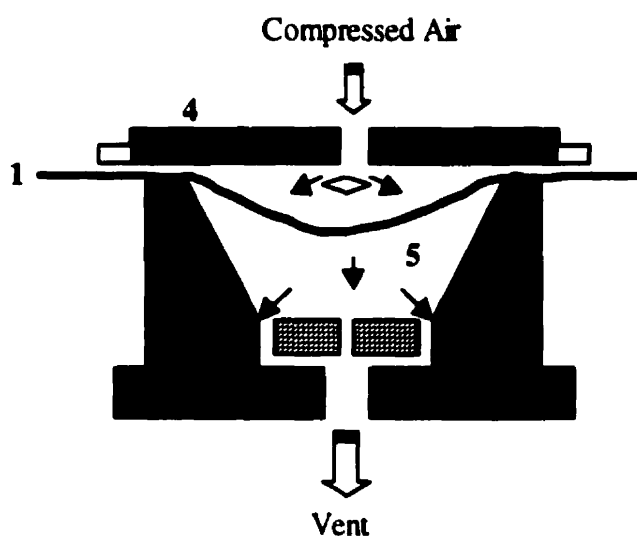


Fig. 6.1 Thermoforming process: (1) preheated thermoplastic sheet; (2) mold base plate; (3) mold body; (4) pressure plate; (5) trapped air.

6.1.2 Inflation of Plane Circular Membrane and Basic Equations

As mentioned in the previous section, accurate material properties are needed in order to obtain correct results from simulation models. However, the properties of plastics are directly dependent on temperature, strain rate, and deformation conditions (uniaxially or biaxially). In thermoforming, the deformation of a polymer membrane from a 2D flat sheet to a 3D shape is essentially biaxial and occurs above the material's glass transition

temperature (usually $>100^{\circ}\text{C}$). In addition, the deformations occur very rapidly, usually less than a second for the whole event, resulting in high strain rates. A number of devices are available commercially for uniaxial extension tests, such as stretch rheometers. However, predicting the deformation of a viscoelastic membrane under biaxial stretching based solely on the behavior exhibited in uniaxial extension often results in large errors, especially for large deformations. Therefore, it is generally more desirable to use a biaxial stretching test at rates approximating those for the application being considered to characterize the material properties under biaxial extension.

One of the techniques, which has been used with success to study the behavior of polymeric materials in biaxial extension, is the bubble inflation test. A sheet of the polymeric material to be studied is clamped between two plates, both of which have circular concentric holes cut in the middle. An inflation medium, a gas or liquid, is introduced under pressure to a chamber mounted on one side of the plate. The pressure difference, ΔP , between the two sides of the sheet will cause the sheet to deform into a bubble, as shown in Fig. 6.2. Usually ΔP and the deformation of the sheet are monitored as functions of time to provide data from which material constants can be determined.

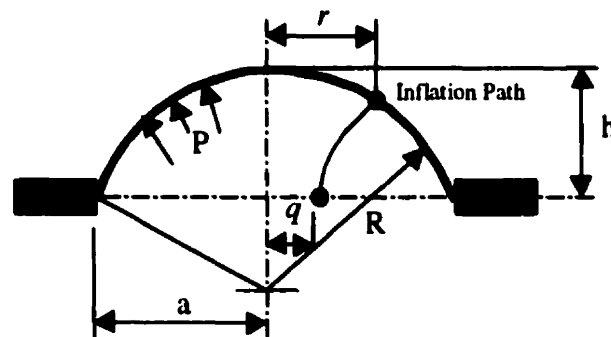


Fig. 6.2 Geometry of a bubble.

The use of the bubble inflation test to characterize the material properties of polymeric materials in biaxial extensions is not a new technique. Treloar used a bubble inflation device in 1944 to test rubber sheets (Treloar 1944). Later in 1951, Rivlin & Saunders

used a similar device to test a rubber elasticity theory (Rivlin & Saunders 1951). Joye, Poehlein and Denson found the technique useful in determining extensional flow properties in 1972 (Joye, Poehlein & Denson 1972). The inflation is often monitored by a camera filming either a pattern painted on the sheet or the height of the bubble (Schmidt & Carley 1975, and Derdouri, Connolly & Khayat 1998).

These researchers all considered an idealized sheet inflation in which the deformation is assumed to be uniform over the entire sheet so that a spherical shell of uniform thickness is formed as shown in Fig. 6.2. For the idealized equibiaxial extension, the polymer sheet is stretched by equal amounts in two orthogonal directions, and the through thickness stress σ_3 is taken as approximately zero, i.e. plane stress. At any instant, the bubble is assumed to be part of a thin spherical shell under internal pressure as shown in Fig. 6.2. The relationship between the radius and height of a spherically symmetric bubble is:

$$R = \frac{a^2 + h^2}{2h} \quad (6.1-1)$$

And from classical shell analysis, the following relationship for the stress is obtained:

$$\sigma_1 = \sigma_2 = \frac{P \cdot R}{2t} \quad (6.1-2)$$

where R is the radius of curvature of the spherical shell and t is the thickness. The surface area of a spherical segment is $(2\pi Rh)$, so that if the material is assumed to be incompressible, the thickness is given by:

$$t = t_0 \times \left(\frac{a^2}{2Rh} \right) \quad (6.1-3)$$

where t_0 is the original thickness. By substituting Eq 6.1-3 into Eq. 6.1-2, the relationship between the stress and the height is given by:

$$\sigma = \frac{P \cdot (a^2 + h^2)^2}{4a^2 t_0 h} \quad (6.1-4)$$

The stretch ratio, λ , is associated with the change in surface distance (arc length) from the pole to the clamped edge of the sheet so that:

$$\lambda = \frac{\alpha \cdot R}{a} \quad (6.1-5)$$

where angle α is shown in Fig. 6.2, and can be obtained from:

$$h = R \cdot (1 - \cos \alpha) \quad \text{or} \quad \frac{a}{R} = \sin \alpha \quad (6.1-6)$$

The stretching strain ε , which is uniform over the entire surface, is then given by:

$$\varepsilon = \ln \lambda = \ln \left(\frac{\alpha R}{a} \right) \quad (6.1-7)$$

The pictures of the bubble inflation from a side view are 2D images, but after a simple calibration of the scale factor, some 1D quantities can be obtained, such as the height at the pole or the diameter of a ring. Thus, the knowledge of pressure P together with the height of bubble h as functions of time is sufficient for the determination of the stress and strain.

The following assumptions have been used in this development: (1) the biaxial deformation is uniform over the whole bubble surface; (2) the bubble geometry is spherical; and (3) the material is incompressible. In fact, uniform stretching over the entire sheet is not possible by considering the following: (1) the clamping plates restrain the displacement of polymer sheet adjacent to them and different degrees of slippage

occur at different locations; and (2) for the tests conducted at elevated temperatures the temperature distribution is not uniform over the entire circular sheet. If the assumption of uniform stretching is not valid, the bubble shape will not be spherical. Therefore, all the equations derived above will be jeopardized. So, what is the real shape for a bubble during its different evolution stages?

From 2D side-view pictures, it is hard to check the sphericity of a bubble since the surface curvature at different locations is unavailable. Sometimes, the 2D bubble images can be projected onto a big screen to get more details on the bubble profile. However, some errors are introduced in locating the bubble edges since all the processing is subjective on an operator's decision. Another shortcoming of the side-view pictures is the difficulty of measuring the initial deformation around the starting point of applying compressed air. The polymer sheets undergo thermal deformation due to the heating process. Therefore, the polymer sheets are no longer flat even though no compressed air has been applied. As shown in Fig. 6.3, a pressure plate has to be used in the bubble inflation tests. Small membrane deformations, i.e. less than the thickness of the upper plate, will not be seen in the pictures. In order to overcome these detailed disadvantages, a more robust measurement system is needed to monitor the evolution of a polymer bubble more accurately.

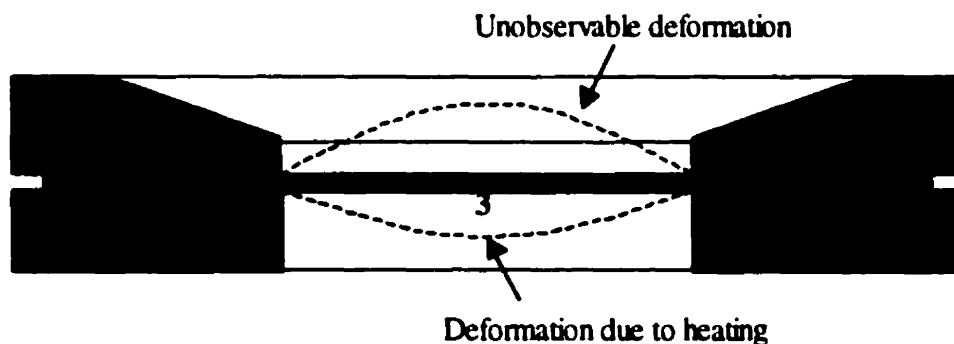


Fig. 6.3 Cross-section view of the bubble inflation test: (1) upper plate; (2) lower plate; (3) polymer sheet.

6.1.3 Application of High-speed Optical Measurement System to Bubble Inflation Tests.

The optical high-speed measuring system described in previous chapters is a very suitable tool for the bubble inflation tests, especially for the early deformation stage. The significance of this measurement can be stated as follows: First, successful use of the optical, high-speed, whole-field measuring system can provide whole-field out-of-plane deformation information with high accuracy. By utilizing detailed 3D information instead of only 2D images, it becomes possible to calculate surface curvature at any location. Therefore, the uniformity of deformation and the sphericity of a bubble can be studied accurately. In addition, the measurement during the early inflation stage is possible. All deformations are observable, even during the early stage. Second, the results obtained from these bubble inflation tests will provide thermoforming engineers a chance to check the thermoformability of different materials. Furthermore, the tests themselves will also provide a tool to verify and improve different analytical models to offer more precise control over the entire thermoforming process.

With this in mind, a joint research project was launched with the Industrial Material Institute (IMI) of the National Research Council of Canada (NRC) in Boucherville, Quebec. The high-speed optical measurement system developed at McGill University was integrated with the bubble inflation testing facility of IMI/NRC, and all the inflation tests were carried out at IMI/NRC. In the following sections, the details of the inflation tests and the measurement results will be presented.

6.2 Experimental Setup

Fig. 6.4 shows an overall view of the experimental setup. A thin square sheet of thermoplastic material is clamped between two plates that leave a 2.5-inch circle at its center exposed to two infrared heating lamps on both sides. After being heated to a certain temperature, the specimen is blown upward into a bubble of an approximately hemispheric shape by inflating with compressed air at room temperature into the lower chamber. The optical sensor head is mounted over the specimen looking downward to

measure the whole deformation history of the polymer sheet. In the meantime, a pressure transducer is used to record the pressure inside the chamber. By using the MCDL, the pressure signal is correlated with each image frame. Elapsed time for these tests was usually less than 1.0 second.

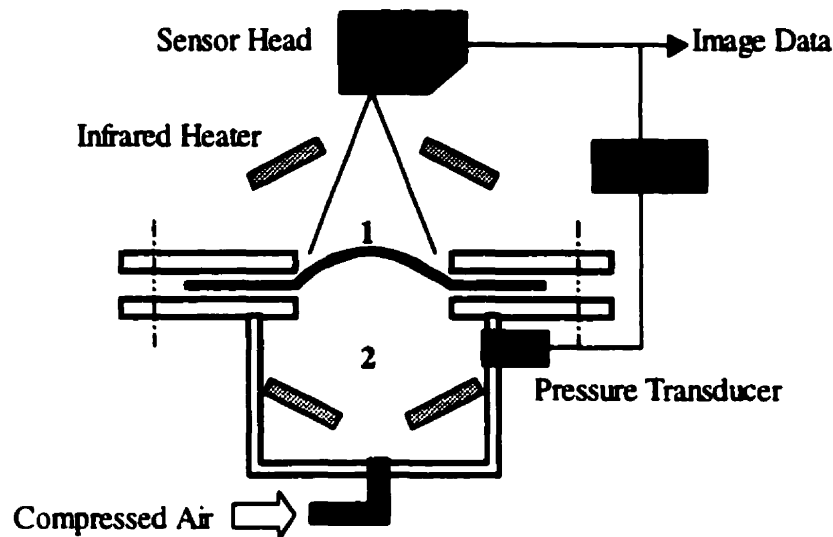


Fig. 6.4 The bubble inflation experimental setup:
(1) polymer sheet; (2) pressure chamber.

Three materials were used in our tests: high impact polystyrene (HIPS), acrylonitrile butadiene styrene (ABS), and high-density polyethylene (HDPE). The raw materials were cut into 110×110 mm square sheets. The thickness of HIPS and HDPE is 1.0 mm and is 1.5 mm for ABS. A total of 27 tests were carried out at temperatures which ranged from 130°C – 180°C and at different airflow rates—3.0, 5.0, and 8.0 liter/second. The high-speed optical measurement system is capable of measuring the deformation up to 1000 times per second, but was usually operated at 250 frames per second with a shutter speed of 1/250 second. That means the bubble shape is measured every four milliseconds for a total period of 2.2 seconds. An infrared camera is mounted beside the optical sensor head to measure the temperature distribution of the specimen. In the future, two infrared thermometers will be installed to monitor the temperatures on both sides of the specimen,

and their readouts are used to control the temperature automatically. The heating procedure usually took approximately 5 minutes in order to create a uniform temperature distribution through the thickness of the specimen. During the heating, the specimen experienced some warping due to the rise of temperature, even though there was no pressure difference on both sides of the polymer sheet. This thermo warping is clearly shown in our measurement results.

The complete step-by-step operating sequence may be summarized as follows: (1) start with initial conditions at room temperature; (2) the original specimen surface shape is measured; (3) the infrared camera is turned on to monitor the temperature; (4) the heaters are turned on to heat the sample for approximately 5 minutes to ensure the uniformity of temperature; (5) the optical sensor head is turned on to start recording; (6) a valve is opened for compressed air to flow into the chamber to generate a bubble; (7) the valve is closed when the bubble bursts; and (8) 30 minutes of cooling process. During the cooling, the digital images saved in the high-speed camera's memory can be replayed in order to select an 'action' sequence. Then, the selected sequence is transferred to the computer for further *xyz* coordinate calculation. From the image data transferred from the high-speed digital camera, the surface shape of a portion of bubble surface is calculated in a form of an array of points with known *xyz* coordinates. Due to the limitation of the depth of view of the optical measuring system, only the early portion of the bubble evolution is measured.

6.3 Experimental Results and Data Analysis

6.3.1 Overview of Measurement Results

The measurement result of a bubble inflation test is an array of points with known *xyz* coordinates, as displayed in Fig. 6.5. Each white dot in the figure represents a point in 3D space. Please note that the white dots shown in the figure are a subset of the actual points measured. Since the *xyz* coordinate calculation is carried out for each pixel in the image and the total number of pixels (over 200,000) is too many for most applications, a reduction factor is used to select a subset from the original point cloud. For example, to

save one point in every five points in a row and to use one row in every five rows. The circle in Fig. 6.5 represents the circular opening in the upper plate, which is shown by rectangular edges. The coordinate system, which is virtually associated with the optical sensor head, is also shown in the figure with the Z-axis approximately being aligned with the inflation direction.

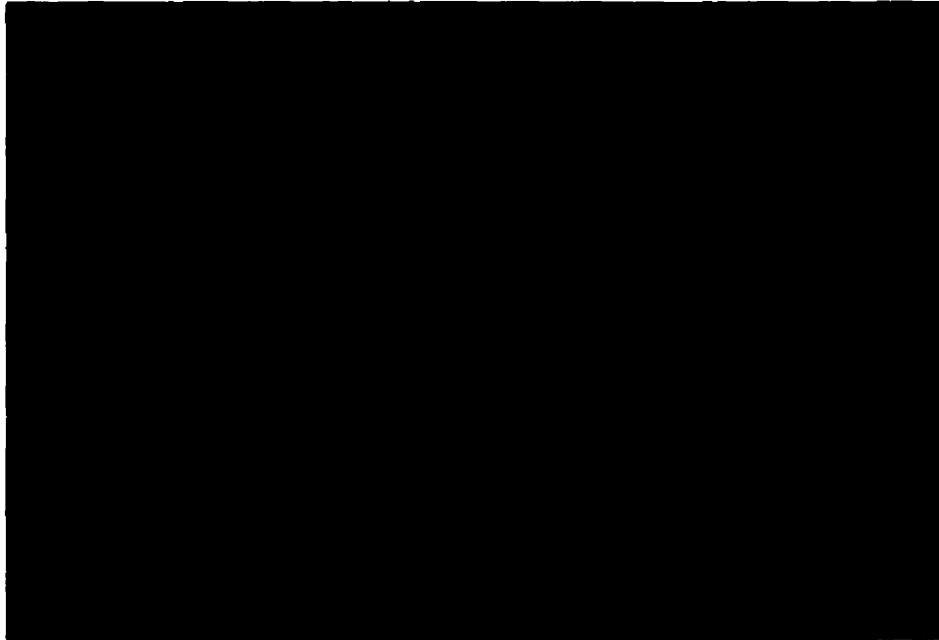


Fig. 6.5 The measurement result of bubble inflation: ABS @ 150 Celsius & 3.0 l/s airflow rate. The measurement was taken at 160 ms after inflation.

As shown in Fig. 6.5, only a portion of the surface of a bubble is measured and digitized into 3D points. The reason is that for coordinate calculation a rectangular window, as shown in Fig. 6.6, has to be defined in order to carry out all image-processing works. Therefore, only the points inside this rectangular window are processed to obtain coordinate information. The white dots in Fig. 6.5 can be connected by straight lines to provide a wireframe display of the bubble shape, and this is shown in Fig. 6.7.

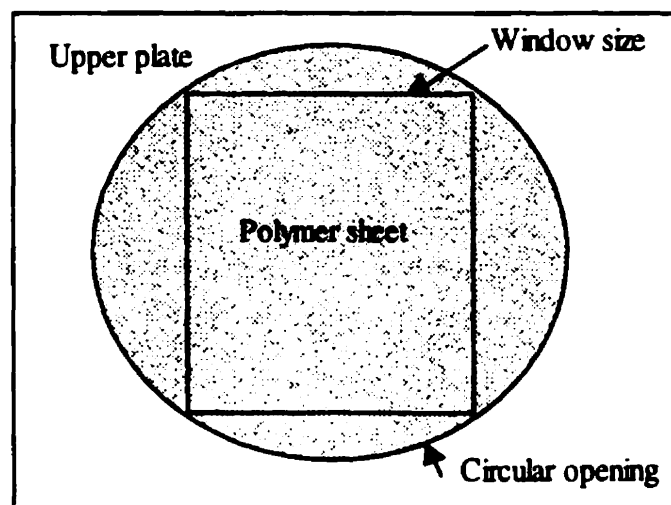


Fig. 6.6 Rectangular xyz coordinate calculation window.

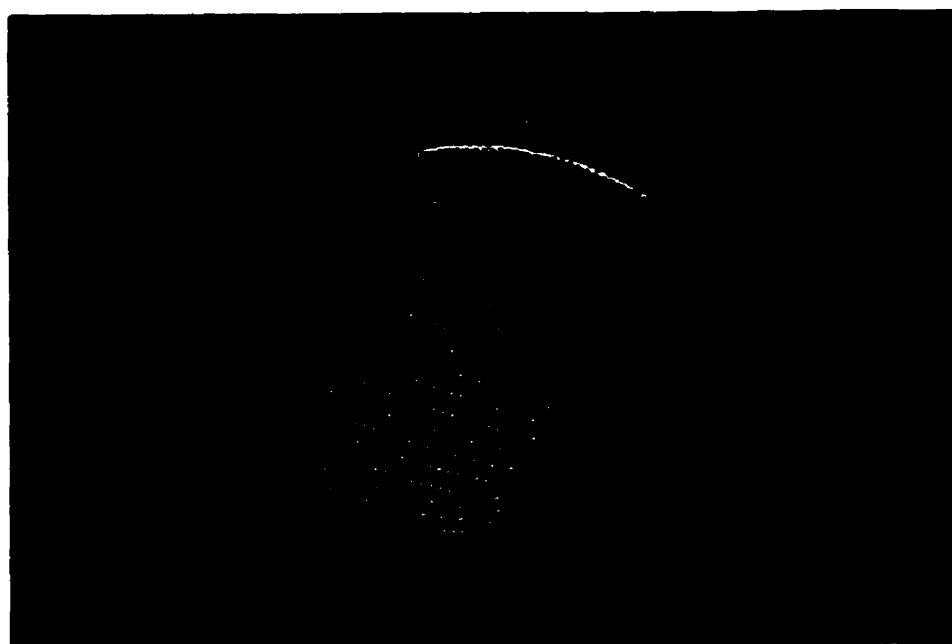


Fig. 6.7 Wire-frame display of Fig. 6.5.

Since the xyz coordinates of all the points in Fig. 6.5 are known, and these coordinates are given with respect to a single fixed Cartesian coordinate system, these raw measurement results, which are also called the *point cloud*, become a source for further analysis of the

bubble surface characteristics, such as the surface curvature. In addition, the point cloud shown in Fig. 6.5 is just one measurement taken at a certain time. Similar measurements on the bubble shape are carried out 250 times per second in our tests, generating a huge point cloud set for each bubble. All our succeeding analyses about the shape of a bubble are based on this set of point cloud data.

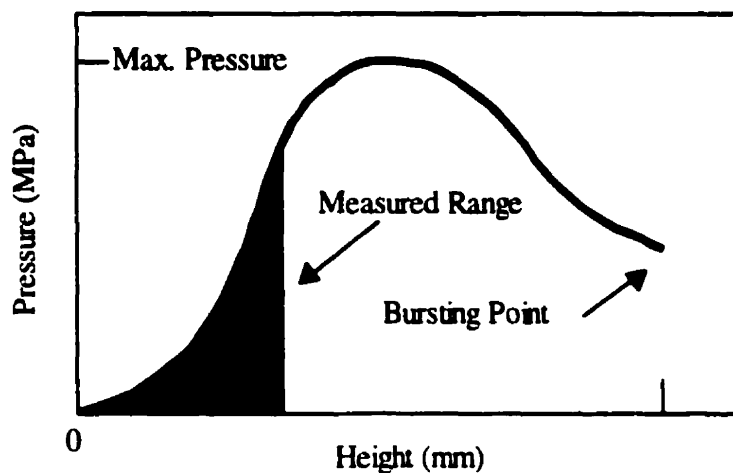


Fig. 6.8 Pressure vs. height in a typical bubble inflation test.

Fig. 6.8 shows a schematic curve of pressure vs. height in a bubble inflation test. It is observed that the pressure will increase along with the bubble height at the beginning of inflation. After the pressure reaches a maximum, the pressure will decrease, although the height continues to grow. At a certain point, the bubble begins to grow rapidly and bursts or fails at the pole region.

The temperature, material, airflow rate, and thickness play very important roles in a bubble inflation test. To change any of these factors can alter the test results, such as the height and the maximum pressure, dramatically. In our tests, the bubble height can go up to approximately three times of the radius of the circular opening ($h/a \approx 3.0$). However, due to the limitation posed by the sensor head fixture, our measurement can only cover the first one third of the blowing process ($h/a = 0.0-0.8$). The measuring range is shown in Fig. 6.8 and the measurement stops just before the pressure reaches its peak. Fig. 6.9

shows a graph of the pressure vs. height of ABS at 150°C and 3.0 *liter/sec* airflow rate. Using Eqs. 6.1-5 & 6.1-7 and the height vs time measurement, the resulting strain rates are on the order of 1.0 s⁻¹.

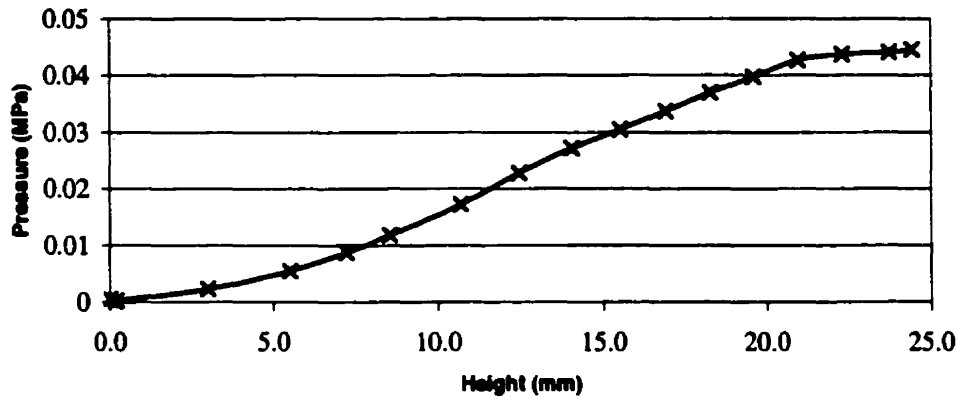


Fig. 6.9 Pressure vs. Height for ABS @ 150 Celsius and 3 *liter/s* airflow rate.

In the literature, several researchers have indicated that beyond $h/a=1.2$, the bubble deformation becomes noticeably more pointed at the pole (Joye, Poehlein & Denson 1972). Thus, the bubble is no longer a simple spherical segment. Later, Pan and Watt set a more strict number, $h/a=1.0$ instead of 1.2 (Pan & Watt 1996). They all claimed that before $h/a=1.0$ the bubble is reasonably spherical, and the analysis should be based on this range. Our measurement covers $h/a=0.0-0.8$, and it will provide an accurate verification of these claims.

In this section, some important aspects of the measurement result of the bubble inflation test have been described, especially the measurable range. In the next section, the real shape of a bubble will be analyzed.

6.3.2 Real Shape of A Bubble

A test is carried out on the ABS material at 150°C and 3.0 *liter/sec* airflow rate. A total of approximately 100 frames have been saved, and a subset of these images are fully processed to generate *xyz* coordinates. The raw point cloud data calculated from frame

#150, which is taken at 160 ms after inflation, has been shown in Fig. 6.5 and 6.7. The bubble height at that moment is approximately 12.0 mm ($h/a = 0.378$). As shown in these two figures, not all the polymeric material inside the circular opening deforms into a spherical shape. There is a relatively rigid ring along the fixed circumference with little deformation. At this moment, 160 ms have elapsed since applying the compressed air. The width of this rigid ring is about 8.45 mm. By observing other images, we find this rigid ring is existing through all bubble inflation stages, even after $h/a \geq 1.0$.

The measured shape is compared to the assumed spherical shape in Fig. 6.10. The flat base line is the original polymer sheet before heating. On the top, an arc is created by using the information of the pole and the fixed circumference. The real bubble shape at this moment is the curve between the base line and the idealized arc. The maximum deviation, which occurred at the rigid ring area, is approximately 2.8 mm. Compared to the bubble height at this instant (12.0 mm), this is an error of about 23%.

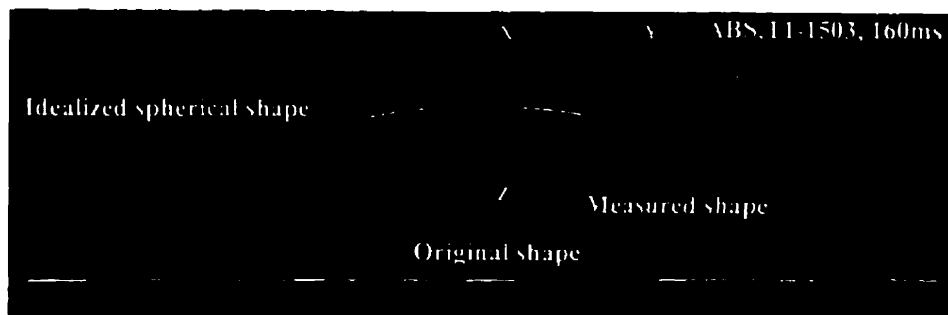


Fig. 6.10 Cross-sectional shape of a bubble at 160 ms after inflation.

In their 1972 paper, Joye, Poehlein, and Denson claimed that at room temperature (23°C) the deviation from true sphericity is perhaps 5% for the deformations where $h/a < 1.2$. The measured result showing here is at an elevated temperature—150°C and the deviation is much worse. Evidently, the temperature gradient in the radial direction and boundary condition play a central role in preventing the bubble from deforming into a real spherical shape in elevated temperature cases. If we can achieve a uniform temperature

distribution in the experiments, with no doubt the final shape will be closer to a sphere. However, the height of the dome will not be as same as that with the temperature non-uniformity existing. Most likely, the bubble height will increase. Therefore, it is difficult to know how much the error has been introduced into the calculation of material properties, and whether or not the final error is negligible.

The bubble profile in Fig. 6.10 is further analyzed to see what the curvature distribution is. Two principal curvatures are usually used in case of a curved surface. In bubble inflation, the curvature distribution at a certain height in the circumferential direction doesn't change much. The curvature distribution in the meridian direction on a cross-section line through the pole is studied first. The curvature k of a curve is defined as the absolute value of the rate of change of the tangent angle with respect to the arc length, and the radius of curvature is defined as $1/k$. A large curvature, i.e., small radius of curvature, means the curve is turning rapidly, while a small curvature, i.e., large radius of curvature, means the curve is nearly straight. In the extreme cases, the curvature is zero and the radius of curvature is infinite for a straight line. The discrete points with known xyz coordinates, which represent the bubble profile, are fitted into a 3D curve. Then the curvatures at different locations along the curve are calculated and plotted.



Fig. 6.11 Curvature distribution at 160 ms after inflation and $h/a=0.378$.

As shown in Fig. 6.11, the curvature plot consists of a number of circles centered on the curve, so that the radius of each circle is proportional to the curvature at that location. A large circle means the bubble shape is turning rapidly at this location, while a small circle

means the bubble shape is flat. Due to our viewing direction, these curvature circles are shown as small line segments. From the curvature plot, we can see that at this moment the curvature is almost uniform in the region near the pole. With the increase of the distance to the pole, the curvature decreases. There is a point on each side of the pole where the curvature is zero since at this point the second derivative of the profile curve is zero. Starting from this zero-curvature point, the curve changes its shape from concave upward into concave downward. It is very clear that the problem occurs near and beyond these zero-curvature points (inflection points), even though at 160 ms after inflation and the h/a ratio is only 0.378. Another observation is that on both sides of the pole the curvature distribution is very symmetric as expected.

The curvature distribution shown in Fig. 6.11 is for a cross sectional curve passing through the pole. Regarding surface curvature, some analyses have also been performed as shown in Fig. 6.12. The principal curvatures, k_1 and k_2 , at any location on the bubble surface have been calculated. The Gaussian curvature, $k_1 \times k_2$, at different locations on the bubble surface is displayed in colors in the figure. Again, the figure shows that the surface curvature distribution is not uniform on the entire bubble surface.

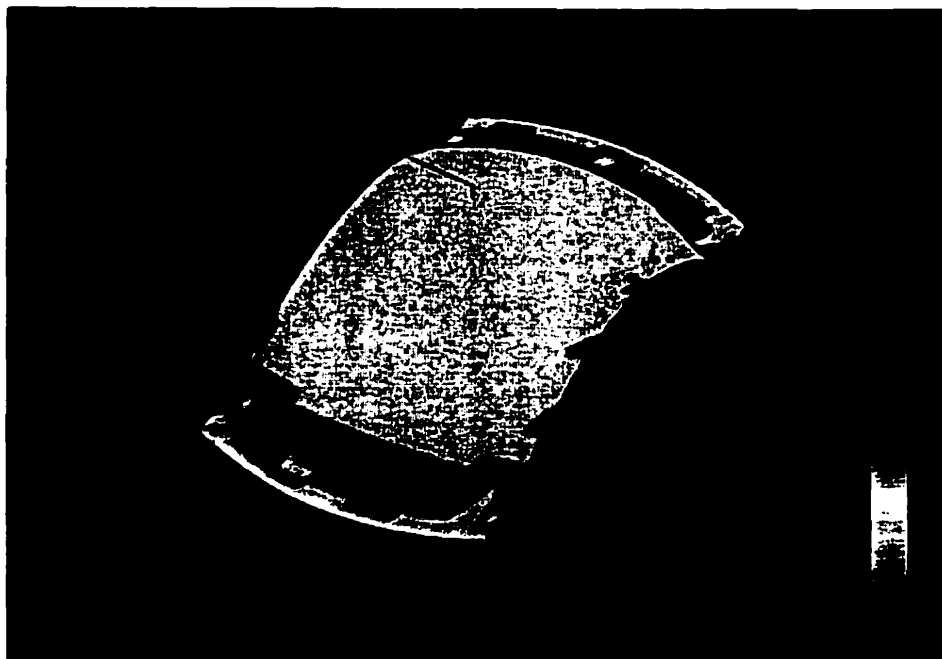


Fig. 6.12 Gaussian surface curvature distribution at 160 ms after inflation ($h/a=0.378$).

We have identified that the surface curvature distribution is not uniform on the entire surface of a bubble. Furthermore, there is a region near the pole where the curvature is relatively uniform. In the following, we will explore how this region changes during different inflation stages. Fig. 6.13 shows the inflation of a bubble at different times.

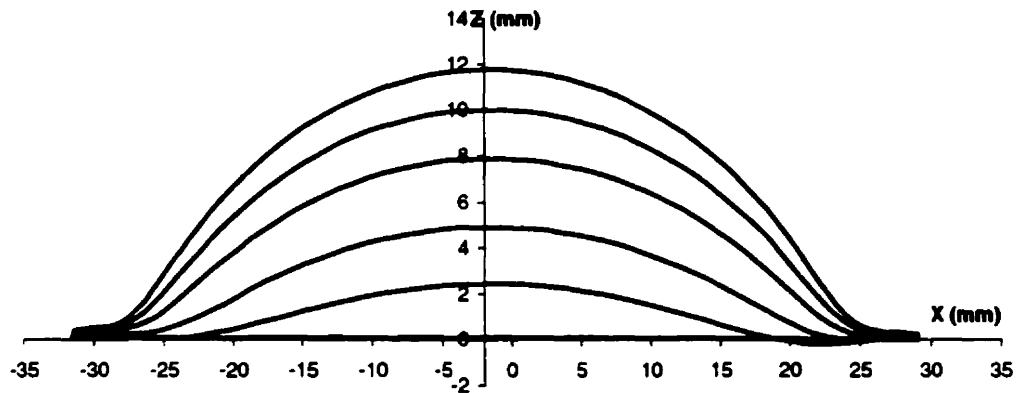


Fig. 6.13 The bubble inflation at different times: from bottom up at time 20, 40, 80, 120, and 160 msec. The zero deformation is defined as the polymer sheet position before heating.

The region of uniform curvature distribution is defined as the area between the two first inflection points on each side of the pole. As shown in Fig. 6.14, the curvature distribution along a cross-sectional curve of the bubble is calculated at different times. At time zero, the polymer sheet is no longer flat, and it has a concave upward shape due to the heating. The bubble inflation starts from this non-flat shape. At time 20 ms shown in Fig. 6.14 (b), the central portion of the bubble deforms into a concave downward shape, but in the region close to the fixed circumference the specimen has not fully recovered from the deformation caused by heating. There is one extra inflection point on each side of the pole. The horizontal distance between the first inflection point and the fixed circumference is about 16.4 mm. As shown in Fig. 6.14 (c), at time 40 ms the distance between the first inflection point and the circumference is decreased to 13.5 mm. The deformation due to heating and the inflation are still co-existing. The bubble is a bit flatten in the pole area than it should be. At time 160 ms shown in Fig. 6.14 (d), there is only one inflection point on each side of the pole. It means that the bubble has fully

recovered from the warping deformation due to heating, and the distance between the first inflection point and the fixed circumference is further decreased to 8.45 mm. The bubble is still a little bit flatten in the pole area, but the situation is better than 120 ms earlier. Therefore, the uniform region is increasing with the time for $h/a=0.0 \sim 0.378$.

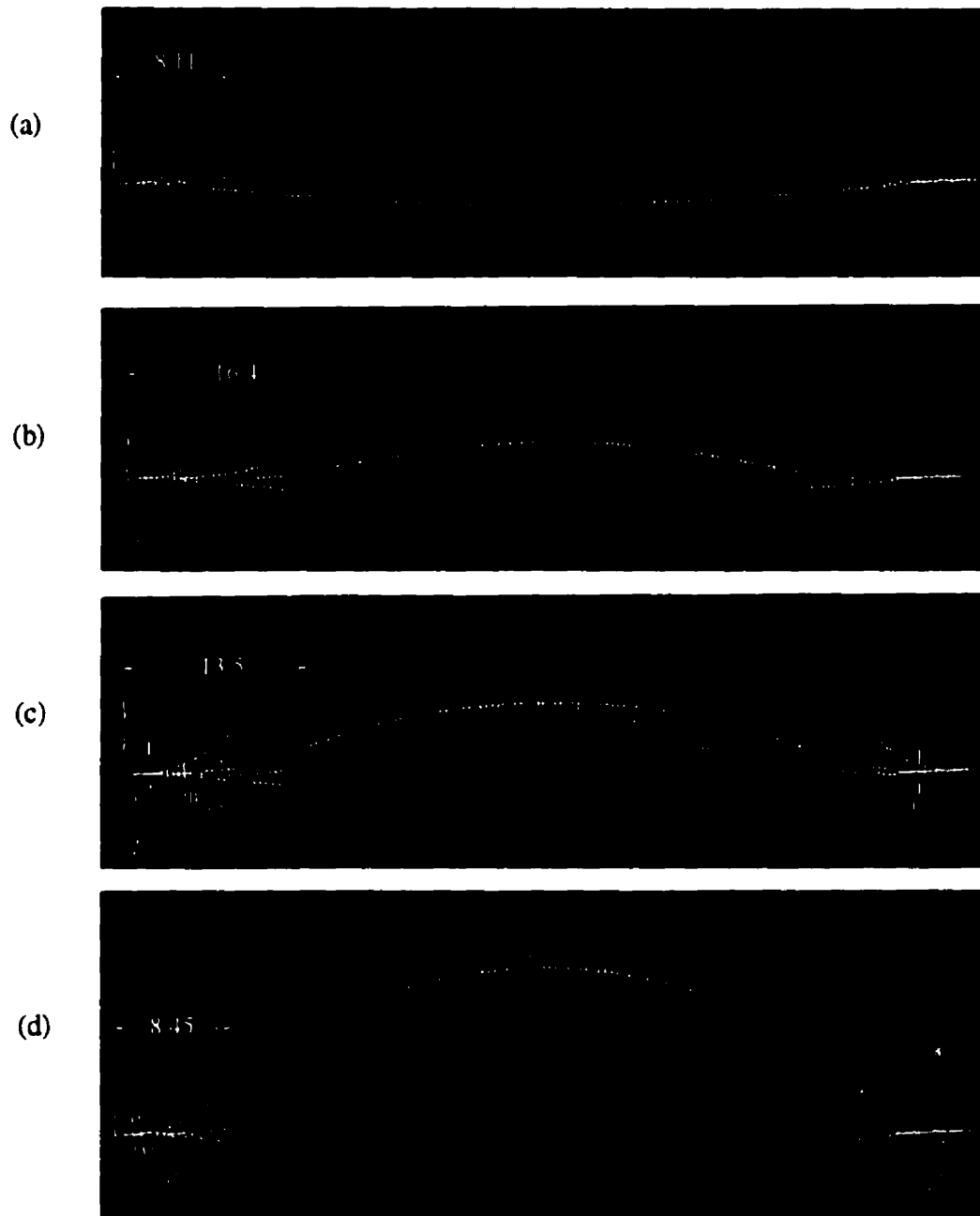


Fig. 6.14 Curvature distribution at different times: (a) $t=0.0$ ms deformation due to heating; (b) $t=20$ ms; (c) $t=40$ ms; (d) $t=160$ ms. Distance from the edge to the inflection point is indicated.

As seen in the previous figures, the heating process itself generates some thermal deformation, called warpage or warpage, even though there is no pressure difference on the two sides of the polymer sheet. When the temperature of the polymer is elevated to its glass transition temperature, the polymer will change from a solid, brittle glassy state to a rubbery state (capable of flow). Under the combination of forces caused by residual stress, thermal expansion stress, and the material's own weight, the polymer sample will deform into a form no longer flat. The thermal warpage is dependent on the material's own thermal expansion properties and initial residual stress conditions. For the ABS material, the heating warpage is relatively small and uniform. As shown in Fig. 6.15, the measured heating warpage is approximately 1.69 mm for the maximum. This warpage plays a role in the following inflation deformation. As shown in Fig. 6.14, the heating warpage and the inflation deformation co-exist for a short period. For the HIPS and HDPE materials, the heating warpage is more serious, and plays a dominant role for the following inflation deformation, as we will see later.



Fig. 6.15 Warpage due to the heating of the ABS material.

6.3.3 Temperature Effect

In this section, the effect of temperature on the bubble inflation test is studied. Three ABS polymer sheets are heated to three different temperatures—130 °C, 150 °C, and 180 °C, respectively. Then the sheets are blown up by inflating the compressed air at a rate of 3.0 liter/s. The bubble profiles before and 60 ms after the inflation are displayed in Fig. 6.16 for different temperatures.

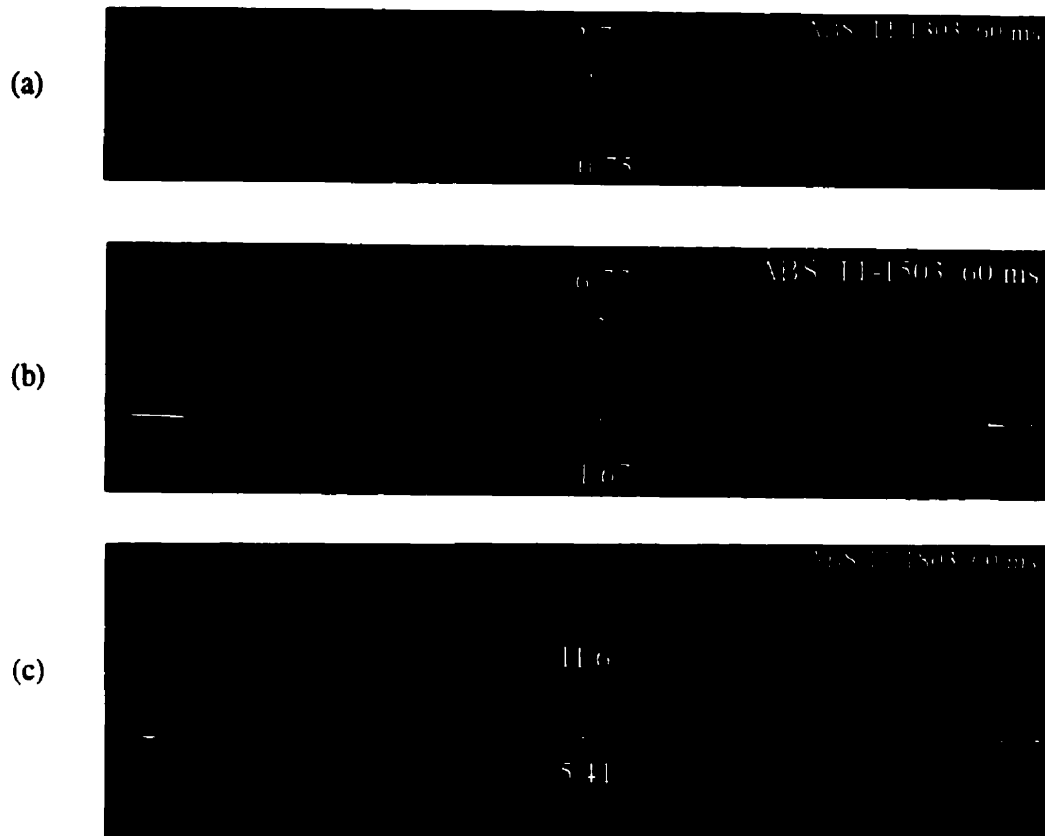


Fig. 6.16 Temperature effect on the bubble inflation tests for ABS material: (a) 130 Celsius; (b) 150 Celsius; (c) 180 Celsius. All at 3.0 liter/s airflow rate.

As shown in Fig. 6.16, the higher the temperature is, the softer the specimen will be. Due to the thermal expansion and specimen's own weight, the heating warpage gets worse with the increase of temperature. At 130 °C, the maximum warpage is approximately 0.75 mm. This number is increased to 1.67 mm for 150°C and 5.41 mm for 180°C. On the other hand, the bubble height at 60 ms after inflation is also increasing with the promotion of the temperature—2.7 mm for 130°C, 6.77 mm for 150°C, and 11.6 mm for 180°C. The pressure difference at 60 ms after inflation is also recorded for three tests— 8.27×10^{-3} MPa for 130°C test, 8.48×10^{-3} MPa for 150°C test, and 8.27×10^{-3} MPa for

180°C test. At this moment (60 ms after inflation), the pressure difference is almost the same for these three tests at different temperatures, though the bubble height is quite different. Clearly, the temperature is a very important factor in bubble inflation tests.

6.3.4 Airflow Rate Effect

As the inflation medium, the compressed air is also important in the bubble inflation tests. Different strain rates of the bubble deformation are generated by different airflow rates. Three airflow rates are employed in our tests—3.0, 5.0, and 8.0 *liter/s*. In this section, the airflow rate effect on the ABS material at 150°C will be studied.

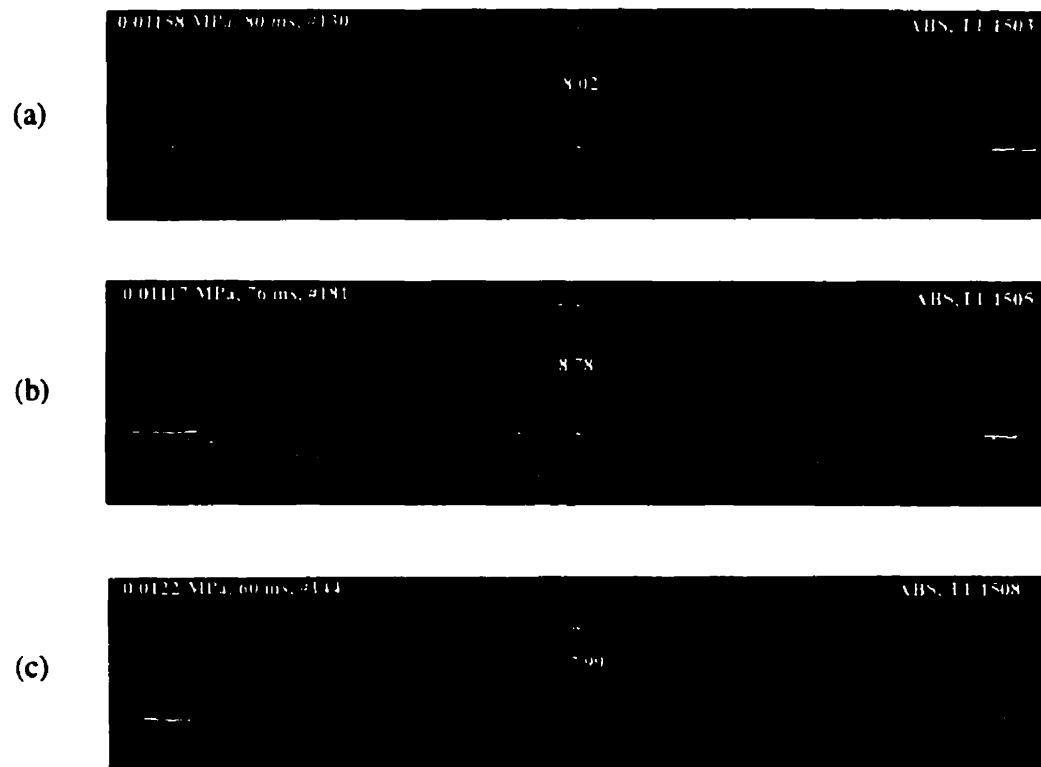


Fig. 6.17 Airflow rate effect on the ABS material at 150 Celsius:
(a) 3.0 *liter/s*; (b) 5.0 *liter/s*; (c) 8.0 *liter/s*.

As shown in Fig. 6.17 (a), the airflow rate is 3.0 *liter/s*. At the moment 80 ms after introducing the compressed air into the pressure chamber, the bubble height is

approximately 8.02 mm and the pressure difference is close to 11.58×10^{-3} MPa. If the airflow rate is changed to 5.0 *liter/s* and repeat the same test, the bubble height goes to 8.78 mm when the pressure difference is 11.79×10^{-3} MPa, as shown in Fig. 6.17 (b). The pressure difference spent less time (76 ms) to reach approximately the same level as the previous test. Finally the airflow rate is increased to 8.0 *liter/s* and the same test is repeated. The bubble height is approximately 7.99 mm with the pressure difference at 12.2×10^{-3} MPa. This time the pressure difference reached this level in 60 ms after inflation. Therefore, the higher the airflow rate is, the faster the bubble grows, and the faster the pressure difference increases. If the rate dependency of the material were significant, it would be expected to observe a difference in the bubble height at the same nominal pressure for different airflow rates. However, the difference in the bubble height does not vary consistently with the airflow rates tested. From 3.0 *liter/s* to 8.0 *liter/s*, the airflow rate is changed by a factor of 2.7 only. It is expected that rate dependency will become non-negligible only when the airflow rate is changed by a factor of over 10. On the other hand, when considering a small height difference, a number of other factors play a role, such as the thermal warping variation, the temperature variation, and the airflow rate variation in different tests, which may be more significant than the rate dependency over this small range of flow rates.

6.3.5 Thermoformability

In the research, three different polymeric materials have been tested—HIPS, ABS, and HDPE. The measured data shows that these three materials have different behaviors during the heating and the succeeding biaxial deformation. In this section the thermoformability of these three materials is studied.

The profiles of the bubble at time zero and 120 ms are shown in Fig. 6.18 for three materials respectively. All three tests are carried out at 130 °C and with the airflow rate at 3.0 *liter/s*. For the ABS, the maximum warping due to heating is approximately 0.747 mm, and the bubble height at time 120 ms is around 4.93 mm. At this moment the measured pressure difference is approximately 16.96×10^{-3} MPa. The HDPE specimen goes through a relatively violent warping deformation when the temperature is elevated

from room temperature to 130 °C. As shown in Fig. 6.18 (b), the central part of the circular specimen moves upward to form a convex area with the height of approximately 4.24 mm for the maximum. In the meantime, other portion moves downward as the usual warping of the other two materials. At this instant, there is no pressure difference on both sides to support the polymer sheet. In the succeeding inflation, the polymer sheet has to recover from the warping first. So, some areas of the sheet deform a lot comparing to the central portion, during the same period of time. At time 120 ms, the bubble shape has fully recovered from the warping and the pole reaches approximately 6.27 mm high, however the shape is not as spherical as whose with relatively uniform warping. The pressure difference is around 17.99×10^{-3} MPa at time 120 ms. Finally, the HIPS sheet has a usual warping recorded at 1.75 mm downward for the maximum. At time 120 ms, the relatively bigger bubble has been formed with the pole at 10.1 mm high and the pressure difference of 16.96×10^{-3} MPa, which is as same as the ABS specimen.

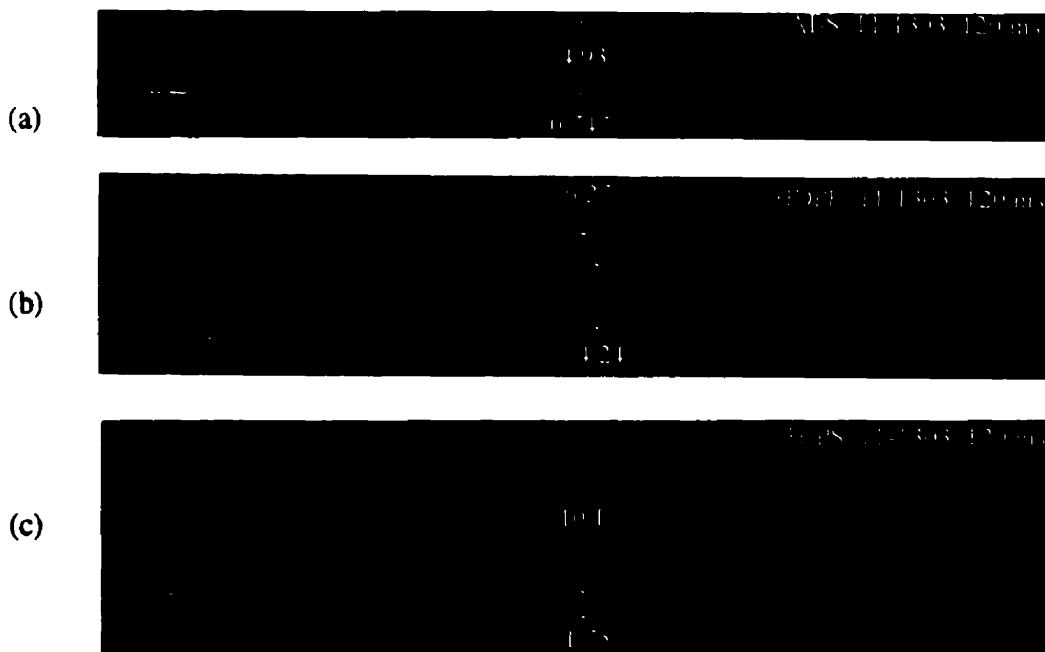


Fig. 6.18 Bubble profiles at $t=0$ and $t=120$ ms: (a) ABS; (b) HDPE; (c) HIPS. Temperature at 130 Celsius and airflow rate at 3.0 liter/s.

Since the thickness of the ABS specimen is 1.5 mm and only 1.0 mm for the HIPS and HDPE materials, it is difficult to draw any conclusion for the ABS material directly. However, the HIPS is easier to form a bubble than the HDPE. Moreover, the HDPE is most likely to have some violent warping deformation during the heating process.

6.3.6 Deformation in Heating Process

Due to the use of compressed air as inflation medium in our tests, there is no support for the sample during the heating and prior to the inflation process. It is reasonable for the specimen to deform due to the combined effect of thermal expansion and the material's own weight. As shown in the measured data, different polymeric materials have different warping deformations during the heating process. For the ABS and HIPS, the warping is relatively uniform, and increases with the temperature. The warping of the HDPE specimen is more profound and turns into a more complex shape. In addition, the warping plays a role in the succeeding inflation deformation. In the cases of the ABS and HIPS, much of the deformation in the early inflation stage will turn out to correct the warping. For the HDPE, the complex warping shape will play a dominant role in the succeeding inflation deformation, and usually ends up causing a non-spherical bubble.

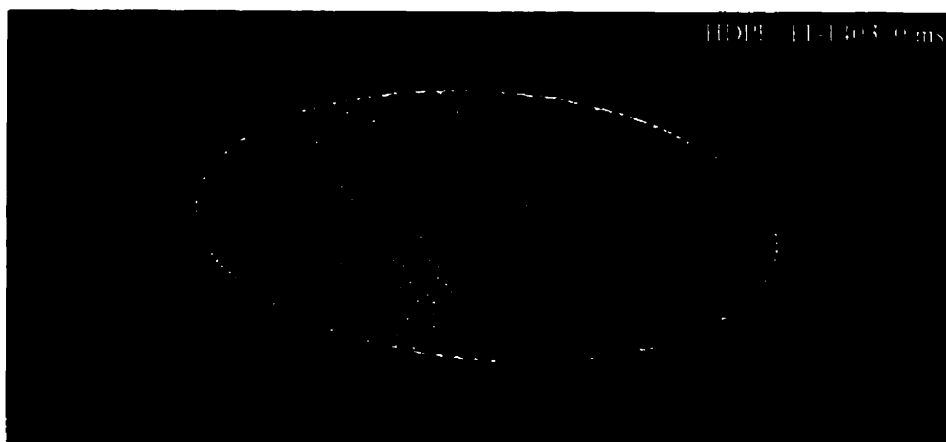


Fig. 6.19 Warping of the HDPE specimen at 140 Celsius before inflation.

As shown in Fig. 6.19, some areas on the HDPE specimen have a positive warping and others have negative one compared to the original shape before the heating. The profound warping shape is shown more clearly in Fig. 6.20 in a cross-sectional form with the deformation varying from -1.05 mm to $+1.67$ mm.

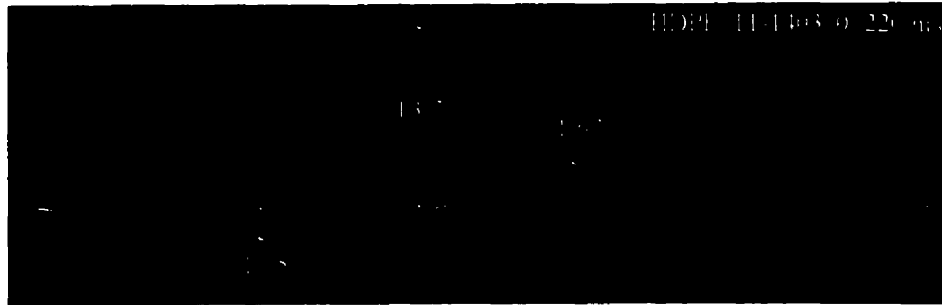


Fig. 6.20 Bubble profiles of HDPE at $t=0$ ms and $t=220$ ms.
With 3.0 liter/s airflow rate and 140 Celsius.

The bubble shape at $t=220$ ms is displayed in Fig. 6.21 with the pole at 13.7 mm high. A cross-sectional view is also available in Fig. 6.20. The bubble shape at this moment is more like a cone instead of a sphere. The curvature distribution of a cross-sectional line at $t=0$ ms and $t=220$ ms is displayed in Fig. 6.22. The results obtained are clearly more complex than those obtained for ABS, which is shown in Fig. 6.14.



Fig. 6.21 Wireframe display of the bubble shape of a HDPE sheet at $t=220$ ms with 3.0 liter/s airflow rate and 140 Celsius.

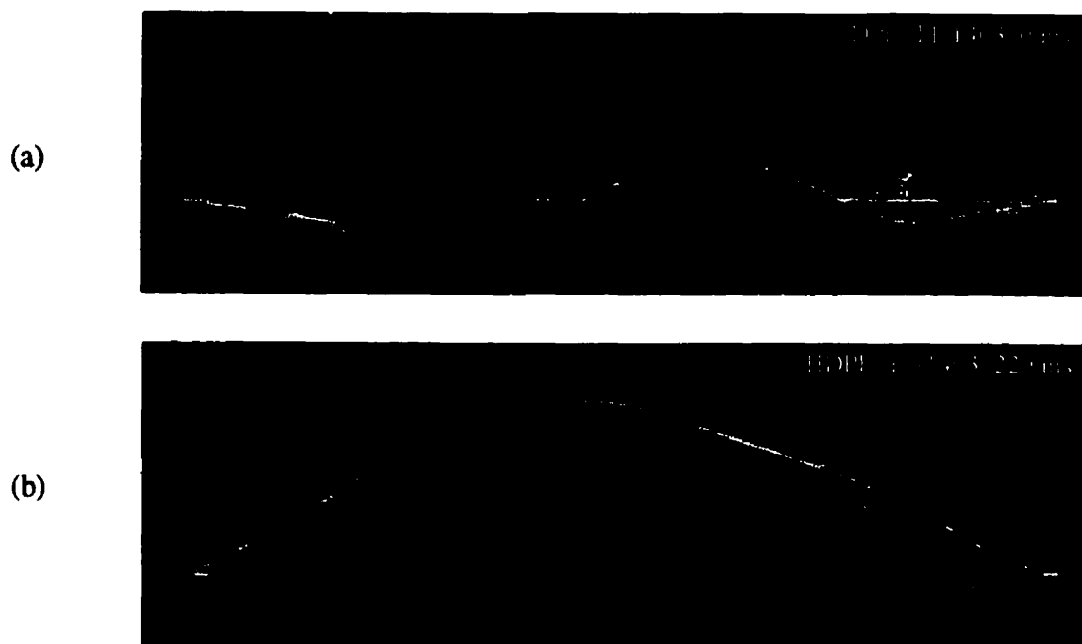


Fig. 6.22 Curvature distribution of cross-sectional lines of a HDPE bubble at (a) $t=0$ & (b) $t=220$ ms with 3.0 liter/s airflow rate and 140 Celsius.

By looking at Fig. 6.22, it is clear that the shape is not spherical even though the h/a ratio is only 0.43. Therefore, the warping during the heating process plays a very important role in the succeeding inflation for some materials such as the HDPE. This fact should be addressed when using the bubble inflation technique in the characterization of material properties.

6.4 Summary

The bubble inflation technique is a very useful method for polymer characterization, especially under biaxial stretching. Some basic assumptions are set initially for the analysis, such as uniform deformation and spherical shape. Due to a lack of precise bubble shape data, it has previously been impossible to assess how accurate this method is.

The experimentally measured data presented in this chapter shows that the deformation is not uniform, and the bubble shape is not spherical. The spherical shape assumption used

by the related work will create errors in their results. The effects of different factors, such as the temperature and the airflow rate, are also studied. In order to obtain material properties, a proposed method utilizing a FEM model to account for the imperfections in the testing, such as the temperature gradient, is considered in the following section.

Digitization of a bubble inflation surface of a circular polymer sheet into an array of points with known *xyz* coordinates has not been done previously. Thus, the experimental results presented in this chapter are very useful as a source of verification and comparison for the related work.

CHAPTER 7

FINITE-ELEMENT ANALYSIS ON CIRCULAR MEMBRANE INFLATION

7.1 Introduction

Many polymeric materials exhibit rubber-like behavior, i.e., the deformation remains elastic up to large strain values, particularly when the temperature is over its glass transition temperature. Although, the stress-strain behavior of these polymeric materials is elastic, it is usually highly nonlinear. This type of material behavior can be described using hyperelasticity theories. The constitutive equation for hyperelastic material is described in terms of a strain energy potential function rather than by assuming a linear relation, a priori, as is done for most engineering materials. The strain energy potential function defines the strain energy stored in the material per unit of reference volume as a function of the strain at that point in the material. There are several forms of strain energy potentials available in the literature, including the polynomial form, the Mooney-Rivlin form, and the Ogden form. If the material is incompressible, the polynomial form of the strain energy potential function, which is most commonly used, has a form:

$$U = \sum_{i+j=1}^N C_{ij} (\bar{I}_1 - 3)^i (\bar{I}_2 - 3)^j \quad (7.1-1)$$

where U is the strain energy potential; \bar{I}_1 & \bar{I}_2 are the first and second invariants of the left Green-Cauchy deformation tensor, C_{ij} are material parameters, which are functions of temperature, and N is the order of the polynomial utilized. The C_{ij} parameters describe the shear behavior of the material. If the number of terms, N , is one and since the material is assumed incompressible, Eq. 7.1-1 has a simple form, which is commonly referred to as the Mooney-Rivlin material model.

$$U = C_{10}(\bar{I}_1 - 3) + C_{01}(\bar{I}_2 - 3) \quad (7.1-2)$$

The invariants \bar{I}_1 and \bar{I}_2 can be written in terms of the principal stretch ratios by:

$$\begin{aligned} \bar{I}_1 &= \lambda_1^2 + \lambda_2^2 + \lambda_3^2 \\ \bar{I}_2 &= \lambda_1^2 \lambda_2^2 + \lambda_2^2 \lambda_3^2 + \lambda_3^2 \lambda_1^2 \end{aligned} \quad (7.1-3)$$

where λ_1 , λ_2 and λ_3 are the stretch ratios in the meridian, circumferential and normal directions, respectively. If the bubble is assumed in spherical shape and the deformation is uniform and incompressible, the stretch ratios can be defined as:

$$\begin{cases} \lambda_1 = \frac{\alpha \cdot R}{a} \\ \lambda_2 = \frac{r}{q} \\ \lambda_1 \cdot \lambda_2 \cdot \lambda_3 = 1 \end{cases} \quad (7.1-4)$$

As shown in Fig. 6.2, the angle α and R are defined by Eq. 6.1-1 and Eq. 6.1-6, respectively. The distance r and q are shown in Fig. 6.2. Therefore, the stretch ratios can be calculated from the bubble height when the spherical assumption remains.

Based on the membrane theory (Yang & Feng 1970), the equilibrium equations in the meridian-circumferential and the normal directions of the deformed membrane are:

$$\begin{cases} \frac{dT_1}{dq} + \frac{1}{q}(T_1 - T_2) = 0 \\ K_1 T_1 + K_2 T_2 = P \end{cases} \quad (7.1-5)$$

where T_1 and T_2 are the stress resultants with dimension of force per unit edge length of the membrane; K_1 and K_2 are the principal curvatures; P is the inflating pressure in the

normal direction of the deformed membrane; q is the distance from the point on the membrane to the axis which is passing through the center of the circular membrane and perpendicular to the original membrane plane. In the context of membrane theory, the stress resultants T_1 and T_2 can be expressed in terms of the strain energy potential:

$$T_i = \lambda_i \cdot \frac{\partial U}{\partial \lambda_i} \quad (7.1-6)$$

where U is the strain energy potential and $i=1,2$. The non-linear problem defined by equations (7.1-2) through (7.1-6) can be solved subject to the boundary conditions by using numerical methods, such as the Runge-Kutta method. This is the closed-form solution for the circular membrane inflation—given any pressure P , the bubble height h can be calculated for different material models. However, to do so it is necessary to assume that the bubble shape is spherical.

By reviewing the experimental data presented in the previous chapter, it is observed that the bubble shape is non-spherical due to the non-uniform deformation. In addition, the thermo warping during the heating plays a role in the succeeding inflation and it is not negligible at least for HDPE material. Therefore, applying the above closed-form solution for the bubble inflation problems will lead to errors.

In order to account for the non-uniform deformation observed in our experimental data, the finite-element method is used here to model the circular membrane inflation including some imperfections. In the first section, a finite-element model will be outlined, which covers the mesh generation, element type and material model. In the second section, the finite-element analysis results under idealized conditions will be presented. The purpose is to demonstrate how significant the error is by ignoring the non-uniformity of the temperature distribution. Finally, in order to better simulate the actual test conditions, a non-uniform temperature distribution and the prestress condition generated in the heating process are included in the finite-element analysis.

The commercially available finite-element analysis software package—ABAQUS v.5.8 by Hibbit, Karlsson, and Sorensen Inc.—is used in this analysis.

7.2 Finite-element Model

7.2.1 Geometry and Mesh Generation

The succeeding finite-element analysis is focused on the ABS material. Since the specimen is circular in shape, axisymmetric conditions are assumed here. The coordinate system and the mesh used for the circular membrane are shown in Fig. 7.1. Due to symmetry, only the material from the center to one clamped edge is considered in the FEM simulation. The radius of the circular membrane is 31.75 mm, and its thickness is 1.57 mm. Twenty axisymmetric continuum elements are used, and the elements have an aspect ratio of approximately 1.

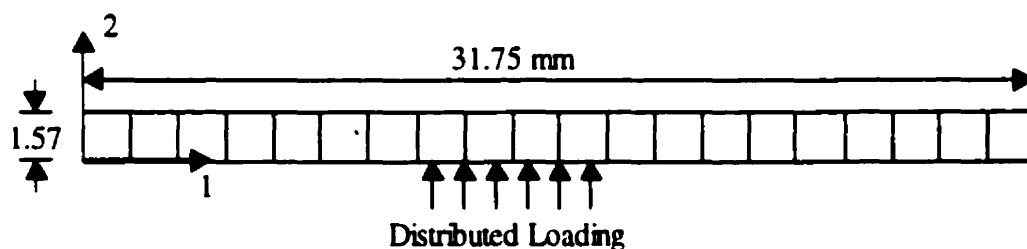


Fig. 7.1 Finite-element mesh for circular ABS membranes.

7.2.2 Element Model

As shown in Fig. 7.1, twenty continuum elements are used. These elements are 8-node, second-order, mixed formulation, hybrid elements since the polymeric material is treated as incompressible. The element formulation is described in the ABAQUS Theory Manual (Hibbit, Karlsson, and Sorensen Inc. 1998). The origin of the global coordinate system is placed at node 1 located in the center of the specimen. The global 1-axis lies along the length of the circular membrane starting from node 1 toward the fixed edge, and the global 2-axis lies in the thickness direction from node 1 upward.

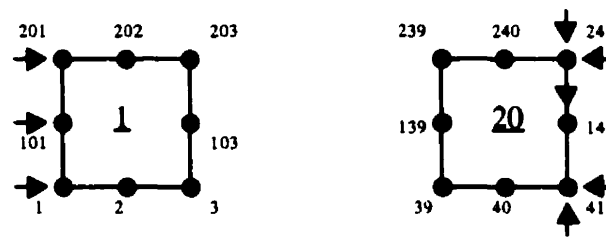


Fig. 7.2 Element type (CAX8H) and boundary condition.

As shown in Fig. 7.2, element 1 is close to the center of the circular specimen and element 20 is close to the fixed circumference. Regarding the boundary condition, node 41 and node 241 are fixed in both directions. Node 141 is free to move in the 1-axis direction, but constrained in the 2-axis direction. The displacements in the 1-axis direction for the nodes on the central line (node 1, 101, and 201) are zero since the deformation is symmetric. The boundary condition at Node 141 allows the material to be drawn inward during the inflation even though it could be small since the central region material is very soft and the material close to the clamped edge is very stiff due to the temperature gradient. The loading consists of a uniform pressure applied to the bottom surface of the specimen in the 2-axis direction. The modified Riks method is used in the FEM simulation since the loading is proportional and because the solution may exhibit instability. For more about the modified Riks method, please see Crisfield's paper (1981). A pressure magnitude of 0.09 MPa is specified: this magnitude is somewhat arbitrary since the Riks method is chosen. The actual pressure magnitude beyond the end of the first increment will be decided by Riks method.

In the analysis, the Mooney-Rivlin material model is used. Different values for the material constants, C_{10} and C_{01} , are selected for different temperatures. The objective is to match the inflation shapes obtained from finite-element analysis to those measured experimentally.

The following assumptions have been made for modeling the inflation of ABS material:

- The material behavior is hyperelastic (Mooney-Rivlin);
- The material behavior is isotropic;
- The material is incompressible.

7.3 Finite-element Analysis—Idealized Conditions

In order to perform this initial analysis, two additional idealized conditions have been added:

- The initial temperature distribution is uniform;
- Thermo-warping plays no role in the inflation.

Most of the research papers published have considered that the inflation obeys these two assumptions since they can easily lead to a uniform deformation and a pure spherical bubble shape.

7.3.1 Finite-element Simulation for ABS Inflation Test T1-1503

The following analysis is for the ABS material with a nominal temperature of 150°C and the airflow rate of 3.0 *liter/sec*. The bubble inflation was measured by the proposed optical measurement system. Therefore, the bubble shape as a function of time and pressure is known from the measurement. Different values for C_{10} and C_{01} are input into the ABAQUS software to match the simulation result with what was measured experimentally. Under the current conditions, the best agreement is found when $C_{10} = 0.4$ MPa and $C_{01} = 0.008$ MPa, after several iterations. The input file for the ABAQUS is listed in Appendix B.

The simulated bubble shape at various inflation stages is shown in Fig. 7.3. The bubble shape in this figure is more spherical than what was measured experimentally. The simulated shape is compared with the shape measured experimentally in Fig. 7.4 and Fig.7.5 for two different pressure values.

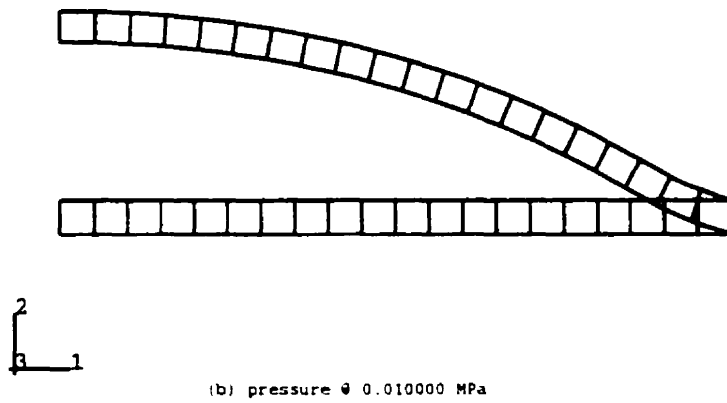
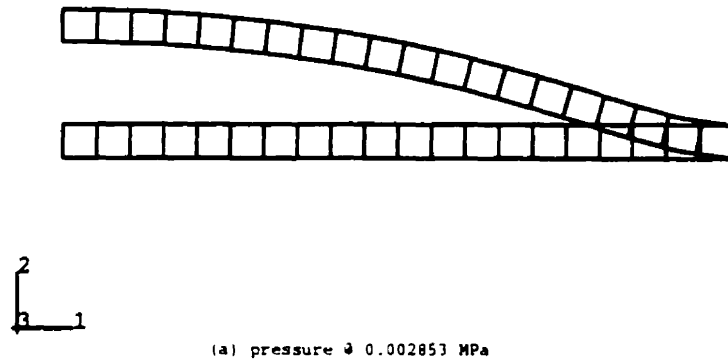


Fig. 7.3 The ABAQUS simulation results: (a) pressure= 0.2852×10^4 Pa;
(b) pressure= 1.0000×10^4 Pa.

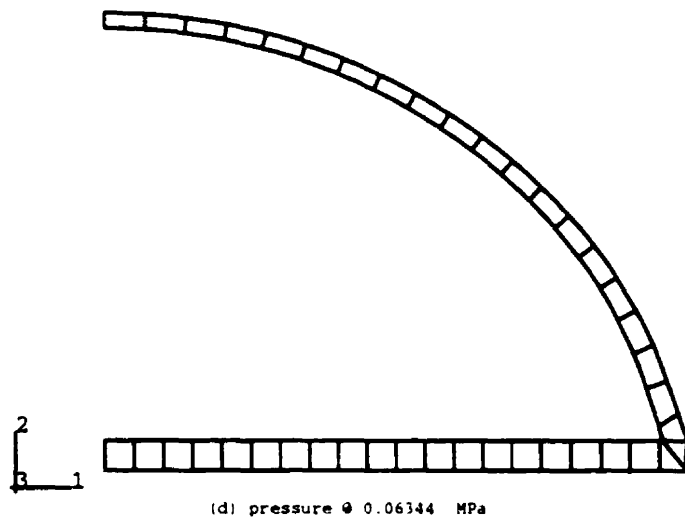
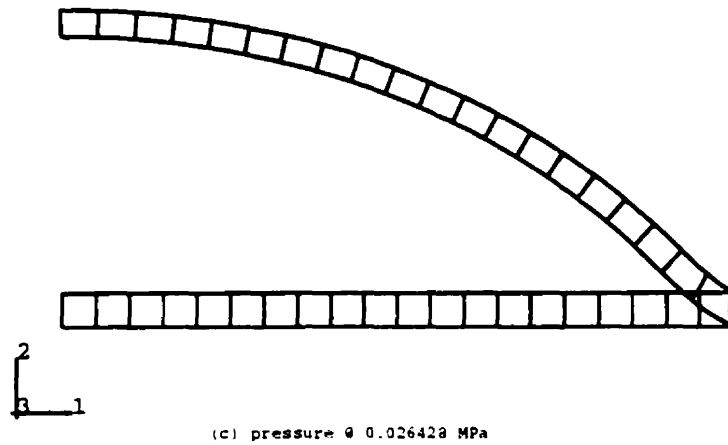


Fig. 7.3 (Cont.) The ABAQUS simulation results: (c) pressure= 2.6428×10^4 Pa; (d) pressure= 6.344×10^4 Pa.

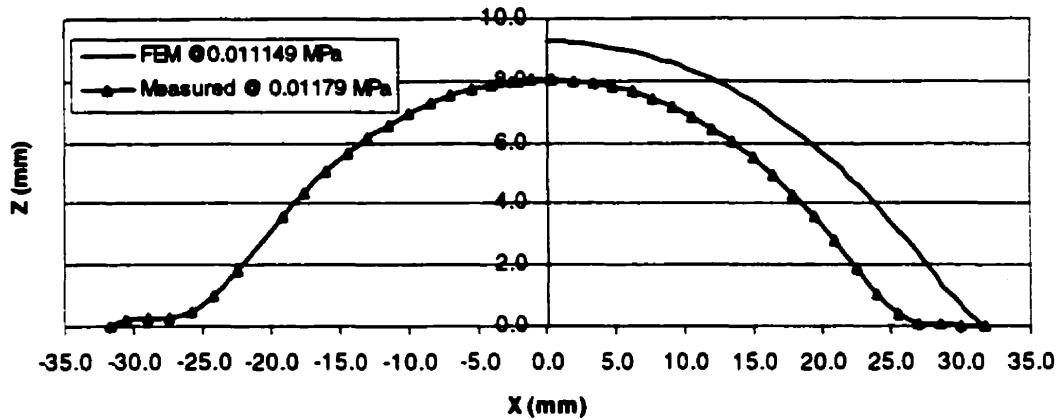


Fig. 7.4 Bubble shape comparison @ 0.011 MPa.

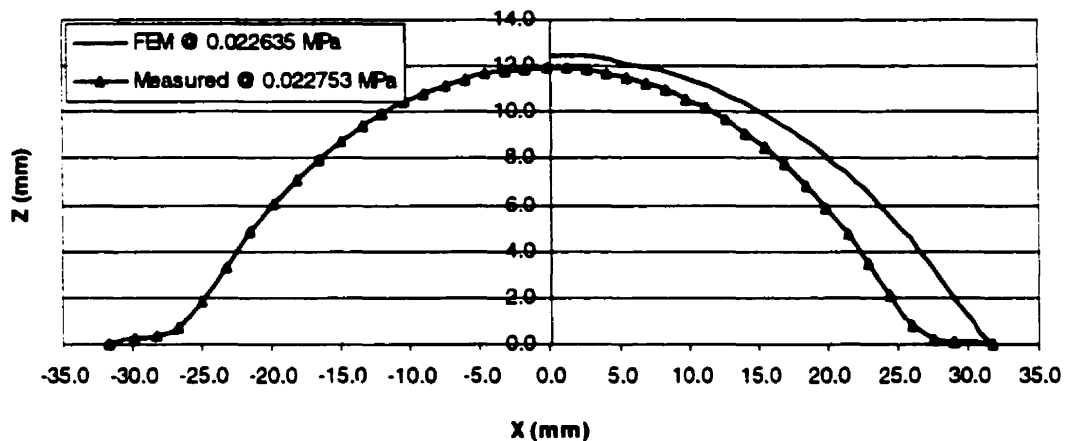


Fig. 7.5 Bubble shape comparison @ 0.023 MPa.

As shown in Fig. 7.5, the FEM simulation predicts a larger bubble shape at the beginning of the inflation. With the increase of pressure, the difference between the bubble height predicted by the FEM and what was measured experimentally is decreasing. At one point, the bubble height predicted by the FEM and what was measured experimentally are almost the same. Meanwhile, the difference in the bubble shape is more pronounced close to the circumference. From this point on, the bubble height predicted by the FEM will be smaller than what was measured experimentally. This can be shown more clearly in the height vs. pressure curve in Fig. 7.6.

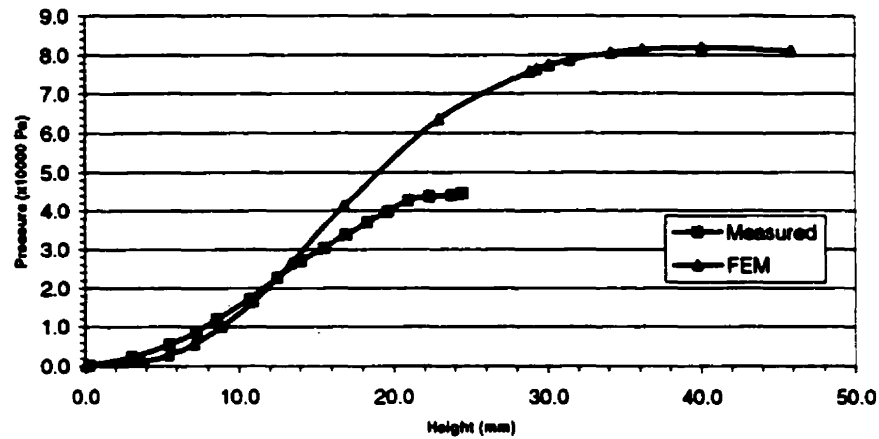


Fig. 7.6 Bubble height vs. pressure curve of ABS material considering uniform temperature distribution.

Fig. 7.6 shows that the pressure simulated by the FEM will continue to grow even after the experiment shows the pressure to level off, although in much of the range the two curves are 'close' to each other. If the material constants are characterized by this method, the obtained material constants could represent a stiffer polymeric material, which has a similar response in the measured pressure range. Therefore, it is difficult to say thus that the FEM simulation agrees with experiments very well. This may have something to do with the assumptions we made.

It should be noted that the experiments start from room temperature, and the specimen's final temperature may be as high as 150°C for certain tests. The polymer membrane is clamped between two aluminum plates and the lower plate is connected to the high-pressure chamber that has also aluminum plates as its walls. Since the thermal conductivity of the aluminum material is approximately 100 times of that of the ABS material, and the infrared heaters are focused on the specimen only, a temperature gradient exists in the experiments. Therefore, considering the temperature to be uniform is a very significant assumption in this kind of test.

On the other hand, the polymeric material constants are very sensitive to the temperature, and any temperature change will cause a significant change in the material constants,

particularly near the glass transition temperature. The assumption of uniform temperature means that incorrect material constants are used for some regions of the specimen by ignoring the temperature gradient. In addition, the temperature gradient can certainly lead to a bubble shape, which is not spherical. Although there is a region close to the pole, in which the deformation is almost uniform and the shape is very close to a sphere, the bubble height is very much decided by the constraints experienced in the region close to the circumference. Less constraint in these areas will permit more material to participate in the inflation, and result in a much larger bubble under the same pressure. Therefore, one should be very careful in the bubble inflation test if only the bubble height will be measured and an existing temperature gradient in the specimen is ignored.

Another idealization made concerned the thermo-warping during the heating process. In this first analysis, it was assumed that the thermo-warping plays no role in the succeeding inflation, even though we observed it existed in all inflation tests carried out. It is known that a change in temperature will cause stress in a structure if it is not free to expand, and the circular ABS sheet is clamped along its circumference. On the other hand, the ABS material becomes very soft in our tests since the temperature was above its glass transition temperature, which is around 140°C. Therefore, under the combined action of thermal expansion and the material's own weight, it is not reasonable to assume there is no stretching and stress existing in the specimen before the inflation takes off.

Due to these assumptions, this section is called 'under idealized conditions'. In the next section, the FEM analysis will include temperature nonuniformities and thermal warping to improve the accuracy of characterization of polymer constants.

7.4 Finite-element Analysis—General Conditions

The analysis results in the previous section show that the nonuniformities of the temperature distribution and the thermo-warping during the heating are very important in the bubble inflation tests of polymer membranes. In order to determine the material

constants correctly, the FEM model has to include these two factors. To measure the temperature gradient, an infrared camera—ThermoVision 900 made by the AGEMA Infrared Systems AB, Sweden—is used. The measured result is shown in Fig. 7.7. The temperature is relatively uniform in the central region of the membrane, but clearly the temperature is dropping rapidly starting from approximately $2/3$ of the radius. This trend is increasing to where there is a temperature jump in between the polymer and aluminum materials at the clamped edge. The maximum temperature difference from the center to the clamped edge is approximately 40°C , according to the reading from the infrared camera. Fig. 7.8 shows the temperature profile along a line passing through the center of the circular sample. There is a temperature gap of approximately 70°C between the aluminum plate and the polymeric sample at the clamped edge. The first and last points shown in Fig. 7.8 are located on the aluminum plate.

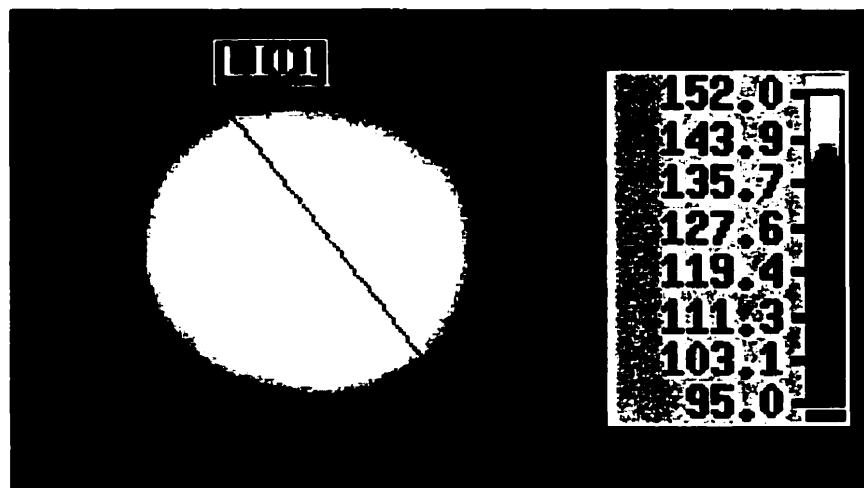


Fig. 7.7 Temperature distribution measured by an infrared camera.

Another observation is about the temperature change during the inflation. Since the inflation usually takes only 1.0 second or less, it is assumed that the temperature distribution is not changing during this period of time. The infrared camera's recording supported this assumption, particularly in the early stage when the measurements were carried out.

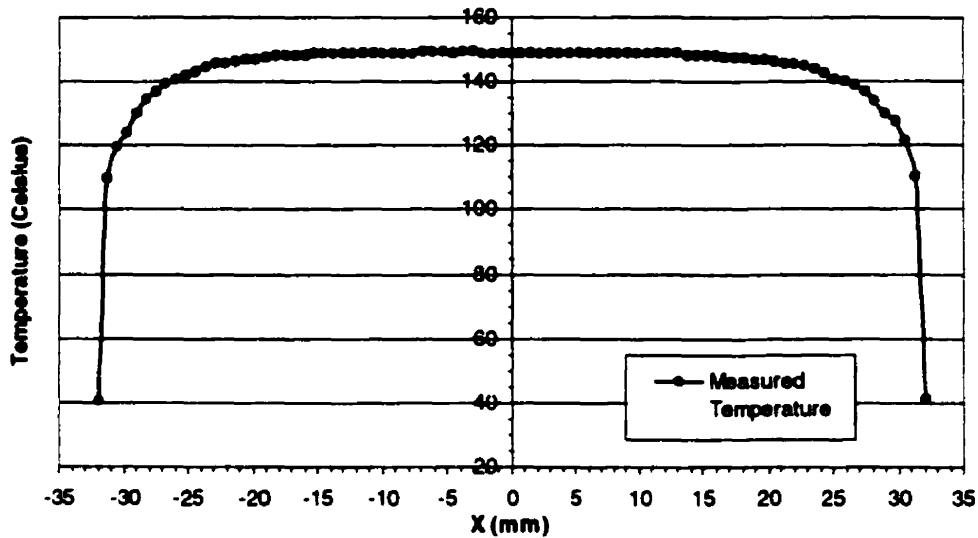


Fig. 7.8 Typical temperature distribution along a line passing through the center.

As shown in Fig. 6.15, the maximum thermo-warping is approximately 1.69 mm in the center of the membrane. This deformation actually creates a small uniform tensile prestress condition in both radial and circumferential directions all over the membrane. In order to approximate the effect of the thermo-warping, a small value (0.06 MPa) is used to represent the prestress as the initial condition in the FEM simulation.

7.4.1 Finite-element Simulation for ABS Inflation Test T1-1503

The same test as that of Section 7.3.1 is simulated. This time the temperature gradient measured by the infrared camera and 0.06 MPa prestress in both radial and circumferential directions are included as the initial conditions in the finite-element analysis. The temperature profile used in the FEM simulation is shown in Fig. 7.9, which is based on Fig. 7.8 after removing the point on the aluminum plate. The material constants C_{10} and C_{01} as functions of temperature are selected in order to let the simulation results match what is measured experimentally. Fig. 7.10 shows the material

constants C_{10} and C_{01} as functions of temperature. The input file for the ABAQUS is included in Appendix C.

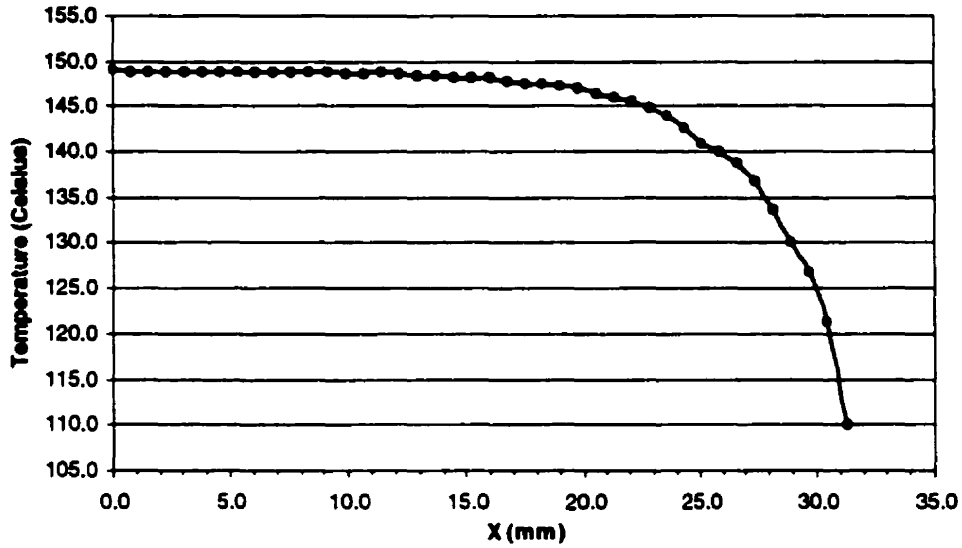


Fig. 7.9 Temperature profile used for FEM simulation. (from the center to the clamped edge)

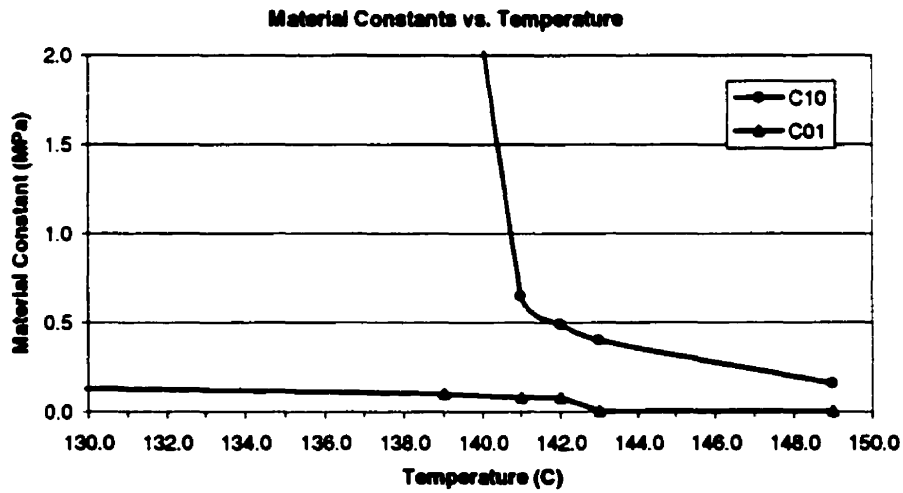


Fig. 7.10 Material constants C_{10} and C_{01} as functions of temperature.

The relationships between the material constants and the temperature, which are shown in Fig. 7.10, can also be written in terms of a set of linear equations:

$$C_{10} = \begin{cases} 194.525 - 1.375T & (T = 139 - 141^\circ\text{C}) \\ 23.21 - 0.16T & (T = 141 - 142^\circ\text{C}) \\ 7.184 - 0.047T & (T = 142 - 149^\circ\text{C}) \end{cases} \quad (7.4-1)$$

$$C_{01} = \begin{cases} 1.02667 - 0.00667T & (T = 139 - 142^\circ\text{C}) \\ 1.6623 - 0.011142T & (T = 142 - 149^\circ\text{C}) \end{cases}$$

where T is the temperature in Celsius, and the unit of C_{10} and C_{01} are MPa.

As shown in Fig. 7.9, the temperature drops below the material's glass transition temperature ($T_g=141^\circ\text{C}$) at the location approximately 26.0 mm from the center. That means the ABS material inside a radius of 26.0 mm is in the rubbery state and capable of flow. While from $r=26.0$ to 31.75 mm, the material is still in the glassy state—solid and brittle. That is the reason why little deformation has been found in this region. At temperatures well above T_g , the polymer chains are relatively free to move in cooperative thermal motion to provide conformational rearrangement of the backbone. Therefore, the material behaves in an increasingly rubber-like manner when the temperature increases, but no sudden change in material properties is expected in the rubbery state. When the temperature is below T_g , the motion of these individual polymer chain segments become frozen with only small scale molecular motion remaining, involving individual or small groups of atoms. Therefore, there is a sharp change in material properties at the glass transition. At temperatures well below T_g , the material behaves in an increasingly brittle-like manner, but with no dramatic change. The temperature dependence of the material constants used is consistent with the material behavior.

From Eq. 7.4-1, the values of C_{10} and C_{01} at 149°C are 0.16 MPa and 0.002 MPa, respectively. Compared with the results in the previous section when the temperature

was considered uniform ($C_{I0}=0.4$ MPa and $C_{O1}=0.008$ MPa), it is clear that the difference is significant.

The bubble shapes at various inflation stages, which is simulated by ABAQUS, are shown in Fig. 7.11. Obviously, the bubble shapes in this figure are not spherical. The inflation appears uniform in the region close to the center of the membrane. However, the material close to the clamped edge experiences constraint and less inflation occurs there. Consequently, the bubble height is affected significantly by these regions close to the clamped edge. In addition, the simulation results show that the thickness of the membrane is no longer uniform after the inflation starts. There is little change in the thickness in the regions close to the clamped edge, and the membrane becomes very thin in the central regions. That is why the final burst always happens near the pole. Both the shape and the thickness distribution after the burst match the experimental observation of the membrane.

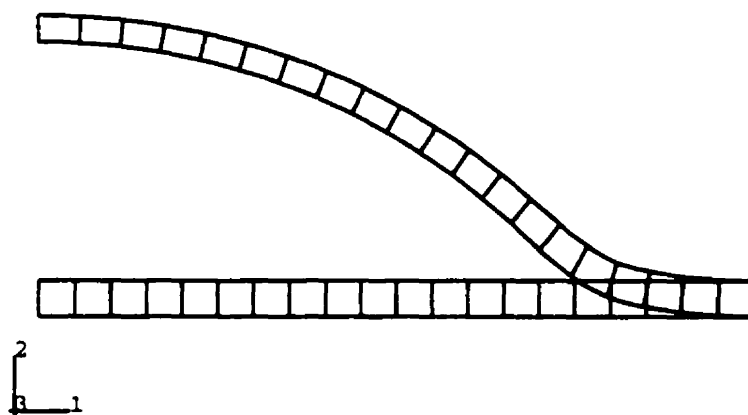
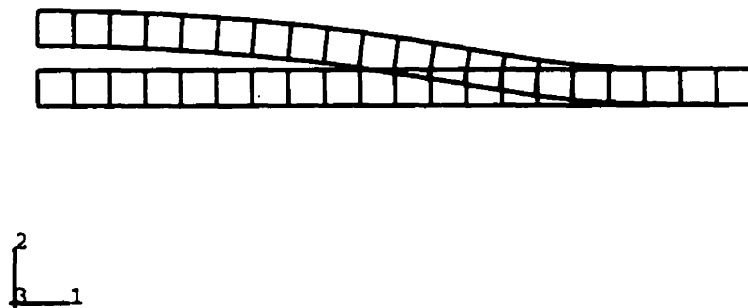


Fig. 7.11 ABAQUS simulation results considering temperature nonuniformity and thermo-warping: (a) pressure= 0.3982×10^4 Pa; (b) pressure= 2.3675×10^4 Pa.

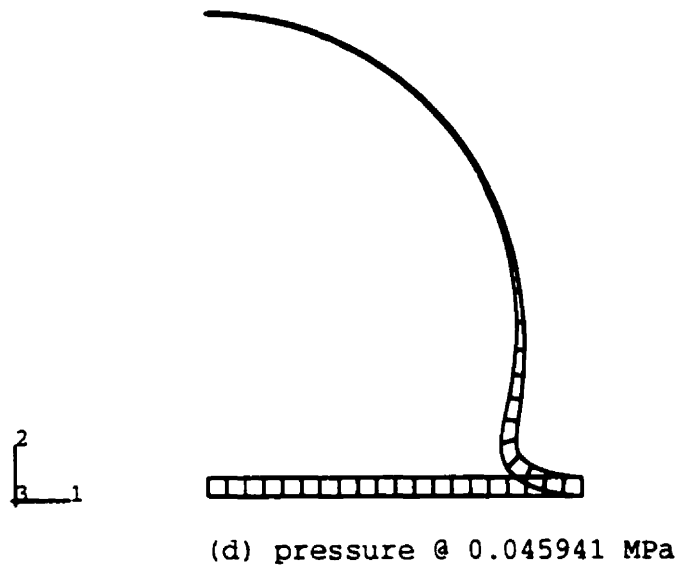
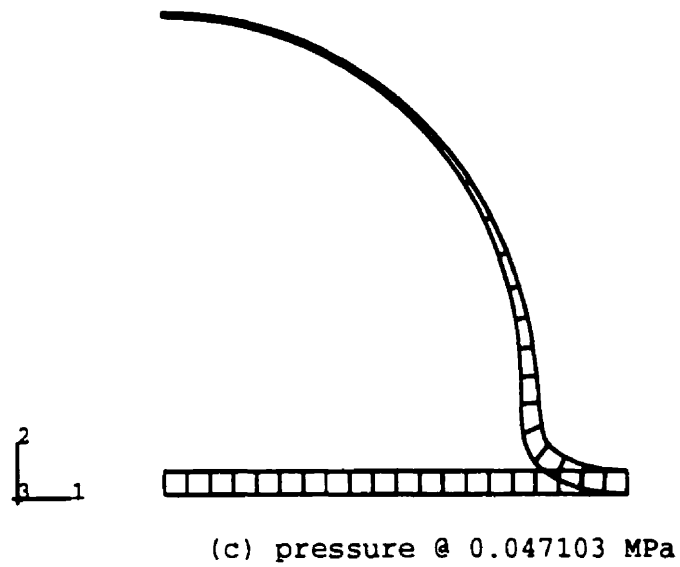


Fig. 7.11 (Cont.) ABAQUS simulation results considering temperature nonuniformity and thermo-warping: (c) pressure= 4.6618×10^4 Pa; (d) pressure= 4.5495×10^4 Pa.

The simulated shape is compared with the shape measured experimentally in Fig. 7.12 for two different pressure values. Comparing with the results in Section 7.3.1, the agreement between the finite-element simulation and what was measured experimentally is very much improved. This agreement can also be seen in the height vs. pressure curve of Fig. 7.13.

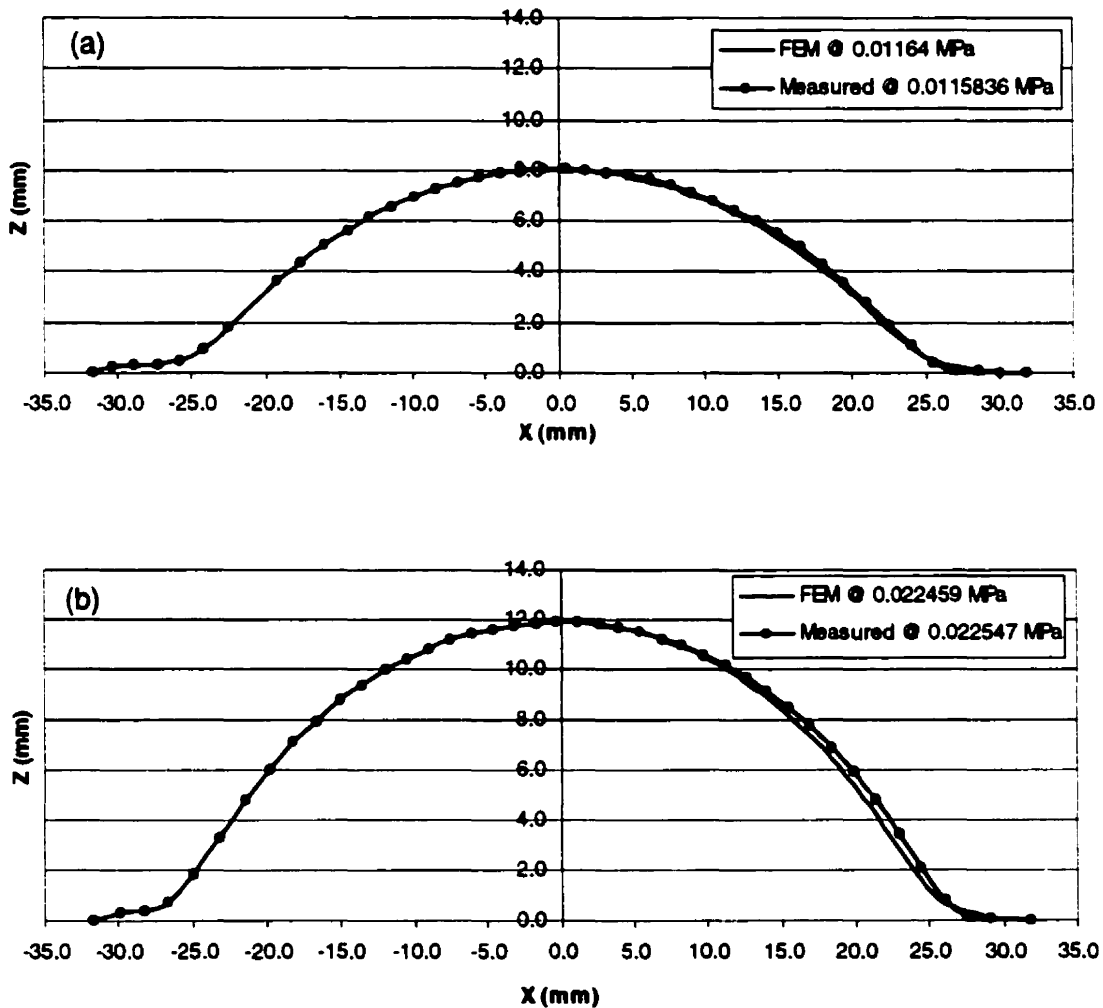


Fig. 7.12 Bubble shape comparison: (a) pressure=0.011 MPa; (b) pressure=0.022 MPa. (Considering the thermal warpage and temperature gradient).

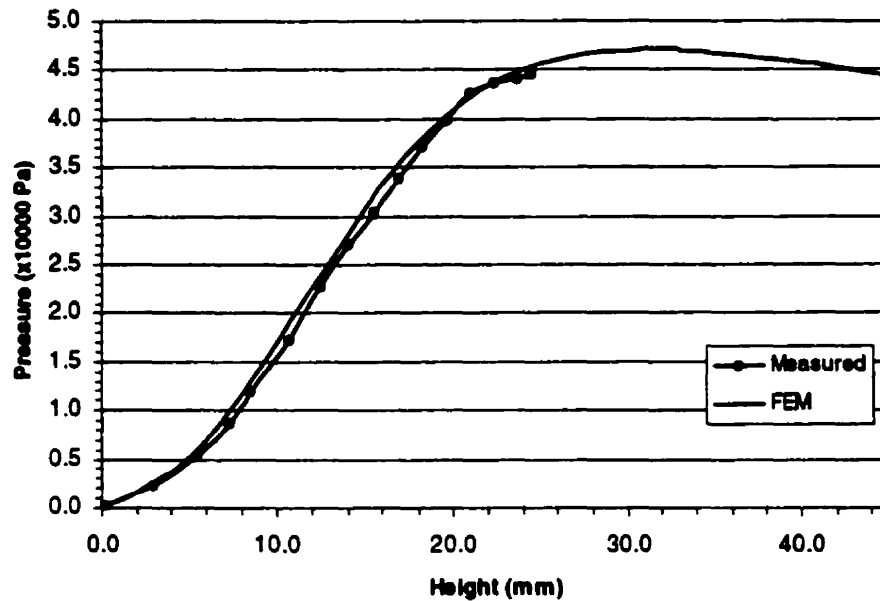


Fig. 7.13 Bubble height vs. pressure curve of ABS material considering nonuniform temperature distribution and thermo-warping.

So far, it has been shown that this method of characterizing temperature-dependent material constants works well reasonably. However, it is worth knowing that this method is not that efficient to find values for the material constants that do not influence shape changes when the material constants themselves are modified. For example, the change of the C_{01} in the Mooney-Rivlin model does not cause significant change in the bubble shape in early inflation stages, so the method is significantly less accurate for determination of this parameter. In addition, this method is not very efficient in finding the values of C_{10} for temperatures significantly below the glass transition temperature. The reason for this is that the deformation of the material below T_g is small. The change in the material properties of the material with its temperature below 130°C does not change the bubble shape considerably. Thus the accuracy would not be expected to be very good. However, In this test, the majority of the material is over 140°C . So the method seems appropriate. Another fact that should be mentioned is that the temperature-dependent material properties characterized in this way can compensate for the discrepancy caused by the material model to a certain extent. For instance, even if the

simple Mooney-Rivlin model may not be very good in representing the material, the overall performance of the material model can be maximized by using the material constants characterized in the manner shown here.

7.5 Summary

A finite-element model is developed to simulate the membrane inflation of polymeric materials. The analysis is performed using a commercially available finite-element software package—ABAQUS version 5.8. The elements are 8-node, second-order, hybrid continuum elements (CAX8H). The material model is the incompressible Mooney-Rivlin model.

First, the nonuniformities of temperature distribution and thermo-warping are ignored. In addition, it is assumed that the temperature remains uniform and unchanged during the inflation. Different values of the material constants are input into the Mooney-Rivlin model in order to match the simulated results with what was measured experimentally. After several iterations, the simulation which has 'the best' agreement with the experimental data is when $C_{10} = 0.4$ MPa and $C_{01} = 0.008$ MPa. However, the simulation results also showed some disagreement, especially in the bubble height vs. pressure curve. In this case, it is quite possible that the material constants have been over-estimated to give a similar response in the tested pressure range. In fact, the polymer represented by these over-estimated material constants shows pressure increasing far beyond the pressure values recorded in the experiments. Therefore, the polymer represented by these over-estimated material constants would not accurately represent what is tested, although it has a similar response in much of the pressure range recorded in the experiments. This gives a warning about the potential errors in the material constants characterized by the bubble inflation technique if the existing temperature nonuniformities and thermo-warping are ignored.

When the temperature gradient and thermo-warping are included in the finite-element analysis, the simulation results give a very close match with what was measured

experimentally. The agreement shows in both the bubble shape as well as the bubble height vs. pressure history. Compared with the material constants determined under the idealized conditions, it is clear there is a significant difference. Therefore, the combination of the optical measurement system and the finite-element method in the membrane inflation tests can provide a new way to characterize the polymeric material constants. Using this method, the material constants can be characterized not as a single value corresponding to a given temperature, but as a function of temperature over the temperature range measured in the experiment.

CHAPTER 8

CONCLUSIONS AND FUTURE DEVELOPMENTS

8.1 Conclusions

In this work, a high-speed optical surface measurement system has been developed. The system is based on the grating projection and Fourier transform method. In addition, a high-speed digital camera is employed to allow measurements of transient surface deformation. The following features make this system distinguishable from other optical measurement technologies:

- (1) Whole-field measurement;
- (2) Setting up a fixed Cartesian coordinate system associated virtually with the sensor head by a developed calibration technique;
- (3) Generating Cartesian coordinates as direct measurement results, which are with respect to the fixed coordinate system in 3D space;
- (4) High-speed measurement—a digital high-speed camera is employed with the maximum frame rate up to 1000 Hz and the shortest exposure time for each frame as low as 50 μ sec;
- (5) Experimentally verified the measurement accuracy;
- (6) Fully automatic data processing.

This is the first time that such an optical measurement system has been developed.

Also for the first time, the inflation of polymer membranes has been measured using whole-field optical methods. The effects of various factors, such as temperature and airflow rate, have been studied. The accurate measurement data also provides a source for further material constant characterization. A potential error caused by the assumption of uniform temperature distribution in the characterization of polymeric material

constants by the bubble inflation technique has been pointed out. As a result, a hyperelastic finite-element model has been used to simulate the bubble inflation of polymer membranes. Finally, for the first time a method of material constant characterization, which is based on a combined finite-element and experimental approach with the ability of incorporating temperature gradients, has been proposed.

8.2 Future Developments

8.2.1 Optical Dynamic Measurement System

All core software that is necessary to calculate xyz coordinates from a deformed grating image has been developed. However, a user-friendly interface is still very desirable.

It is also very necessary to improve the light source. So far, the light intensity can easily support a frame rate of 250 fps, but at frame rates higher than 250 fps and shorter shutter speed, higher light intensity is required.

8.2.2 Membrane Inflation Experiments

The measured results have indicated that nonuniformities in temperature distribution and thermo-warping are very important in determining the inflation response of polymer membranes. Accurate measurement of the temperature distribution is therefore important in bubble inflation tests when using compressed air as the inflation medium. More work needs to be done in order to make accurate temperature measurements. The deformation due to thermo-warping can be measured by the optical system, and the measured results can be used as the initial shape of the polymer membrane, instead of using its original flat shape. By doing so, more accurate finite-element simulation can be expected.

8.2.3 Finite-element Modeling and Material Constant Characterization

The combination of the optical measurement system and the finite-element method that can take account of the nonuniformity of temperature distribution and the thermo-

warping can provide a useful tool in the material constant characterization. If the temperature measurement can be carried out very accurately, the material constants at different temperatures can be determined in one test.

So far, the bubble shape as a function of internal pressure is used to compare with the simulation results provided by the finite-element method to determine the possible material constants. It is a time-consuming process and a more efficient way to do the iteration has to be found. For example, a program can be written to carry out this iteration to find the correct material constants quickly.

The Mooney-Rivlin hyperelastic model has been used in the finite-element simulation. It should be noted that the material constants derived in this way would include the discrepancy caused by the material model. It should be interesting to try other material models, such as the Ogden and higher order polynomial models to study the difference between different material models.

8.2.4 Other Applications

The application of the newly developed optical measurement system has focused on the inflation tests of polymer membranes, particularly for the material constant characterization. Actually, such an optical measurement system is also useful in the inflation tests of other materials including proposed experiments on chopped fiber reinforced polymer membranes. The optical system should be also useful in the bulge experiments of various membrane tissues.

The optical measurement system should be also useful regarding dynamic behavior of structures including the buckling or impact tests of structural components. A preliminary study has been made to measure the elastic buckling of a stiffened box beam during forced vibrations, with good results. A study on a composite plate with bending and twisting coupling has also been carried out (Li & Nemes 1998). Numerous other applications of this system in the field of structural dynamics can be envisioned.

ORIGINALITY AND CONTRIBUTION TO KNOWLEDGE

The original contributions of the present work are two-fold. First, a high-speed optical surface measurement system has been developed. This system has the following features to distinguish itself from other technologies: (1) whole-field measurement which yields Cartesian coordinates as the final data, which are with respect to an absolute coordinate frame; (2) It has the ability to measure rigid body translation and rotation; (3) high-speed measurement—the sampling rate can go up to 1000 Hz, and the shortest exposure time of each frame can be as small as 50 μ sec; (4) fully automatic data processing.

The calibration technique developed in this work makes it possible for the whole-field optical 3D shape measurement system to provide Cartesian coordinates in an absolute way. The whole-field shape measurement of a 3D surface in a dynamic event becomes feasible by using a high-speed digital camera. Furthermore, the evaluation of the measurement accuracy can share the common concepts with what are used in industries. All these factors have made the proposed optical measurement system distinguishable and opened a door for wide-range industrial applications in the near future.

The second contribution is the use of the proposed optical system in the polymer membrane inflation tests. The principal contribution regarding the polymer membrane inflation experiments is that the measured results and the corresponding finite-element analysis reveal the importance of the temperature uniformity and the thermo-warping in the inflation deformation. Serious error could be embedded into the material constants determined from the bubble inflation technique for polymeric materials if there is a temperature gradient existing in the inflation experiments and this temperature nonuniformity is ignored in analysis. As a solution, the optical measurement system combined with the finite-element analysis can be used in the bubble inflation tests to

include the temperature gradient and thermo-warping. The material constants obtained in this way will be more accurate, and multiple values corresponding to different temperatures can be obtained in a single experiment. In addition, the experimental data represents a much-needed contribution to the modeling of the thermoforming process since the reported experimental measurements on the inflation of polymer membranes are few, incomplete and most importantly inaccurate. Whole-field measurements on inflation of circular polymer membrane resulting in *xyz* coordinates are practically nonexistent. Therefore, the experimental data obtained from these measurements will be useful as a source of comparison and verification for related work.

APPENDIX A

SYSTEM CALIBRATION

Eq. 3.3-5 can be transformed into vector forms:

$$(1-k \cdot r^2) \cdot i \cdot [x, y, z, 1] \cdot \begin{bmatrix} r_7 \\ r_8 \\ r_9 \\ t_3 \end{bmatrix} = [x, y, z, 1] \cdot \begin{bmatrix} f \cdot r_1 / \delta_u \\ f \cdot r_2 / \delta_u \\ f \cdot r_3 / \delta_u \\ f \cdot t_1 / \delta_u \end{bmatrix} \quad (\text{A-1})$$

$$(1-k \cdot r^2) \cdot j \cdot [x, y, z, 1] \cdot \begin{bmatrix} r_7 \\ r_8 \\ r_9 \\ t_3 \end{bmatrix} = [x, y, z, 1] \cdot \begin{bmatrix} f \cdot r_4 / \delta_v \\ f \cdot r_5 / \delta_v \\ f \cdot r_6 / \delta_v \\ f \cdot t_2 / \delta_v \end{bmatrix} \quad (\text{A-2})$$

From Eq. A-1, we have

$$[x, y, z, 1] \cdot \begin{bmatrix} f \cdot r_1 / \delta_u \\ f \cdot r_2 / \delta_u \\ f \cdot r_3 / \delta_u \\ f \cdot t_1 / \delta_u \end{bmatrix} + [-ix, -iy, -iz, -i] \cdot \begin{bmatrix} r_7 \\ r_8 \\ r_9 \\ t_3 \end{bmatrix} + k \cdot [r^2 ix, r^2 iy, r^2 iz, r^2 i] \cdot \begin{bmatrix} r_7 \\ r_8 \\ r_9 \\ t_3 \end{bmatrix} = 0 \quad (\text{A-3})$$

From Eq. A-2, we have

$$[x, y, z, 1] \cdot \begin{bmatrix} f \cdot r_4 / \delta_v \\ f \cdot r_5 / \delta_v \\ f \cdot r_6 / \delta_v \\ f \cdot t_2 / \delta_v \end{bmatrix} + [-xj, -yj, -zj, -j] \cdot \begin{bmatrix} r_7 \\ r_8 \\ r_9 \\ t_3 \end{bmatrix} + k \cdot [jxr^2, jyr^2, jzr^2, jr^2] \cdot \begin{bmatrix} r_7 \\ r_8 \\ r_9 \\ t_3 \end{bmatrix} = 0 \quad (\text{A-4})$$

We define $[P_1]$, $[P_2]$ and $[P_3]$ as following:

$$[P_1] = \begin{bmatrix} f \cdot r_1 / \delta_u \\ f \cdot r_2 / \delta_u \\ f \cdot r_3 / \delta_u \\ f \cdot t_1 / \delta_u \end{bmatrix}, \quad [P_2] = \begin{bmatrix} f \cdot r_4 / \delta_v \\ f \cdot r_5 / \delta_v \\ f \cdot r_6 / \delta_v \\ f \cdot t_2 / \delta_v \end{bmatrix}, \quad [P_3] = \begin{bmatrix} r_7 \\ r_8 \\ r_9 \\ t_3 \end{bmatrix}$$

If we apply all 2D-3D pairs and combine Eq. A-3 and Eq. A-4 together, we then have:

$$\begin{bmatrix} \cdot & \cdot \\ \cdot & \cdot \\ x_n & y_n & z_n & 1 & 0 & 0 & 0 & 0 \\ 0 & 0 & 0 & 0 & x_n & y_n & z_n & 1 \\ \cdot & \cdot \\ \cdot & \cdot \end{bmatrix} \cdot \begin{bmatrix} [P_1] \\ [P_2] \end{bmatrix} + \begin{bmatrix} \cdot & \cdot & \cdot & \cdot \\ \cdot & \cdot & \cdot & \cdot \end{bmatrix} \cdot [P_3] \quad (A-5)$$

$$+ k \cdot \begin{bmatrix} \cdot & \cdot & \cdot & \cdot \\ ix_n r^2 & iy_n r^2 & iz_n r^2 & ir^2 \\ jx_n r^2 & jy_n r^2 & jz_n r^2 & jr^2 \\ \cdot & \cdot & \cdot & \cdot \\ \cdot & \cdot & \cdot & \cdot \end{bmatrix} \cdot [P_3] = \begin{bmatrix} \cdot \\ \cdot \\ 0 \\ \cdot \\ 0 \\ \cdot \\ \cdot \end{bmatrix}$$

Here, $n = 1, 2, 3, \dots, N$. N is the total number of 2D-3D pairs used in the calibration. For convenience, Eq. A-5 can also be written in the following matrix form:

$$[A] \cdot \begin{bmatrix} [P_1] \\ [P_2] \end{bmatrix} + [B] \cdot [P_3] + k \cdot [C] \cdot [P_3] = [0] \quad (A-6)$$

If we define $[p]$ and $[q]$ as following:

$$[p] = \begin{bmatrix} [P_1] \\ [P_2] \end{bmatrix} \cdot \frac{1}{t_3} \quad \text{and} \quad [q] = [P_3] \cdot \frac{1}{t_3}$$

Eq. A-6 will have the following format:

$$[A] \cdot [p] + [B] \cdot [q] + k \cdot [C] \cdot [q] = [0] \quad (\text{A-7})$$

APPENDIX B

INPUT FILE OF ABAQUS FOR IDEALIZED CONDITIONS

```
*HEADING
PRESSURIZING OF A FLAT POLYMER PLATE (CAX8H)
*NODE
1,0.,0.,0.
41,0.03175,0.0,0.0
101,0.0,0.000785,0.0
141,0.03175,.000785,0.0
201,0.0,.00157,0.0
241,.03175,0.00157,0.0
*NGEN
1,41,1
101,141,2
201,241,1
*NSET,NSET=CENTER
1,101,201
*ELEMENT,TYPE=CAX8H,ELSET=ONE
1,1,3,203,201,2,103,202,101
*ELGEN,ELSET=ALL
1,20,2,1
*BOUNDARY
41,1,2
141,2
241,1,2
1,1
101,1
201,1
*ELSET,ELSET=ONE
1
*SOLID SECTION,MATERIAL=A1,ELSET=ALL
*MATERIAL,NAME=A1
*HYPERELASTIC,N=1
.4E+6,.008E+6
*RESTART,WRITE,FREQUENCY=2
*STEP,NLGEOM,INC=36, UNSYMM=YES
*STATIC,RIKS
```

.001,1.0,.000001,0.1,1.0,1,1,10000.
*DLOAD
ALL,P1,3.0E+5
*MONITOR,NODE=201,DOF=2
*EL PRINT,FREQUENCY=50,ELSET=ALL
COORD , E
DG
LOADS
S,MISES
ENER
*EL PRINT,FREQUENCY=1,ELSET=ONE,SUMMARY=NO
COORD , E
DG
LOADS
S,MISES
ENER
*NODE FILE,NSET=CENTER
U ,RF
*EL FILE,FREQUENCY=2,ELSET=ONE
COORD , E
DG
LOADS
S
*NODE PRINT,FREQUENCY=1,NSET=CENTER
U,RF
*END STEP

APPENDIX C

INPUT FILE OF ABAQUS FOR GENERAL CONDITIONS

```
*HEADING
PRESSURIZING OF A POLYMER SHEET WITH TEMPERATURE
GRADIENCE (CAX8H)
*NODE
1,0.,0.,0.
41,0.03175,0.0,0.0
101,0.0,0.000785,0.0
141,0.03175,.000785,0.0
201,0.0,.00157,0.0
241,.03175,0.00157,0.0
*NGEN
1,41,1
101,141,2
*NGEN,NSET=UPPER
201,241,1
*NSET,NSET=CENTER
1,101,201
*NSET,NSET=N1
1,101,201
*NSET,NSET=N2
2,202
*NSET,NSET=N3
3,103,203
*NSET,NSET=N4
4,204
*NSET,NSET=N5
5,105,205
*NSET,NSET=N6
6,206
*NSET,NSET=N7
7,107,207
*NSET,NSET=N8
8,208
*NSET,NSET=N9
9,109,209
*NSET,NSET=N10
10,210
*NSET,NSET=N11
11,111,211
*NSET,NSET=N12
```

12,212
*NSET,NSET=N13
13,113,213
*NSET,NSET=N14
14,214
*NSET,NSET=N15
15,115,215
*NSET,NSET=N16
16,216
*NSET,NSET=N17
17,117,217
*NSET,NSET=N18
18,218
*NSET,NSET=N19
19,119,219
*NSET,NSET=N20
20,220
*NSET,NSET=N21
21,121,221
*NSET,NSET=N22
22,222
*NSET,NSET=N23
23,123,223
*NSET,NSET=N24
24,224
*NSET,NSET=N25
25,125,225
*NSET,NSET=N26
26,226
*NSET,NSET=N27
27,127,227
*NSET,NSET=N28
28,228
*NSET,NSET=N29
29,129,229
*NSET,NSET=N30
30,230
*NSET,NSET=N31
31,131,231
*NSET,NSET=N32
32,232
*NSET,NSET=N33
33,133,233
*NSET,NSET=N34
34,234
*NSET,NSET=N35

35,135,235
 *NSET,NSET=N36
 36,236
 *NSET,NSET=N37
 37,137,237
 *NSET,NSET=N38
 38,238
 *NSET,NSET=N39
 39,139,239
 *NSET,NSET=N40
 40,240
 *NSET,NSET=N41
 41,141,241
 *ELEMENT,TYPE=CAX8H,ELSET=ONE
 1,1,3,203,201,2,103,202,101
 *ELGEN,ELSET=ALL
 1,20,2,1
 *BOUNDARY
 41,1,2
 141,2
 241,1,2
 1,1
 101,1
 201,1
 *ELSET,ELSET=ONE
 1
 *SOLID SECTION,MATERIAL=A1,ELSET=ALL
 *MATERIAL,NAME=A1
 *HYPERELASTIC,N=1
 30E+6,0.2E+6,.0,110.0
 3.4E+6,0.1E+6,.0,139.0
 0.65E+6,0.08E+6,.0,141.0
 .49E+6,0.08E+6,.0,142.0
 0.4E+6,0.004E+6,.0,143.0
 .16E+6,.002E+6,.0,149.0
 *RESTART,WRITE,FREQUENCY=2
 *STEP,NLGEOM,INC=36, UNSYMM=YES
 *STATIC,RIKS
 .01,1.0,.0001,.05,1.0,1,1,10000.
 *DLOAD
 ALL,P1,6.E+4
 *INITIAL CONDITIONS,TYPE=STRESS
 ALL,0.06E+6,0.,0.06E+6
 *INITIAL CONDITIONS,TYPE=TEMPERATURE
 N1,149.0
 N2,148.9

N3,148.9
N4,148.9
N5,148.9
N6,148.9
N7,148.9
N8,148.9
N9,148.9
N10,148.9
N11,148.9
N12,148.9
N13,148.8
N14,148.7
N15,148.7
N16,148.6
N17,148.5
N18,148.4
N19,148.3
N20,148.2
N21,148.1
N22,147.8
N23,147.5
N24,147.3
N25,147.2
N26,147.1
N27,146.5
N28,146.0
N29,145.5
N30,144.5
N31,143.2
N32,142.1
N33,140.5
N34,139.2
N35,137.4
N36,135.2
N37,131.9
N38,129.0
N39,124.0
N40,115.7
N41,110.0
*MONITOR,NODE=201,DOF=2
*EL PRINT,FREQUENCY=25,ELSET=ALL
COORD , E
DG
LOADS
S,MISES
ENER

*EL PRINT,FREQUENCY=1,ELSET=ONE,SUMMARY=NO
COORD , E
DG
LOADS
S,MISES
ENER
*NODE FILE,NSET=CENTER
U ,RF
*EL FILE,FREQUENCY=2,ELSET=ONE
COORD , E
DG
LOADS
S
*NODE PRINT,NSET=CENTER
U
*NODE PRINT,FREQUENCY=1,NSET=UPPER
COORD
*END STEP

REFERENCES

- Andresen, K., Kamp, B., and Ritter, R. (1992), "Three-dimensional surface deformation measurement by a grating method applied to crack tips", *Optical Engineering*, 31(7), pp1499-1504.
- Bone, D. J. (1991), "Fourier fringe analysis: the two-dimensional phase unwrapping problem", *Applied Optics*, 30(25), pp3627-3632.
- Brigham, E. O. (1974), *The Fast Fourier Transform*, Prentice-Hall Publishing.
- Bruning, J. H., Herriott, D. R., Gallagher, J. E., Rosenfeld, D. P., White, A. D., and Brangaccio, D. J. (1974), "Digital wavefront measuring interferometer for optical surfaces and lenses", *Applied Optics*, 13, pp2693-2703.
- Bruynooghe, M. (1996), "Fast algorithms for automatic Moiré fringe analysis: application to non-contact measurement for quality control of industrial components", *Proceedings of SPIE*, v.2786, pp54-67.
- Chai, H. (1982), *The growth of impact damage in compressive loaded laminates* (Ph.D. Thesis, California Institute of Technology).
- Christensen, J. K., Rasmussen, H. K., and Kjaer, E. M. (1999), "Characterization of polymers by bubble inflation", *Proceedings of ANTEC'99*, pp1906-1909.
- Creath, K. (1992), "Error sources in phase-measuring interferometry", *Proceedings of SPIE*, v.1720, pp428-435.
- Crisfield, M. A. (1981), "A fast incremental/iteration solution procedure that handles 'snap-through'", *Computers and Structures*, v.13, pp55-62.
- Dawson-Howe K. M. and Vernon D. (1994), "Simple pinhole camera calibration", *Intl. J. of Imaging Systems and Technology*, 5(1-6), pp1-6.
- Derdouri, A., Connolly, R., and Khayat, R. (1998), "Material constants identification for thermoforming simulation", *ANTEC'98*, 672-675.
- Faig, W. (1975), "Calibration of close-range photogrammetric systems: mathematical formulation", *Photogrammetric Eng. & Remote Sensing*, 41, pp1479-1486.

- Fang, J. (1991), "Optical modulation and digital demodulation of an in-plane Moiré carrier", *Optics & Laser Technology*, 23(6), pp349-352.
- Fujimoto, K. *et al.*, (1992), "Slit laser scanning Moire method and a simple method for distinguishing between depression and elevation", *Advanced Robotics*, 6(2), pp141-163.
- Gierloff, J. J. (1987), "Phase unwrapping by regions", *Proceedings of SPIE*, v.818, pp2-9.
- Goldstein, R. M., Zebker, H. A., and Werner, C. L. (1988), "Satellite radar interferometry two-dimensional phase unwrapping", *Radio Science*, 23(4), pp713-720.
- Gonzalez, R. C. and Woods, R. E. (1993), *Digital image processing*, Addison-Wesley Publishing.
- Gonzalez-Velasco, E. A. (1995), *Fourier Analysis and Boundary Value Problems*, Academic Press.
- Halioua, M., and Liu, H.-C. (1986), "Optical sensing techniques for 3D machine vision", *Proceedings of SPIE*, Vol. 665, pp150-161.
- Halioua, M., and Liu, H.-C. (1989), "Optical three-dimensional sensing by phase measuring profilometry", *Optics & Lasers in Engineering*, 11(3), pp185-215.
- Han, B., Ifju, P., and Post, D. (1993), "Geometric Moiré methods with enhanced sensitivity by optical/digital fringe multiplication", *Exp. Mech.*, 33(3), pp195-200.
- He, Y. M., Tay, C. J., and Shang, H. M. (1998), "Deformation and profile measurement using the digital projection grating method", *Optics & Lasers in Engineering*, 30, pp367-377.
- Hibbitt, Karlsson & Sorensen, INC. (1998), *User's Manual on ABAQUS/STANDARD Version 5.8*.
- Hibbitt, Karlsson & Sorensen, INC. (1998), *Theory Manual on ABAQUS/STANDARD Version 5.8*.
- Hobson, C. A., Atkinson, J. T., and Lilley F. (1997), "The application of digital filtering to phase recovery when surface contouring using fringe projection techniques", *Optics & Lasers in Engineering*, 27, pp355-368.
- Hung, Y. Y., Liang, C. Y., Hovanesian, J. D., and Durelli, A. J. (1977), "Time-averaged shadow Moiré method for studying vibrations", *Applied Optics*, 16(6), pp1717-1719.
- Huntley, J. M. (1989), "Noise-immune phase unwrapping algorithm", *Applied Optics*, 28(15), pp3268-3270.

Imageware, SDRC (1999), *User's Manual on SURFACER version 9.0*.

Joenathan, C. (1994), "Phase-measuring interferometry: new methods and error analysis", *Applied Optics*, 33(19), pp4147-4155.

Joye, D. D., Poehlein, G. W., and Denson, C. D. (1972), "A bubble inflation technique for the measurement of viscoelastic properties in equal biaxial extensional flow", *Trans. Of the Soc. Of Rheology*, 16(3), pp421-445.

Judge, T. R. and Bryanston-Cross, P. J. (1994), "A review of phase unwrapping techniques in fringe analysis", *Optics & Lasers in Engineering*, 21, pp199-239.

Kobayashi, A. S. (1993), *Handbook on Experimental Mechanics* (2nd Edition), Society of Experimental Mechanics.

Kokidko, D., Gee, L., Chou S. C., and Chiang, F. P. (1997), "Method for measuring transient out-of-plane deformation during impact", *Int. J. Impact Engineering*, 19(2), pp127-133.

Lambros, J., and Rosakis, A. J. (1997), "An experimental study of dynamic delamination of thick fiber reinforced polymeric matrix composites", *Exp. Mech.*, 37(3), pp360-366.

Lenz, R. K. and Tsai, R. Y. (1988), "Techniques for calibration of the scale factor and image center for high accuracy 3-D machine vision metrology", *IEEE Transaction on Pattern Analysis and Machine Intelligence*, 10(5), pp713-720.

Li, Y. and Nemes, J. A. (1999), "High speed 3D measurement system for dynamic deformation measurement", *Proceedings of SEM'99 Spring Conference*, pp158-160.

Li, Y. and Nemes, J. A. (1998), "Whole-field displacement measurement of laminated composite plates", *Proceedings of SEM'98 Spring Conference*, pp22-25.

Li, Y. and Nemes, J. A. (1997), "Development of an optical measurement technique for dynamic surface three dimensional measurement", *Proceedings of SEM'97 Spring Conference (Student Paper)*, pp11-12.

Liao, J. E. A., and Voloshin, A. S. (1993), "Enhancement of the shadow-Moiré method through digital image processing", *Exp. Mech.*, 33(1), pp59-63.

Lin, P. P., Chawla, M. D., and Wagner, P. M. (1997), "Three-dimensional deformation comparison between F-16 bias and radial aircraft tires", *Tire Science & Technology*, 25(1), pp63-75.

Macy, W. (1983), "Two-dimensional fringe pattern analysis", *Applied Optics*, 22(23), pp3898-3901.

Marshall, S. J. *et al.* (1993), "Development of a 3D clinical facial imager", Proceedings of SPIE, vol.1889, pp255-262.

Martins, H. A., Birk, J. R., and Kelley, R. B. (1981), "Camera models based on data from two calibration planes", Computer Graphics & Image Processing, 17, pp173-180.

Meadows, D. M., Johnson, W. O., and Allen, T. B. (1970), "Generation of surface contours by Moiré patterns", Applied Optics, 9(4), pp942-947.

Mertz, L. (1983), "Real-time fringe pattern analysis", Applied Optics, 22, pp1535-1539.

Mckelvie, J. (1986), "On the limits to the information obtainable from a Moiré fringe pattern", Proceedings of the 1986 SEM Spring Conference, pp971-980.

Moran, A. J., and Lipczynski, R. T. (1994), "Automatic digitization and analysis of Moiré topograms on a personal computer for clinical use", Medical Engineering and Physics, 16(3), pp259-264.

Motion Analysis Systems Division, EASTMAN KODAK COMPANY (1998), *User's Manual on Kodak Motion Corder Analyzer SR-Series*.

Motion Analysis Systems Division, EASTMAN KODAK COMPANY (1998), *User's Manual on Kodak Multi-Channel Data Link*.

Murakami, K. and Murakami, Y. (1978), "A study of Moiré topography: a method for discriminating between the concave and convex regions of an object", Bulletin Of the JSME, 21(155), pp788-792.

Myler, H. R. and Weeks, A. R. (1993), *The Pocket Handbook of Image Processing Algorithms in C*, Prentice-Hall Publishing.

Nadeborn, W., Andra, P., Juptner, W., and Osten, W. (1993), "Evaluation of optical shape measurement methods with respect to accuracy of data", Proceedings of SPIE, v.1983, pp928-930.

Nakadate, S., and Saito, H. (1985), "Fringe scanning speckle-pattern interferometry", Applied Optics., 24(14), pp2172-2180.

Ning, P. T., and Peng, W. L. (1988), "Automatic analysis of Moiré fringe patterns by using an image-processing system", Exp. Mech., 28(4), pp350-354.

Pan, R., and Watt, D. F. (1996), "Biaxial tension deformation behavior of sparsely reinforced flexible elastomer sheet", Plastics, Rubber and Composites Processing and Applications, 25(1), pp29-36.

Pirodda, L. (1982), "Shadow and projection Moiré techniques for absolute or relative mapping of surface shapes", *Optical Engineering*, 21(4), pp640-649.

Rhi-Sausi, J., and Dealy, J. M. (1981), "A biaxial extensometer for molten plastics", *Polymer Eng. and Sci.*, 21(4), pp227-232.

Rivlin, R. S. and Saunders, D. W. (1951), "Large elastic deformations of isotropic materials VII. experiments on the deformation of rubber", *Phil. Trans. Roy. Soc.*, Vol.243A, pp251-288.

Schmidt, L. R. and Carley, J. F. (1975), "Biaxial stretching of heat-softened plastic sheets: experiments and results", *Polymer Eng. and Sci.*, 15(1), pp51-62.

Schreiber, W., Kirschner, V., Kowarschik, R., and Notni G. (1997), "Managing some calibration problems in fringe projection shape measurement systems", *Fringe'97*, 443-450.

Sciammarella, C.A. (1982), "The Moiré Method—A Review", *Experimental Mechanics*, 22(11), pp418-433.

Senf, H., Strassburger, E., and Rothenhausler, H. (1997), "Investigation of bulging during impact in composite armour", *Journal de Physique IV*, 7(3), pp301-306.

Takasaki, H. (1970), "Moiré Topography", *Applied Optics*, 9(6), pp1467-1472.

Takeda, M., Ina, H., and Kobayashi, S. (1982), "Fourier-transform method of fringe-pattern analysis for computer-based topography and interferometry", *J. Opt. Soc. Amer.*, 72(1), pp156-160.

Takeda, M., and Mutoh, K. (1983), "Fourier transform profilometry for the automatic measurement of 3-D object shapes", *Applied Optics*, 22(24), pp3977-3982.

Toyooka, S., and Iwaasa, Y. (1986), "Automatic profilometry of 3-D diffuse objects by spatial phase detection", *Applied Optics*, 25(10), pp1630-1633.

Treloar, L. R. G. (1944), *Trans. Inst. Rubber Ind.*, Vol.19, pp201.

Tsai, R. Y. (1986), "An efficient and accurate camera calibration technique for 3-D machine vision", *Proceedings of IEEE Conference on Computer Vision and Pattern Recognition*, pp364-374.

Tsai, R. Y. (1987), "A versatile camera calibration technique for high-accuracy 3D machine vision metrology using off-the-shelf TV cameras and lenses", *IEEE Journal of Robotics and Automation*, RA-3(4), pp323-344.

Wykes, C., Morshedizadeh, R., and Ordish, S. (1994), "Calibration of projected fringe surface topography measurement", Proceedings of SPIE, v.2248, pp74-84.

Yamamoto, M., Tonooka, M., Otani, Y., and Yoshizawa, T. (1998), "Surface profile measurement of specular objects by grating projection method", J. of the Japan Society of Precision Engineering, 64(8), pp1171-1175.

Yang, W. H. and Feng, W. W. (1970), "On axisymmetrical deformations of nonlinear membranes", J. of Applied Mechanics, 37, pp1002.

Yogo, T., Hayashi, Y., and Chou, S. (1993), "The function and usage of the Moiré Master—new Moiré 3D measurement machines", Kikai To Kogu, 37(10), pp48-54.

Wu, R. L. (1985), *Finite element and experimental analyses of the inflation of membranes in relation to thermoforming* (Master Thesis, McGill University).

Zhu, G. Q., Goldsmith W., and Dharan C. K. H. (1992), "Penetration of laminated kevlar by projectiles—I. Experimental investigation", Int. J. Solids Structures, 29(4), pp399-420.